



BUDAPEST UNIVERSITY OF TECHNOLOGY AND ECONOMICS
FACULTY OF NATURAL SCIENCES

Characterization of conductance fluctuations in atomic and molecular junctions

PhD Dissertation

Gréta Mezei

Supervisor: Zoltán Balogh

Institute of Physics,

Department of Physics

Budapest

2025

Contents

1	Introduction	1
2	Literature Review	3
2.1	Emerging applications of molecular electronics: from single-molecular switches to molecular memristors	3
2.1.1	Single molecule switches	3
2.1.2	Molecular memristors	4
2.2	Creation of atomic size contacts and contacting molecules	5
2.2.1	Scanning Tunneling Microscope-based Break Junction (STM-BJ)	5
2.2.2	Atomic Force Microscope-based Break Junction (AFM-BJ)	7
2.2.3	Mechanically Controllable Break Junction (MCBJ)	8
2.2.4	Adding molecules	9
2.2.5	Comparison	11
2.3	Conduction of nanowires	11
2.4	Statistical analysis of the conductance of a nanojunction	14
2.4.1	Conductance measurements	14
2.4.2	Conductance histograms	15
2.4.3	Conductance–displacement histograms	16
2.4.4	Correlation of conductance traces	18
2.4.5	Trace selection techniques	19
2.5	$I(V)$ characteristics measurements	20
2.6	Noise spectroscopy of molecular junctions	21
2.6.1	Basics of noise measurements	21
2.6.2	Description of noise	22
2.6.3	Relevant noise mechanisms in single-molecule systems	23
2.6.4	Exploring flicker noise in single-molecule junctions	25
3	Measurement Technique and Analysis Software Development	33
3.1	Measurement control and measurement technological considerations	33
3.2	Mechanically controllable break junction setups	36
3.2.1	Sample preparation	36

Contents

3.2.2	Low-temperature and room-temperature MCBJ setups	38
3.2.3	Molecule dosage techniques	39
3.3	Room-temperature scanning tunneling microscope-based break junction setup	41
3.4	FPGA-based measurement control	42
3.5	Data analysis software developments	44
3.5.1	Optimized data architecture for high-performance evaluation	45
3.5.2	Data analysis developments for hold measurements	46
4	Binary Conductance Switching in Au–BPY–Au Single-molecule Nano-wires	49
4.1	Conductance of Au–BPY–Au molecular junctions in low-temperature measurements	50
4.2	Analysis of mechanical switching of Au–BPY–Au molecular junctions . . .	52
4.3	Current–voltage characteristics of Au–BPY–Au single molecular junctions .	54
4.4	Switching dynamics as a function of electrode separation	55
4.5	Voltage dependence of the switching dynamics	60
4.6	Comparing the experimental results with possible theoretical models	63
4.6.1	Simple two-level system (TLS) models	64
4.6.2	Temperature activated switching model	65
4.6.3	Vibrational pumping model	66
4.6.4	Double-well potential inversion model	67
4.6.5	Heuristic model relying on the molecule’s energy dependent transition probability	67
4.7	Conclusion	68
5	Temporal Noise Measurements on Au–BPY–Au Single-molecule Nano-wires	71
5.1	Basics of temporal noise measurement technique	72
5.2	Noise characteristics of Au-BPY-Au single-molecule junctions	74
5.3	EPCP-based trace selection technique	77
5.4	EPCP-aided interpretation of single-molecule flicker noise measurements .	79
5.5	Conclusions	84
6	Correlating Noise and Nonlinear Conductance Data in Real-time Controlled Break Junction Measurements	87
6.1	Real-time controlled break junction measurements	88
6.2	Stability analysis of hold measurements	89
6.3	Relaxation phenomena in gold tunnel junctions	93
6.4	Investigation of noise phenomena in gold tunnel junctions using combined $I(V)$ characteristics and noise measurements	95
6.4.1	The scheme of combined $I(V)$ characteristics and noise measurements	96

6.4.2	Conductance dependence of relative fluctuation	97
6.4.3	Fitting of measured $I(V)$ curves and calculation of simulated noise using numerically evaluated Simmons model	100
6.5	Comparison of measured and simulated noise characteristics	104
6.6	Conclusions	106
7	Thesis Statements	109
7.1	Binary conductance switching in gold–4,4′-bipyridine–gold single-molecule nanowires	109
7.2	Investigation of configuration-specific noise characteristics of gold–4,4′-bi- pyridine–gold molecular contacts	109
7.3	Investigation of stability and noise phenomena of gold nanogaps using an FPGA-based real-time measurement control system	110
8	Acknowledgements	113
	List of Publications	115
	Other Publications	117
	Bibliography	119

Contents

List of Figures

2.1	Depiction of the two binding geometries of BPY between two gold electrodes.	4
2.2	Schematics of STM–BJ measurements.	7
2.3	Schematics of AFM–BJ measurements	8
2.4	Schematics of MCBJ measurement	10
2.5	Example methods for in situ molecule dosing techniques	11
2.6	Schematics of transport regimes	12
2.7	Parabolic energy dispersion relations	13
2.8	Conductance measurement flow chart	15
2.9	Creation of 1D conductance histograms.	16
2.10	Creation of 2D conductance–displacement histograms.	17
2.11	Statistical analysis and configurations of Au–2,7-diaminofluorene–Au molecular junctions	19
2.12	Origin of the $1/f$ -type noise	24
2.13	Flicker noise as a probe of electronic interaction at metal–single-molecule interfaces	27
2.14	Characteristics of stacked dimer molecular junctions.	29
2.15	Scaling exponent curves as a function of displacement	30
3.1	Components of the measurement control system	34
3.2	Simplified circuit diagram of the current to voltage converters used in our measurements	35
3.3	Photos of samples with different fastening mechanisms	37
3.4	Black and white photo and cutaway diagram of the sample chamber of the low-temperature MCBJ sample holder	39
3.5	Sample holders during measurements	40
3.6	Photomontage of the measurement setup illustrating molecule dosage techniques	41
3.7	Room temperature STM-BJ setup	42
3.8	Measurement control setup	43
3.9	Measurement flow diagram.	44
3.10	File structure	46

List of Figures

3.11	Demonstration of power spectral density calculation for a hold trace with a complex bias signal	48
4.1	Periodic switching between the two stable configurations of Au-BPY-Au junctions	50
4.2	Molecular traces and histograms.	51
4.3	Mechanical switching demonstration.	53
4.4	Current-voltage characteristics measurements at low temperature.	55
4.5	Comparison of conductances measured in the I(V) characteristics cycles with 1D closing break junction histogram.	56
4.6	Demonstration of the switching mechanism.	56
4.7	Location of switching events.	58
4.8	Switching times distribution	59
4.9	Bias dependent switching times.	61
4.10	Statistical analysis of the switching times.	62
4.11	Illustration of the model considerations	64
4.12	Vibrational pumping model	67
4.13	Double-well potential inversion model	68
5.1	Example slow MCBJ trace for temporal noise analysis	73
5.2	Analysis of the conductance dependence of relative conductance noise . . .	75
5.3	Distribution of γ exponent.	77
5.4	Statistical analysis of Au-BPY-Au dataset.	78
5.5	Histograms of trace groups selected via the EPCP method using $(P^{(4)})$. . .	80
5.6	Relative noise analysis for HighG and LowG class separately	81
5.7	Configuration-specific $1/f$ -type noise analysis of Au-BPY-Au junctions. . .	82
6.1	Analysis of tunnel hold measurement stability.	89
6.2	Comparison of the 1D histograms	90
6.3	Comparison of the conductances before and after the hold portion	92
6.4	Stability of tunnel junction.	94
6.5	Hold measurement with current-voltage characteristics.	97
6.6	Relative noise distributions for the second plateau of opening and closing traces	99
6.7	Example $I(V)$ curves	101
6.8	Distribution of gap size and barrier height in tunnel contacts acquired from simulation	103
6.9	Relative noise distributions from simulation	104
6.10	Heatmaps of the squared difference matrices of the simulated and measured mean relative noise ($sd_{j,k}$)	105

List of Abbreviations

G_0	conductance quantum ($G_0 = 2e^2/h$)
BJ	Break Junction
BPY	4,4'-bipyridine
DAF	2,7-diaminofluorene
DAQ	Data AcQuisition
DAT	4,4''-diamino-p-terphenyl
EPCP	Extremal Principal Component Projection
FPGA	Field-Programmable Gate Array
MCBJ	Mechanically Controllable Break Junction
PCA	Principal Component Analysis
PCP	Principal Component Projection
PSD	Power Spectral Density
SME	Single Molecule Electronics
STM-BJ	Scanning Tunneling Microscopy based Break Junction
TLS	Two-Level System
TMBDA	2,3,5,6-tetramethyl-1,4-benzenediamine

List of Abbreviations

Chapter 1

Introduction

In his 1960 talk, Richard P. Feynman envisioned a new field that would manipulate matter on the atomic/molecular scale and design functional devices consisting only of a few atoms/molecules [1]. In the past decades, electronic devices have gone through remarkable development and miniaturization and continue to be developed at a rapid rate. The progress was empirically described by Moore's law, which predicted that the number of transistors in an integrated circuit doubles about every two years [2]. The latest transistors have an active region of a few ten nanometers, approaching the molecular scale. The dream of expanding Moore's law to the molecular level inspired the growth of the molecular electronics field. By integrating single or grouped molecules into electronic circuits, the size of electronic devices would further shrink [3, 4]. The integration of molecules has the added advantage that they can be tailored to a specific task through chemical synthesis and by adding functional groups, which also means that they are ideal candidates in sensing applications [5].

Before we can utilize single molecules in functional devices, we must understand their transport properties and behavior. However, this also imposes several difficulties, such as creating an opening that is small enough to fit a single molecule and measuring the current through this molecular junction [6, 7]. The development of several methods for the creation of small metallic openings, such as break junction methods [8–15], chemical etching [16, 17], electromigration [18–21], and various molecule-dosing systems have enabled the construction and study of numerous single-molecule junctions to characterize their novel properties [22]. Molecular electronics is a multidisciplinary field that combines the efforts of chemists, physicists, biologists, material scientists, electronic engineers, and data scientists in using an individual or a small set of molecules as the active region of electronic devices.

The goal of this research field is not only to explore fundamental questions, such as whether a given molecule can bridge the electrodes, what molecular configurations may form, and what transport mechanisms characterize them but also to investigate how these configurations can be controlled and what kind of noise characteristics they exhibit [23]. Noise is often considered a disturbing factor [24]; however, it is also a great source of

Chapter 1. Introduction

information about the transport mechanism in the break junction. Noise spectroscopy is a well-established characterization technique for investigating the properties of various systems and devices, such as nanowires, memristors, transistors, etc. [25–28]. The study of electronic noise expanded to the field of molecular electronics as well [29–31].

The Neuromorphic Electronics Group¹ at the Budapest University of Technology and Economics has been studying the charge transport mechanism of atomic and single-molecule junctions for years [32–37], developing several promising measurement setups for both low- and room-temperature measurements [38–41], contributed statistical methods to the characterization of molecular junctions [34, 36, 40–44], and utilized machine learning methods to sort measurements [44–46], as well as established $1/f$ -type noise spectroscopy measurement system [30] to characterize molecular junctions. I joined the group in 2017 and began focusing on molecular measurements, aiming to make meaningful contributions to the rapidly advancing area of molecular electronics research [P1–P4].

In this dissertation, I summarize my work in the study of molecular electronics and statistical analysis of molecular junctions. In the following, I present the synopsis of my dissertation. In chapter 2, I summarize the current state of molecular electronics, including well-established techniques (such as break junction methods for measurements) and the theory of state-of-the-art analysis techniques (such as correlation, principal component, and noise analysis). In chapter 3, I present the measurement setup and the measurement control program in detail, followed by a summary of the development of the file structure and the analysis software with a collection of complex statistical methods used to analyze the measurement results. Following these introductory chapters, I review the scientific results of my work, divided into 3 additional chapters, according to the observed mechanism and measurement method. In chapter 4, I show my observation of the bistable molecular switching of 4,4'-bipyridine at low temperature to mechanical and electrical stimuli. I present a complex statistical analysis of the voltage-dependent switching times. In chapter 5 I present the study of the temporal evolution of noise in slow break junction measurements performed on gold–4,4'-bipyridine–gold molecular junctions. First, I study the noise generally, then using principal component analysis, I separately analyze the two configurations of 4,4'-bipyridine. In chapter 6 I collect the test measurement conducted for the validation of hold measurements performed with the Field-Programmable-Gate-Array-based measurement control software developed by András Magyarkuti [41].

¹https://nanoelectronics.physics.bme.hu/neuromorphic_electronics

Chapter 2

Literature Review

This chapter presents a summary of commonly employed techniques for constructing atomic and molecular junctions, along with the fundamental theoretical frameworks used to describe these small systems. Subsequently, I discuss recent discoveries that are relevant to my findings.

2.1 Emerging applications of molecular electronics: from single-molecular switches to molecular memristors

In modern computing applications, particularly in neuromorphic and brain-inspired computing, the demand for energy-efficient, highly integrated, and functionally versatile devices is growing rapidly. By exploiting the intrinsic electronic, structural, and chemical tunability of individual molecules, molecular electronics is a promising alternative of conventional silicon-based technology. Recent results have demonstrated that molecules can serve not only as passive elements, but also as active circuit components such as switches, rectifiers, or memory elements [47–49].

2.1.1 Single molecule switches

Certain molecules have the ability to function as reversible conductance switches under external stimuli such as light, voltage, or mechanical force, making them ideal candidates for various electronic applications [49]. For example, azobenzene-based optically driven switches that exhibit reversible *trans-cis* photoisomerization or photochromic diarylethene derivatives that transition between *open-ring* and *closed-ring* configurations under ultraviolet and visible light [50, 51]. Besides light induced switching, other mechanisms are also possible including force-induced switches, such as mechanically induced *cis-trans* conformational changes in molecules like 1,4-diethynylbenzene [52], which show conductance hysteresis due to structural distortions under mechanical strain; and current-induced

Chapter 2. Literature Review

hydrogen tautomerization in phthalocyanine derivatives, where hydrogen repositioning within the molecule modulates conductance [53].

Of particular relevance to my work is the study by Quek et al., who reported mechanically controlled binary conductance switching in Au–4,4'-bipyridine–Au (BPY) molecular systems [54]. The 4,4'-bipyridine molecule exhibits two distinct binding geometries between the gold electrodes (see Figure 2.1), resulting in two different conductance values. At smaller electrode separations, the conductance is higher because the coupling between the aromatic ring and the gold electrode contributes to the overall conductance. As the electrode separation increases, the molecule shifts toward the apex, decoupling the aromatic ring so that only the nitrogen linker remains connected. This structural change leads to a decrease in the measured conductance. Quek et al. demonstrated that these two configurations could be switched by fine-tuning the electrode separation.

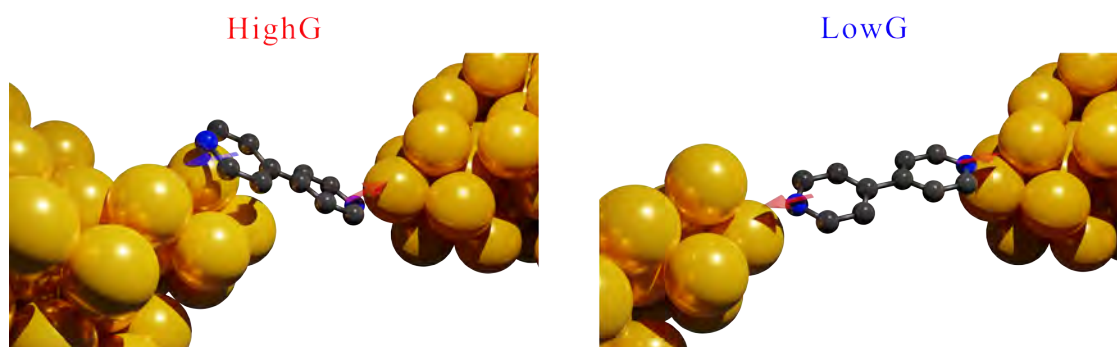


Figure 2.1: Depiction of the two binding geometries of BPY between two gold electrodes. At a smaller electrode distance, the nitrogen linkers and the aromatic rings are both coupled to the gold electrodes, resulting in a higher characteristic conductance value. When the electrodes are moved further away from each other, the aromatic ring decouples, and the conductance decreases. Figures created by Zoltán Balogh.

2.1.2 Molecular memristors

Memristors, i.e. circuit elements whose resistance can be modulated and retained based on their voltage history, have emerged as key building blocks of fully hardware-implemented neural networks due to their ability to mimic synaptic behavior. Memristors can be fabricated from various materials, such as metal oxides, other solid-state materials, magnetic or ferroelectric materials, and organic compounds. Recent works have extended the concept to the molecular scale [48, 55].

The development of molecular electronic devices, such as the above mentioned molecular memristors and switches, requires a detailed understanding of single-molecule behavior, including structural dynamics, charge transport properties, and interactions with the surrounding environment. The need to explore and characterize the electronic functionalities of individual molecules provided the primary motivation for my work.

2.2 Creation of atomic size contacts and contacting molecules

In this section, I give an introduction to the most common methods used to fabricate metallic atomic-size contacts. These methods can be used not only to study the physical properties of metallic atomic contacts but they also provide the basis to contact single molecules. The collection of these methods are the *break junction (BJ)* methods. The name refers to the primary working principle of breaking a metallic junction. In the simplest case, we start with a macroscopic metallic wire. Depending on the particular method, the wire is elongated, causing it to narrow gradually until it reaches a width of only a few atoms or even a single atom, eventually breaking to create a gap between the two newly formed electrodes. The resulting gap is then used to contact molecules. Some techniques use lithographic methods to fabricate a metallic bridge, so the starting wire is only a few nanometers wide. Like the larger wire, this bridge is also broken to create a gap to contact molecules.

Now that the metallic nanowire was formed, it is time to talk about the dosing of molecules. There are two ways to add molecules to the system: either prior to junction formation, so the molecule is present from the beginning; or following control measurements, one can add the molecule in-situ. The latter method makes it possible to check the cleanliness of the system during the control measurement to make sure that there is no contamination that could interfere with the molecule. During in-situ molecule dosage, the two electrodes are separated. Regardless of the dosage method, the target molecule attaches to the surface of either of the electrodes. Then, the electrodes are pushed into each other, and in the next gap formation, there is a chance that the molecule is going to bridge the gap, forming a molecular junction.

There are several methods used in the literature to form nanosized gaps for contacting and studying molecules; I want to focus on three of them: the scanning tunneling microscope-based break junction (STM-BJ), the atomic force microscope-based break junction (AFM-BJ), and the mechanically controllable break junction (MCBJ). In addition, I review some of the methods for dosing molecules corresponding to each measurement technique. In my measurements, I used the MCBJ method with in situ evaporation of the molecule, but some of the literature that I am going to mention uses STM-BJ, and the AFM can be useful tool to complement measurements, which is why I am going to briefly discuss these methods, too. The MCBJ measurement setup and molecule dosage technique I used will be discussed in detail in chapter 3.

2.2.1 Scanning Tunneling Microscope-based Break Junction (STM-BJ)

The operation of a scanning tunneling microscope (STM) involves the following: a highly sharpened gold tip, potentially terminating in a single atom, traverses above a conductive

Chapter 2. Literature Review

sample in a raster pattern. The tunnel current generated between the tip and the sample is monitored. As the tunnel current exponentially correlates with the distance between the tip and the sample, this metric can be used to accurately chart the topology of the sample. With a feedback loop regulating the tip's elevation to maintain a consistent current, the trajectory of the tip outlines the topology of the sample. Although this represents the primary application of the STM, it can also be employed in alternate techniques, such as conducting break junction experiments [56].

For break junction measurements, instead of hovering above the sample, the tip is indented in the surface. When the tip is pulled back, first, an atomic-size contact forms, and then further pulling the tip away from the surface, the contact created between the tip and the sample ruptures, forming a nanogap between the tip and the sample. If we measure the current during the rupturing process, we can study the conductance of few atom wide or atomic nanowires. If we add molecules to the system (for molecule dosing methods, see subsection 2.2.4), they can be built inside the nanogap formed after rupture, so we can study their conduction properties. The schematics of an STM–BJ measurement are shown in Figure 2.2(a), while in Figure 2.2(b) the schematics of junction evolution during the rupturing process with a simplified conductance as a function of the distance moved by the STM tip [57].

After the initial indentation, the tip will be covered by several atomic layers of metal from the substrate; therefore, after repeated indentations, new contacts may form consisting of the same metal for both electrodes. The formation and rupturing of a nanocontact can be repeated several thousand times, while we can measure the current through the wire and calculate the conductance of the junction at a given elongation [56, 58].

The main advantages of the *scanning tunneling microscope-based break junction (STM–BJ)* technique lie in its speed and versatility in its application (as we shall see later). An example of the versatility of the STM–BJ method is that the tip and sample can be composed of different materials. This capability allows for the creation of contacts between two distinct metals, known as *heterojunctions*. Another advantage is that the STM allows us to map the topography of the two electrodes before and after formation of the contact. However, the exact atomic configuration of the contact cannot be measured directly, because the tip is indented into the surface, and the atomic contact is usually formed while the tip is pulled away from the surface. An atomic contact can also be formed by approaching the surface with the tip: as the tip moves closer to the substrate, an exponential increase in the conductance is observed, which is followed by a step-like increase of the conductance indicating the formation of a chemical bond between the tip and the electrode. The contact formation procedure can be repeated several thousand times and with the additional freedom of moving the tip horizontally, one can measure at a chosen point on the surface, creating new contacts over and over. Another reason why the STM–BJ technique is widely used is the ease of molecule dosage (see later).

The advantages make the STM–BJ technique widely used, but there are some drawbacks to consider. External parameters like temperature or magnetic fields limit the stability, while the lifetime of the contacts is short because the STM is sensitive to vibra-

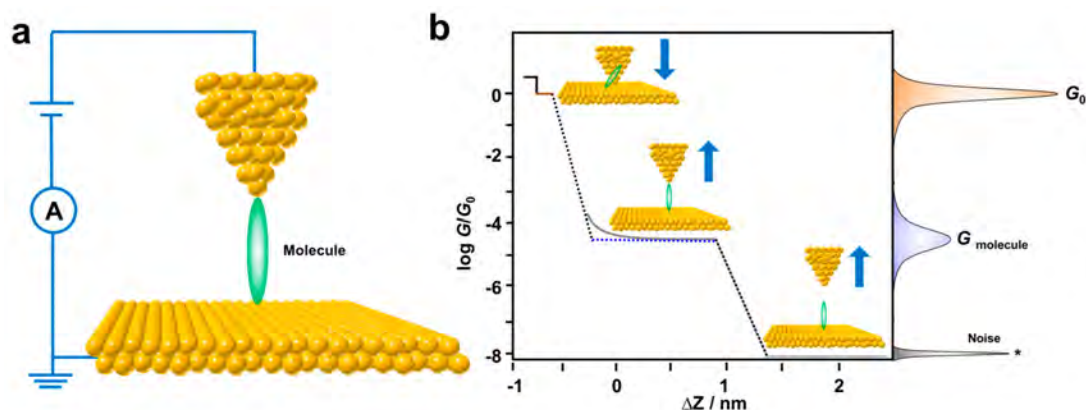


Figure 2.2: (a) Schematics of STM–BJ measurements. The molecule of interest bridges the gap between the STM tip and the gold plate. The current is recorded at a fixed bias, while moving the tip further away from (opening) or closer (closing) to the gold plate, changing the gap size. (b) Simplified conductance curve with the schematic junction evolution during STM–BJ measurement and the main features of the resulting conductance histograms. First, metallic contact is formed by pushing the gold tip into the gold surface. While moving the tip away from the gold plate, plateaus are visible at integer multiples of the conductance quantum (G_0), the last at $1 G_0$, corresponding to the quantum conductance of atomic metal contact. This is followed by the molecular plateau at a lower conductance value. And finally, the junction ruptures and the background noise is measured. The plateaus in the conductance–displacement curves result in peaks in the conductance histograms. Source: [57].

tions.

2.2.2 Atomic Force Microscope-based Break Junction (AFM–BJ)

The fundamental principle of *atomic force microscope* (AFM) involves a tip mounted on a flexible cantilever, which is moved in close proximity to a surface. The deflection of the cantilever is measured using a laser pointer and a position-sensitive detector. This setup enables the determination of the force exerted between the tip and the sample. The AFM is capable of functioning in multiple measurement modes, including the *contact* mode, where the fine tip is pressed into the surface, the *non-contact* mode, characterized by the tip hovering above the surface with deflection resulting from long-range forces such as van der Waals forces, and the *tapping* mode, in which the tip undergoes vibration while scanning the surface and the vibration frequency shift caused by the forces between the sample and the tip is measured. In contrast to STM, which relies on the tunnel current flowing from the sample to the tip, AFM exploits the distance-dependent force interaction between a fine tip and a surface, making it suitable for the study of insulating samples. However, if the sample is conductive and the AFM tip is covered with a conductive material, the local conduction properties can be measured in contact mode. Similarly to

STM–BJ, even the BJ method can be implemented using the contact mode of the AFM, and combining the conductance measurements with the force data, we can study the force required to form or break the contacts [59–61].

There are two methods to create atomic contacts using the *atomic force microscope based break junction (AFM–BJ)* technique, as illustrated in Figure 2.3. The conductive AFM–BJ depicted in Figure 2.3(a) uses a metal-covered AFM tip fixed on a conductive cantilever and the contact is formed by pushing the tip into the metallic surface. With this setup, the conductance and force between the tip and the sample are measured simultaneously, so we can study the force required to form or break the contacts. The AFM method can also be used in combination with an STM, as illustrated in Figure 2.3(b). The sample is fixed on a cantilever and the metallic contact is formed with the sharp metal tip of an STM setup that records the current flowing through the contact. Meanwhile, the deflection of the cantilever is recorded with a separate AFM, so again the conductance and force can be recorded simultaneously [56, 62].

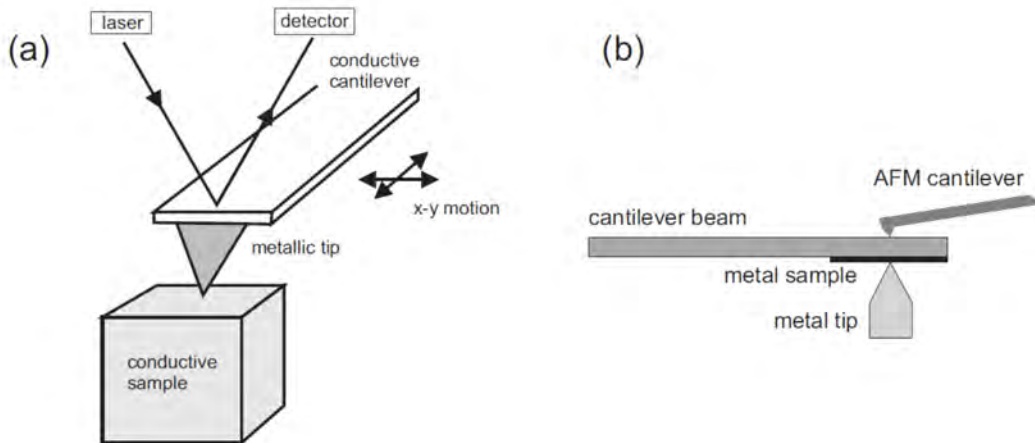


Figure 2.3: Schematics of AFM–BJ measurements (a) Conductive AFM–BJ. *The current and the force is measured simultaneously by the AFM. (b) Combined AFM and STM–BJ measurements.* *The contact is formed with the metal tip of the STM while the force is measured with the AFM. Source: [56].*

2.2.3 Mechanically Controllable Break Junction (MCBJ)

Although STM- and AFM-based break junction methods are widely employed and effective, they exhibit considerable sensitivity to mechanical instabilities. To mitigate these effects, the *mechanically controllable break junction (MCBJ)* technique can be used as an alternative approach. The atomic contact is formed using a metallic wire fixed to a flexible plate that is mounted in a three-point bending mechanism: the two edges of the plate are fixed and a pushing rod bends the plate from below. The bending creates an elongation

along the metallic wire, which becomes thinner and thinner until it finally breaks (opening process), creating two electrodes with a small gap between. Using the fact that the plate is flexible, the process can easily be reversed by gradually decreasing the bending of the flexible plate until the two electrodes come into contact (closing process), and finally, the metallic junction is reformed. For the analysis of molecular junctions, the small gap formed after the initial rupture of the metallic wire can be used.

The working principle is demonstrated in Figure 2.4: a metallic wire is fixed in a flexible *bending beam*. Here, two epoxy dots are used, but there are other ways to secure the wire (see subsection 3.2.1). The two ends of the wire are used to contact the sample to measure the current flowing through it. Between the epoxy dots, the wire is notched prior to measurement, to make sure it breaks and to define the point of rupture. Employing an initially intact wire that is subsequently ruptured during the measurement process ensures that the electrode surfaces remain clean, presenting a significant advantage over the STM-BJ or AFM-BJ techniques, where the starting point is not in contact. The bending beam slides into the sample holder, so it is seated on top of a *pushing rod* that is connected to a *differential screw* and a piezo actuator. The differential screw is turned by a step motor and performs the *coarse* movement, while the piezo actuator is responsible for the *fine* movement of the pushing rod. The displacement of the pushing rod bends the bending beam, so that the vertical displacement (Δx) is translated into the horizontal elongation of the wire (Δz). The transmission between the vertical movement of the pushing rod and the elongation of the wire can be on the order of 100 ($\Delta z \approx \Delta x/100$), which makes the stability of the MCBJ superior compared to STM-BJ or AFM-BJ.

The stability of the measurement can be further improved by preparing the MCBJ sample using electron-beam lithography. This measurement technique is called the lithographic MCBJ method, because it utilizes the same principle. Thanks to the fabrication technology, the fix points can be very close to each other, their distance can be as low as 100 nm, resulting in a transmission ratio of $\sim 10^{-5}$. The increased stability comes with a cost of increased measurement time; a single opening-closing cycle takes longer to complete. Despite its superior stability, this method is not suitable for statistical analysis because these samples break down in a few thousand opening-closing sequences.

2.2.4 Adding molecules

Upon the rupture of the metallic contact, a small nanogap is formed, which can be used to contact the molecules. The primary challenge lies in introducing the molecules into the system such that they can attach to the newly formed electrodes. In STM-BJ and AFM-BJ setups, the target molecules can be deposited onto the sample surface prior to measurement, however, it is best practice to introduce the molecules after execution of several thousand opening-closing sequences to ensure that the setup is free of contaminants. This is accomplished through the use of in situ molecular dosage techniques.

There are several different methods for in situ molecule dosage; the choice depends on measurement circumstances such as the temperature or the state of matter of the target

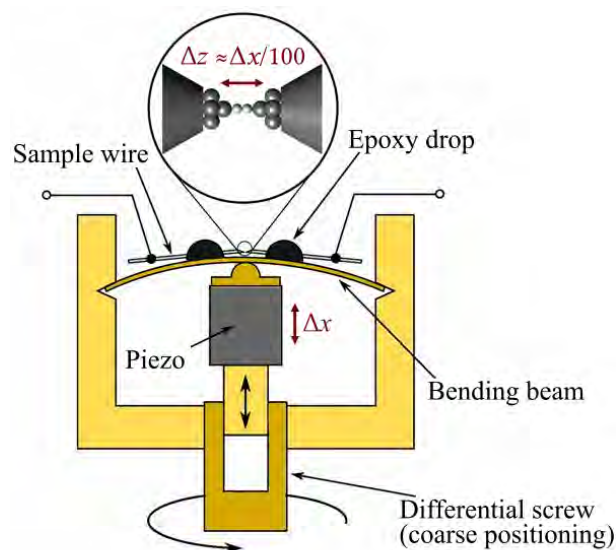


Figure 2.4: Schematics of MCBJ measurement *Cross section of the measurement setup. The wire is fixed to the bending beam by two epoxy drops. The bending beam with the sample wire is bent using a differential screw or a piezo actuator for coarse or fine elongation of the sample wire, respectively. The transmission between the vertical movement of the piezo actuator and the elongation of the wire can be on the order of 100. Source: [38].*

molecule. Some of the in situ molecule dosage techniques are presented in Figure 2.5. Although the illustrations are for an MCBJ sample, these techniques are also suitable for STM-BJ and AFM-BJ samples.

For the dosage of gas-state molecules (e.g. carbon monoxide), heated pipe dosage is a suitable method. The target molecule is in a container and is driven toward the electrodes through an electrically heated pipe, as depicted in Figure 2.5(a). For solid molecules, an example of in situ molecule dosing technique is when we solve the target molecule in an organic solvent (e.g. 1,2,4-trichlorobenzene, mesitylene, etc.) and add a few drops of the solution to the surface of the plate or the metallic wire, for the STM-BJ and MCBJ methods, respectively. For the MCBJ sample, it is crucial to use a fluid cell to contain the solution as depicted in Figure 2.5(b), because otherwise it would flow off of the curved bending beam. This method has the advantage of carrying out control measurements, because the molecule can be added at any point; however, it is not available at cryogenic temperatures. The concentration of the solution plays a crucial role in the pick-up rate, i.e. the ratio of molecular traces to the blank traces after the molecule is added. The in situ evaporation technique is suitable for addressing the temperature restriction of the solution. By placing the target molecule inside a quartz tube and heating it with a filament, the target molecule evaporates onto the surface of the electrodes; see Figure 2.5(c). However, this method does not work with all molecules, only those that have a suitable melting point. In the next chapter, I will discuss this technique in detail when presenting the

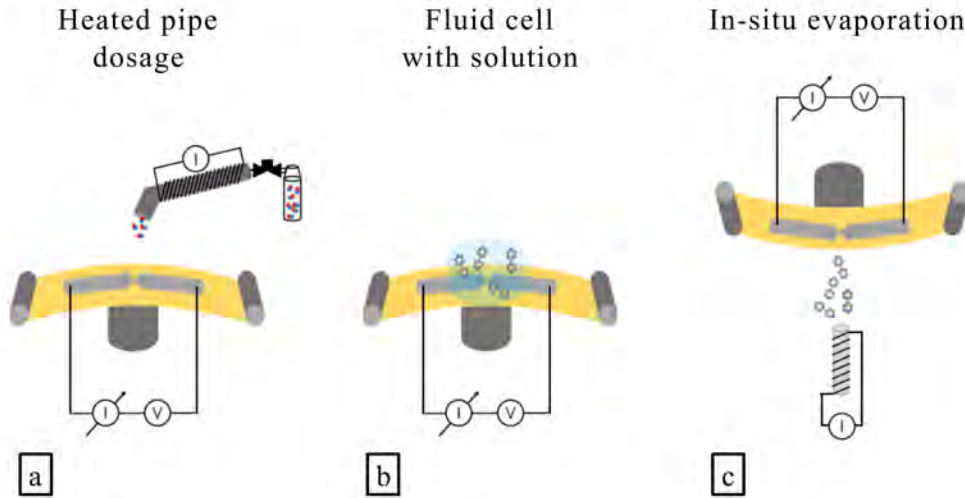


Figure 2.5: Example methods for in situ molecule dosing techniques (a) **Heated pipe dosage.** *This method is used for gas molecules.* (b) **Fluid cell with solution.** *Solid molecules can be added as a solution in an organic solvent. The solution is confined in a fluid cell.* (c) **In situ evaporation** *Solid molecules also can be evaporated on the electrode surface. This method only works with molecules that have a suitable melting point.* Source: [40]

measurement system in the next chapter.

2.2.5 Comparison

Each method has advantages and certain drawbacks, and one has to consider what the goal of the measurement is. In most of my measurements, I used the MCBJ method because of its stability, which was essential for the measurements. I also made some test measurements with our STM-BJ setup, but the results of these measurements are out of the scope of this dissertation. The measurement setup and schemes are described in detail in chapter 3.

2.3 Conduction of nanowires

The key parameter in the study of atomic and molecular contacts is the junction conductance. However, as opposed to macroscopic conductors, Ohm's law – the conductance is directly proportional to the cross-sectional area (S) and inversely proportional to its length (L), σ being the material-dependent conductivity of the sample – ($G = \sigma \cdot \frac{S}{L}$) is no longer applicable on the mesoscopic scale. Depending on the relative size to characteristic length scales (determined by scattering mechanisms), electron transport can be classified into different transport regimes.

One of these characteristic length scales is *phase-coherence length* (L_φ) which measures

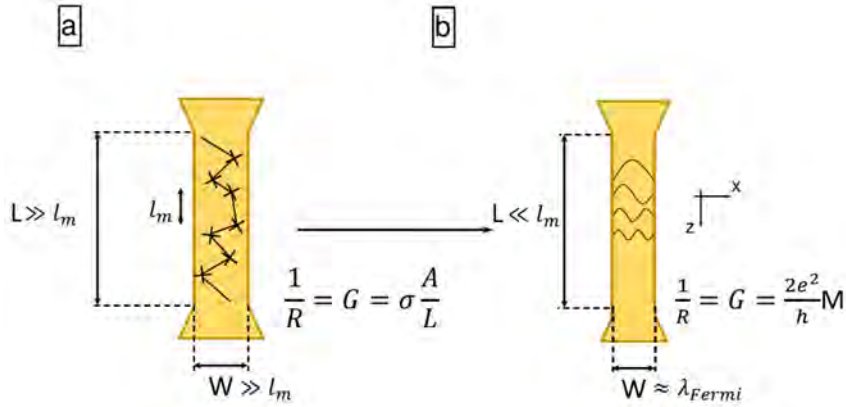


Figure 2.6: Schematics of transport regimes (a) When the length and the width of the wire are larger than the elastic mean free path ($L \gg l_m$, the conductor is diffusive: the electron undergoes several scattering events inside the wire. (b) When the length of the wire is much smaller than the mean free path, the conductor is ballistic and the scattering is limited to the boundaries. Typically, in this length scale, the width of the wire is close to the Fermi wavelength (λ_F) where the electrons are confined in the directions perpendicular to the wire. Source: [40].

the distance over which the phase information of the electron's wave function is preserved. The mesoscopic scale is defined when the typical length scale of the sample (L) is: $L < L_\varphi$. The transport mechanism can be further classified considering the *elastic mean free path* (ℓ), which measures the distance that electrons travel between elastic collisions with static impurities. If $L > \ell$, the conduction regime is called *diffusive*, and the electron motion is like a random walk with a step size ℓ . However, if $L \ll \ell$ the motion of the electron is only limited by the boundaries of the sample and the electron momentum can be considered constant; this regime is called *ballistic*. Another important factor is the width of the wire W : Atomic scale junctions have a width of $W \sim \lambda_F$, where λ_F is the Fermi wavelength, and the *full quantum limit* is reached. [15, 56, 63] The transport regimes and the corresponding conduction mechanisms are depicted in Figure 2.6.

In an *ideal* nanowire (with parallel walls) connecting two macroscopic leads, the electrons move freely along the wire but are confined in the directions perpendicular to the wire by a hard-wall potential. The wavefunction of the electrons is obtained by solving Schrödinger's equation and can be separated into a plane wave along the longitudinal direction and quantized standing waves along the transverse direction. The dispersion relation then is written as:

$$\varepsilon_n(k) = \varepsilon(k) + \varepsilon_n, \quad (2.1)$$

where ε_n is the quantized energy of the discrete transverse modes and $\varepsilon(k) = \hbar^2 k^2 / (2m)$ is the energy that corresponds to the longitudinal plane waves. So we have quantized parabolic dispersion, and taking into account that the maximal energy of electrons in a metal at 0 temperature is equal to the chemical potential (μ), only those n modes are available that cross the chemical potential, these modes are called *open conduction*

channels, as depicted in Figure 2.7(a). An applied bias (V) shifts the chemical potential of the leads, so that $\mu_1 - \mu_2 = eV$, see also Figure 2.7(b). In this case, the current originates from the states between the two chemical potentials, so that the current from a single open conduction channel is $I = (2e^2/h) \cdot V$.

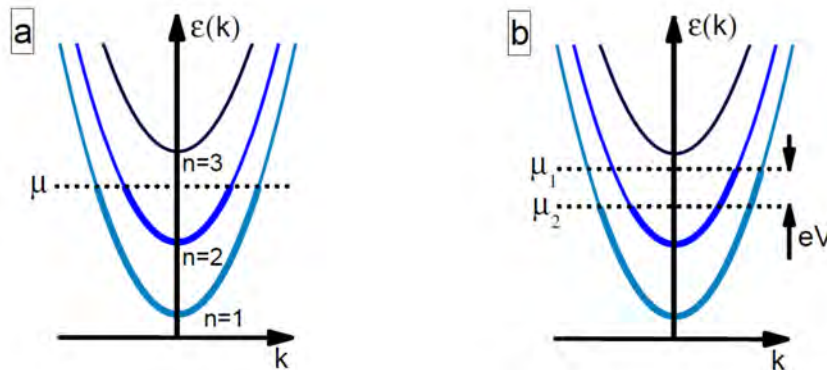


Figure 2.7: Parabolic energy dispersion relations (a) The dispersions that cross the chemical potential are the open conduction channels as highlighted with thicker lines. (b) If a voltage is applied between the two leads, the total current through the wire comes from the range between μ_2 and μ_1 . Source: [39].

Most nanocontacts however, are not ideal, so the above description needs to be modified accordingly. We can consider a nanocontact with arbitrary geometry as a scattering region connecting two wider ideal nanowires, called leads. The probability that an electron from the n th channel of lead 1 to gets through to the m th channel of lead 2 is described by the transmission probability \mathcal{T}_{nm} .

$$G = \frac{2e^2}{h} \sum_{n,m=1}^M \mathcal{T}_{nm}, \quad (2.2)$$

converting to eigenbasis of the transmission matrix, we can rewrite the expression with the transmission eigenvalue \mathcal{T}_n :

$$G = \frac{2e^2}{h} \sum_{n=1}^M \mathcal{T}_n, \quad (2.3)$$

where $G_0 = 2e^2/h$ is the conductance quantum. The Landauer formalism connects the conductance to the transmission eigenvalues, but generally there is no straightforward way to determine the values of \mathcal{T}_n , as it depends on the geometry and electron structure of the contact or even the energy of the electrons. [15, 39]

As the conductance of the contact is a multiple of the conductance quantum, the conductance of an atomic or molecular nanocontact is usually expressed in units of G_0 in measurements. In the case of molecules, the conduction is determined by the number of conduction channels and their individual transmission coefficient.

2.4 Statistical analysis of the conductance of a nano-junction

The formation of atomic and molecular contacts is driven by the self-assembling properties of the material. Due to the stochastic nature of the governing processes, a statistical analysis is necessary to resolve the junction evolution and determine the stable configurations and their conductances. The need for a large amount of data makes break junction techniques fundamental in the analysis of molecular junctions. Through the repeated rupturing and reformation of the junction, which can be performed several thousand times, an extensive dataset is generated that can be statistically analyzed.

2.4.1 Conductance measurements

The primary measurement method in the analysis of nanowires is when we simply apply voltage across the nanowire, while measuring the current flowing through the sample and calculating the conductance of the contact. Using the BJ method, we can measure the temporal evolution of the junction conductance by simultaneously changing the voltage applied to the piezo actuator while measuring the conductance. After the junction ruptured, we can reverse the change of the voltage applied to the piezo actuator, which leads to the reformation of the contact, the rupture–reformation or *opening–closing* process can be repeated, and we can measure thousands of conductance–displacement traces with a single sample. The measurement flow and an example opening/closing trace pair are shown in Figure 2.8. Due to the stochastic self-assembling properties of atomic- and molecular-scale structures, these traces do not reproduce perfectly, and in some circumstances they can be considered statistically independent.

The conductance–displacement traces show plateaus for stable atomic configurations of atomic-scale metallic contacts at values $\geq 1 G_0$, corresponding to stable configurations. It was shown previously that these plateaus correspond to the one- and few-atom-wide nanocontacts. In the case of gold, the single-atom wide atomic wire has a single conduction channel with perfect transmission, so it has a conductance of $1 G_0$. For other metals, the single-atom wide contact has a conductance of the order of $(1 - 3) G_0$. Therefore, the $1 G_0$ conductance value is considered the line that divides the metallic contact region (above $1 G_0$) from the conductance region of the broken wire with a nanogap between the electrode, where conductance is determined by the tunneling current. In this region, conductance depends on the size of the nanogap, but if a molecule is present in the system, a plateau appears when it bonds to the electrodes, at a conductance value $< 1 G_0$, which is specific to the molecule investigated.

The basis of the evaluation of break junction measurements is the study of the *one- and two-dimensional histograms* constructed from the conductance–displacement traces, which give information on the most common conductance values of the given junction. This can be complemented by correlation analysis, where we calculate the correlation of different configurations.

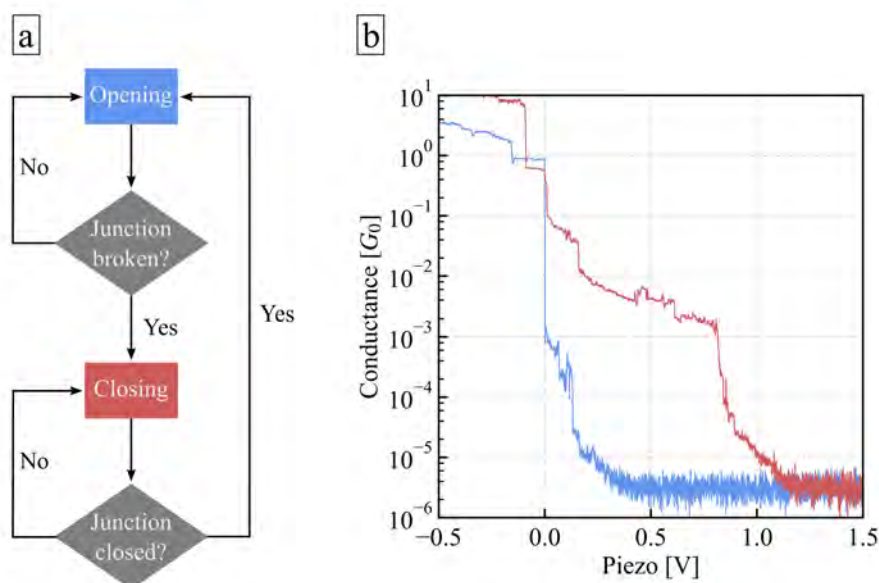


Figure 2.8: Conductance measurement flow chart (a) Flow chart of break junction measurements. The contact is elongated, until the junction finally ruptures i.e. the conductance falls below a threshold, typically $10^{-5} G_0$, then, the contact is closed back (until the conductance increases above a threshold, typically $10 G_0$) by reversing the movement. **(b) Example conductance trace pair.** The trace colors correspond to the color of the rectangular process boxes in the flow chart, blue for the opening and red for the closing process. The conductance traces are shifted along the horizontal axis, so that the rupture of the single-atomic contact is at 0 V.

2.4.2 Conductance histograms

The first step of the analysis is to calculate the 1-dimensional conductance histograms (1D histograms) (see Figure 2.9 for step-by-step demonstration). For this, we first define the conductance bins in the relevant conductance range. As in the tunnel and molecular region, the conductance changes exponentially with distance, we need to define these bins logarithmically equidistant to account for the exponential change in conductance. (This is equivalent to a linearly binned histogram of the logarithm of conductance, but we mostly use the conductance for convenience.) In this example, I defined the number of bins to be 20 bins / decade, that is, a total of 120 bins in the conductance range ($10^{-5} - 10$) G_0 . Then we count the number of points in each bin to calculate the *single histogram* for a single trace (see example traces and single histograms Figures 2.9(a) and 2.9(b)). The blue traces and histograms correspond to measurements performed with clean gold wires, while the red ones correspond to molecular measurements with 4,4'-bipyridine. Finally, we sum up the single histograms and normalize them with the number of traces to calculate the total histograms (Figure 2.9(c)).

When one looks at the example traces and the calculated histograms, the difference

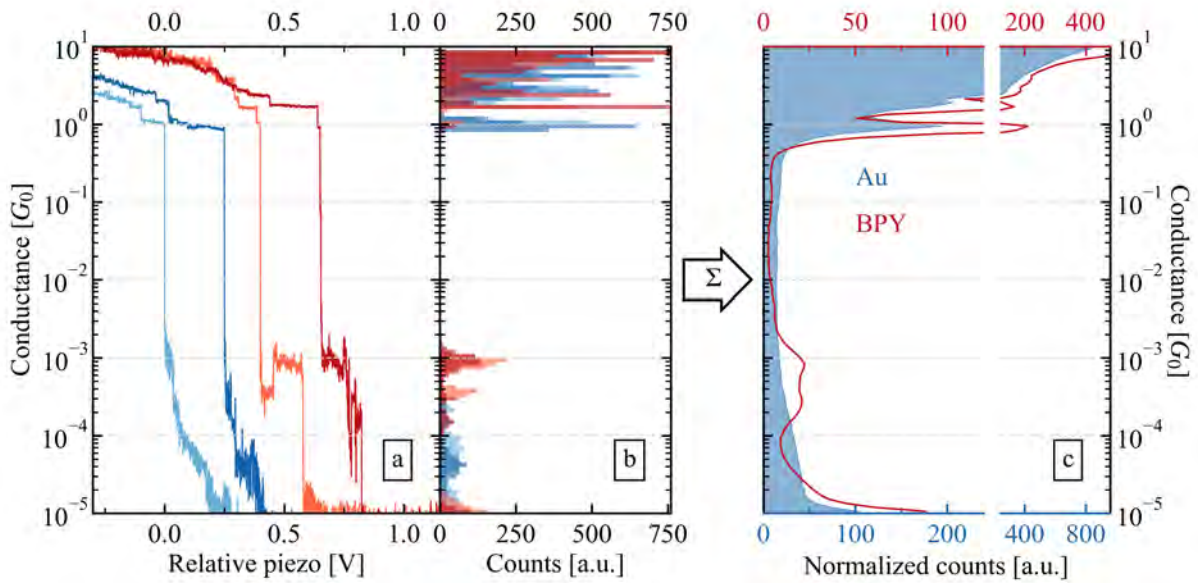


Figure 2.9: Creation of 1D conductance histograms. (a) Example conductance-displacement traces from clean (Au) and molecular (BPY) measurements. The traces are aligned so that they cross $0.1 G_0$ at a relative piezo voltage of zero and from the second trace, each is shifted by an additional 0.25 V for visibility. Blue colors correspond to clean measurements and red colors to molecular measurements. (b) Single histograms, created by counting the points in each logarithmically equidistant bin along the conductance axis. Colors correspond to the trace colors in (a). (c) Total histograms by summing up the single histograms for each trace and normalizing by the total number of traces.

between tunnel traces and molecular traces is significant: following the $1 G_0$ plateau (the rupture of the metallic contact), the tunnel traces show exponentially decreasing conductance, while the molecular traces have plateaus at distinct conductance values. This feature is reflected in the histograms in Figures 2.9(b) and 2.9(c): the counts in the bins around the plateaus are naturally higher, resulting in peaks in the single and total histograms that stand out from the background. For 4,4'-bipyridine this means that in the one-dimensional conductance histogram there are two peaks (see dark red line-plot in Figure 2.9(c)) around the two most common conductance values for the HighG and LowG configurations, respectively.

2.4.3 Conductance–displacement histograms

To resolve the loss of the displacement information in 1D conductance histograms, we also look at the 2-dimensional conductance–displacement histograms (2D histograms) [64, 65], where we not only use the logarithmically equidistant bins for the conductance axis, but we also divide the displacement axis into equal-size bins to calculate a heatmap of all the

traces. Using this analysis method, we can see the characteristic conductances at different electrode displacements.

To calculate the 2D histograms, we first align the traces so that they cross a reference conductance (G_{ref}) at the 0 V relative piezo voltage (see the example trace in Figure 2.10, where $G_{\text{ref}} = 0.1 G_0$). The choice of the reference conductance value depends on the objective of the analysis, but generally we choose values where the conductance in the single traces changes abruptly, e.g. between two conductance plateaus, because the result is less susceptible to small fluctuations of the conductance. Then we count the points of the conductance–displacement traces in each individual area defined by the vertical and horizontal bins and plot them as a heatmap. In this case, low counts are white, while large counts correspond to dark blue, as denoted on the colorbar in each subfigure. If we connect the bins with the highest count, the resulting curve can be considered as an average opening trace. Again, the difference between the tunnel and the molecular 2D histograms is striking: if a molecule is present, the rupture of the atomic contact is followed by a molecular plateau that appears as a well-defined spot in the 2D histogram in the same conductance range where a peak is visible in the 1D histogram.

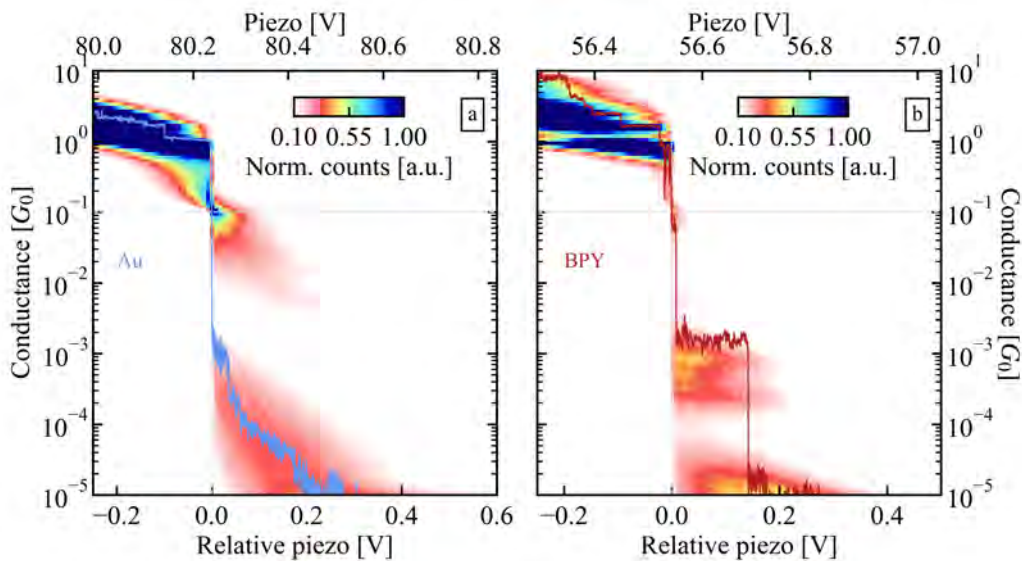


Figure 2.10: Creation of 2D conductance–displacement histograms. (a) *Calculated conductance-displacement 2D histogram for clean (Au) measurements with a representative example trace with light blue.* (b) *Calculated conductance-displacement 2D histogram for molecular (BPY) measurements with a representative example trace with dark red.*

Keeping the displacement information, we get a sense of the length of the molecular plateaus. However, it is important that the rupture of the metal contact is followed by a *snapback* of the gold electrodes, resulting in an increased gap between the electrodes that is around (0.6–0.8) nm [13], so we must also account for this distance.

2.4.4 Correlation of conductance traces

After the presence of the molecule was confirmed with the statistical methods discussed above, we might want to go further in the analysis of the configurations. Makk et al. introduced the correlation analysis technique to study the relationship between different binding configurations, as well as the structural memory effects of molecular junctions. In this method, the correlation is calculated for the histogram bin counts of the single-trace histograms. The equation for the elements of the correlation matrix is as follows:

$$C_{i,j} = C(G_i, G_j) = \frac{\langle (N_i(r) - \langle N_i(r) \rangle) \cdot (N_j(r) - \langle N_j(r) \rangle) \rangle}{\sqrt{\langle (N_i(r) - \langle N_i(r) \rangle)^2 \rangle \cdot \langle (N_j(r) - \langle N_j(r) \rangle)^2 \rangle}}, \quad (2.4)$$

where $C_{i,j}$ is the value in the i th row of the j th column of the correlation matrix, $N_i(r)$ ($N_j(r)$) is the number of counts in the bin i (j) on trace r (that is, the single histogram of trace r) [34]. An example correlation plot for Au-2,7-diaminofluorene-Au molecular contacts is shown in Figure 2.11 ((c)). The dataset was measured with an STM-BJ setup in solution of the 2,7-diaminofluorene molecules at room temperature. The molecular conductance traces give two plateaus in the molecular region, which correspond to two distinct configurations. In addition to the perfect correlation (red) along the diagonal, several other correlated conductance regions are visible. Correlated regions reveal how different regions relate to each other: e.g. the negatively correlated region (blue shades) at $1 G_0$ conductance in the correlation plot suggests that the longer the $1 G_0$ plateau, the fewer counts we get in the lower conductance regions, i.e. the shorter the molecular plateaus are. This can be attributed to the snapback length mentioned previously: when a well-stretched single-atom junction, or a single-atom chain ruptures, the resulting gap between the electrodes may be so large that the molecule barely bridges the gap, resulting in a short molecular plateau, or it can not even incorporate because the gap is larger than the size of the molecule. Looking at the conductance regions that correspond to the two configurations of the molecular contacts, we see that the configurations are also negatively correlated. This can be interpreted in two ways: either one of the configurations occurs but then the other does not; or both plateaus appear but one of the plateaus is long and the other is short. This shows that interpreting 2D correlation matrices is a complex task that often requires experience and additional evaluation steps, such as trace selection [33, 34, 42, 43, O1, 66].

Hamill et al. introduced an approach to reduce the complexity by focusing on the most important correlations that are defined by the eigenvectors of the correlation matrix, the principal components (PCs) $P_i^{(n)}$, sorted in descending order by the corresponding eigenvalue, denoted by the index n [67]. Principal components capture the maximum possible variance in the data and enable an approximation of the original dataset using only a few key components [68]. This simplification aids in understanding junction evolution on its own or when combined with the categorization of traces into groups based on their properties.

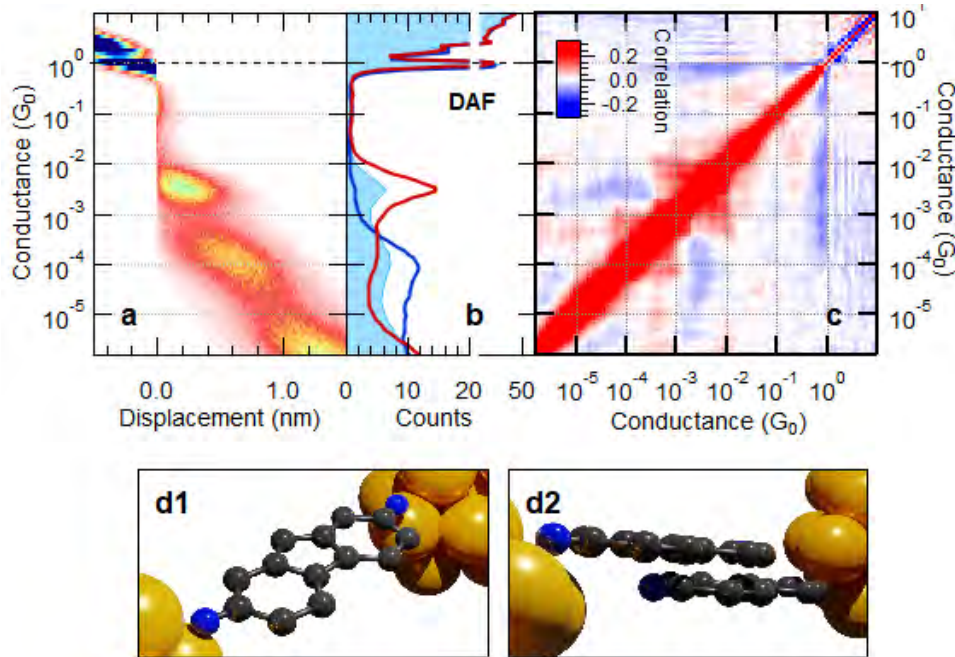


Figure 2.11: Statistical analysis and configurations of Au-2,7-diaminofluorene-Au molecular junctions (a)-(c) 2D conductance-displacement, 1D conductance histogram and correlation plot, respectively, for gold break junction measurements with 2,7-diaminofluorene molecules. In panel (b) the light blue area graph is the 1D histogram of the entire dataset, while the red and blue lines represent the histograms of the data subsets obtained by EPCP analysis (see subsection 2.4.5). (d) The illustration of HighG (monomer) configuration and LowG (dimer) configuration of the 2,7-diaminofluorene molecule. Source: [P2].

2.4.5 Trace selection techniques

In the above examples, the measured conductance traces were studied in one large group, but this often leads to important characteristics being lost in the blend. In a typical experiment, thousands of traces are measured; depending on the molecular pick-up rate, some of them show molecular features, while others do not. Sometimes that is enough to statistically describe a set of traces, but more often the analysis can really benefit from a preselection of the desired traces from the whole dataset. The selection cases are diverse: there are some general selection targets, like selecting traces showing molecular features. For example, we want to study how the presence of a molecule changes the transport mechanism in comparison to the clean metallic measurements. Traces without molecular features can alter the statistics and hide important features. Similar to the selection targets, the selection methods can also be highly specific: for example, a simple method involves grouping traces based on whether the number of conductance plateaus within a given conductance range is higher or lower than average for the actual trace (conditional histogram method) [42], but the selection can also be performed using

other parameters; for instance, Makk et al. used the so-called plateau length histogram to group conductance traces by the number of Pt atoms pulled from the electrodes into the active region of the contact [35]. Furthermore, novel machine learning approaches are also possible [69, 70, O2], which can eliminate the disadvantages of manually defined constraints: such constraints can become quite tedious because they presume prior knowledge of the (un)desired characteristics, and one has to take into account each feature individually and define clever filters for non-trivial criteria [41]. Classification tasks are where machine learning algorithms shine; however, they also have significant downsides. Unsupervised machine learning algorithms are like black boxes; we do not know what happens under the hood, and which characteristics determine the outcome of classification. Supervised machine learning algorithms require manually selected training and test sets, and the creation of these is not only time-consuming but also prone to human error. Manual selection can be bypassed if we utilize the principal components to use the internal correlations to select traces that show a characteristic trait of the whole dataset [46, 67]. This was first demonstrated on artificially mixed traces measured with molecules that had identical anchor groups and similar lengths, but one had π (high conductance), while the other had σ (low conductance) bridge [67].

In cases where the goal is not to classify the entire dataset but rather to identify representative traces that reflect distinct behaviors, the extremal principal component projection (EPCP) method can be highly effective. It provides an alternative to manual selection without requiring the complexity of advanced machine learning algorithms. The principal component projection of a given conductance trace is calculated as $PCP^{(n)}(r) = \sum_i P_i^{(n)} \cdot N_i(r)$, i.e., the scalar product of the n th principal component vector and the histogram of the individual trace. Since this projection can take both positive and negative values, one could, in principle, classify traces by the sign of their projection. However, the EPCP method takes a different approach: it selects the top N traces with the largest positive and negative projection values, respectively. The value of N is typically chosen as a small fraction (e.g., 10–20%) of the total number of traces. For example, in Figure 2.11(b), the red and blue curves show the conductance histograms for such EPCP-based selections applied to the 2,7-diaminofluorene molecule, using the second principal component and selecting 20% of traces in each direction. One selection clearly emphasizes the HighG configuration and suppresses the LowG configuration, while the other shows the opposite behavior. This indicates that this method is well-suited for separating traces that exhibit only one of the characteristic molecular configurations.

2.5 $I(V)$ characteristics measurements

When recording the conductance–displacement traces, the current flowing through the system is measured while a constant bias voltage is applied, so we can study the current (conductance) changes while the individual configurations are formed. This method is ideal for studying structural changes, but falls short when a deeper understanding of the

configurations is desired. In this case, other measurement methods need to be applied.

An example is the current–voltage ($I(V)$) characteristics measurement, which plays an important role in the investigation of molecular systems, as it shows how the current flowing through the molecule changes as a function of the applied bias voltage, giving fundamental information about the conduction mechanism.

Current–voltage measurements typically exhibit non-linear $I(V)$ characteristics, which are attributed to the quantum properties of molecules, the tunneling nature of the conduction mechanism, and the discrete energy levels (molecular orbitals). By fitting the $I(V)$ curve and comparing the result with numerical models, the parameters that describe the molecular system can be extracted. The investigation of $I(V)$ characteristics is especially important when studying molecules that demonstrate switching or memristive behavior.

2.6 Noise spectroscopy of molecular junctions

Noise is typically characterized as an unintentional temporal deviation from the mean value within a measurement, such as that of an electric current, and is frequently regarded as a disturbing factor that should be suppressed. Nonetheless, in certain instances, noise can manifest as a valuable signal from which useful information can be extracted, thereby helping to get a more comprehensive understanding of the system under investigation. Consequently, the analysis of noise constitutes a compelling area of research, particularly for nano- or atomic-scale devices because their extremely small active region is particularly susceptible to deviations. The significance of this field is underscored by numerous related publications from our research group, which have examined noise phenomena across various nano devices [P2, P3, 71]. In this section, I briefly present the experimental interpretation of noise, along with the fundamentals of noise measurements, with an emphasis on $1/f$ -type noise measurements and the insights their examination yields.

2.6.1 Basics of noise measurements

Noise is the random deviation of some physical quantities from their mean values, which can also vary over time in a non-random manner. [25] The electronic noise of single-molecule junctions can be separated into high- and low-frequency noise, and the latter originates from the metal atoms rearranging on the electrode surface and also the fluctuating microenvironment of the molecular junction. Based on its frequency dependence, low-frequency noise is further categorized as flicker noise ($\sim 1/f$) and random telegraph noise (RTS, $\sim 1/f^2$). [31] Previous studies indicate that flicker noise exhibits a power-law dependence on junction conductance, and this scaling has great potential to be utilized as a probe for electrode-molecule coupling. [29, 30, 72]

2.6.2 Description of noise

Every measured quantity has a noise that can be defined as time-dependent fluctuations from the mean value. Experimentally, for example, in the case of current noise, the mean squared deviation, $\langle \Delta I(t)^2 \rangle$ can be obtained in a Δf frequency window around the f_0 central frequency, yielding $\langle \Delta I(t|f_0, \Delta f)^2 \rangle$. For a small enough Δf frequency window, the relation

$$\langle \Delta I(t|f_0, \Delta f)^2 \rangle = S_I(f_0) \cdot \Delta f \quad (2.5)$$

holds up where the proportionality factor $S_I(f_0)$ is the *spectral density of noise*, or the *noise power spectral density* (PSD) defined at f_0 frequency. Consequently, the mean squared deviation of the current is given by the integral of the spectral density over the whole frequency range:

$$\langle (\Delta I)^2 \rangle = \int_0^\infty S_I(f) df. \quad (2.6)$$

The theoretical description of the noise is given by defining the autocorrelation function:

$$C_I(t_2 - t_1) = \langle \Delta I(t_1) \cdot \Delta I(t_2) \rangle, \quad (2.7)$$

which evaluates the correlation between a signal and its time-delayed self. The Wiener–Khinchin theorem describes the connection between the power spectral density and the Fourier–transformed correlation function [25]:

$$S_I(f) = 2 \cdot C_I(\omega) = \int_{-\infty}^\infty C_I(\Delta t) \cdot \exp(-i\omega\Delta t) d(\Delta t). \quad (2.8)$$

However, as the measured signal is not continuous but discretely sampled, the noise PSD is typically derived by performing a discrete Fourier–transform on the measured current fluctuation:

$$S_I(f) = \left\langle \frac{2\Delta t}{N} \cdot \left| \sum_{n=0}^{N-1} \Delta I(n\Delta t) \exp(-i2\pi f n\Delta t) \right|^2 \right\rangle, \quad (2.9)$$

where Δt is the time difference between adjacent acquisition events and N is the total number of analyzed data points and is a power of 2. In practice, to determine the PSD, the measured signal is divided into P segments (each consisting of N datapoints, where N is a power of 2). Then, the Fast Fourier Transform (FFT) of each individual segment is calculated, the resulting spectra are then averaged to obtain the PSD. [73]

The resulting spectrum describes the frequency-dependent characteristics of current noise in the system and allows the analysis of the amplitude of individual frequency components. However, when the object is to compare different systems, conductance states, or driving conditions without focusing on a specific frequency, it is useful to introduce the concept of *noise power*, defined as:

$$N_p = \int_{f_1}^{f_2} S_I(f) df, \quad (2.10)$$

and its normalized square root, the *relative current fluctuation*:

$$|\Delta I|/I = \frac{1}{\langle I \rangle} \sqrt{\int_{f_1}^{f_2} S_I(f) df}. \quad (2.11)$$

Taking into account the noise properties and instrumental limitations, the frequencies f_1 and f_2 can be chosen such that the resulting relative current fluctuation provides a representative characterization of the physical system.

It is important to note that at low voltages, the I(V) curve is linear, and the drive voltage does not excite fluctuations; then Ohm's law is valid, and the relative current, resistance, and conductance fluctuations (*relative noise*) are equal: $\Delta I/I = \Delta R/R = \Delta G/G$.

2.6.3 Relevant noise mechanisms in single-molecule systems

Thermal noise

The *thermal noise*, which is also known as *Johnson-Nyquist noise* (after the experimentalist and the theorist who investigated it [74, 75]), is an equilibrium phenomenon governed by statistical thermodynamics. The temporal noise comes from the thermal motion of the electrons in any conductor and is present even without applied bias. For a resistor R at an absolute temperature T the current noise PSD is given by:

$$S_I = \frac{4k_B T}{R}, \quad (2.12)$$

where k_B is the Boltzmann constant. This type of noise is classified as *white noise* because it does not depend on the frequency. Temporal noise is present even with an applied bias of 0 V and does not change even at a higher bias. Thermal noise sets the fundamental and theoretical noise and is referenced as the base noise level. In cases when instrumental noises are suppressed, this is the base level of the system. If calculated for a 1 G_0 conductor at room temperature (~ 300 K), the temporal noise is $\sim 1.28 \cdot 10^{-24}$ A²/Hz, while for molecular contacts it is 3-4 orders of magnitude smaller.

Shot noise

The non-equilibrium fluctuations known as *shot noise* are caused by the discreteness of the charge of the carriers of the electrical current. The electrons are transmitted independently from each other through the barrier, leading to a frequency-independent current noise density proportional to the mean current:

$$S_I = 2e\langle I \rangle. \quad (2.13)$$

Shot noise is also independent of the frequency, but not of the applied bias. At zero applied bias, the value of the shot noise is 0, but if the bias is increased, the shot noise

Chapter 2. Literature Review

increases too. For a typical applied bias of 100 mV, for a $1 G_0$ conductor, the shot noise level is $\sim 2.5 \cdot 10^{-24} \text{ A}^2/\text{Hz}$, and again, for molecular contacts it is 3-4 orders of magnitude smaller.

However, it is important to note that this is a theoretical maximum value for the shot noise, and it is only true if the charge carriers follow the ideal Poisson distribution, which means that the electrons are transmitted randomly, independent of each other. In our measurements, in the frequency range covered and with the typical applied biases, the shot noise level is hidden by the temporal, instrumental, and the $1/f$ -type noise.

$1/f$ -type noise (flicker noise)

Named after its characteristic frequency dependence, $1/f$ -type noise (also called *flicker noise*) originates from resistance fluctuations in or close to the active region of an electronic device (see Figure 2.12). In metals, resistance fluctuation is induced by electrons scattering on dynamic fluctuators, such as atoms that fluctuate between metastable positions, as shown in the inset in the top right corner of Figure 2.12(b).

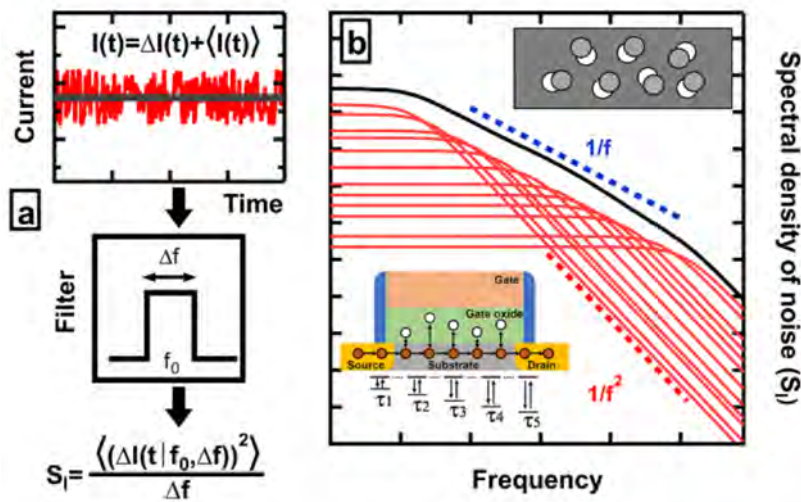


Figure 2.12: Origin of the $1/f$ -type noise. (a) **Fluctuating current signal.** The fluctuating current signal is the sum of its mean value and the $\Delta I(t)$ noise around the mean. By decomposing the signal, we can obtain the mean value and the noise. Calculating the mean squared deviation of the noise in a frequency band Δf around an f_0 central frequency and normalizing by Δf , we obtain the power spectral density of the noise (S_I). (b) **Lorentzian spectra of individual fluctuators.** Red curves show individual contributions to the overall noise. At low frequencies they are constant, but at higher frequencies they scale with $1/f^2$ as indicated with the dashed red guide. The sum shows shallower frequency dependence as indicated with the dashed blue guide. Image taken from [P3].

The contribution of a single fluctuator with characteristic time τ is a Lorentzian spectrum that is constant in the low frequency limit and scales with $1/f^2$ at higher frequencies.

The Lorentzian spectra of a collection of fluctuators (red curves) and their sum (black curve) are shown in Figure 2.12(b). Adding up the contributions of many fluctuators results in a shallower frequency scaling: the sum scales with $1/f$, as illustrated with the blue dashed guideline.

The noise power of flicker noise is proportional to $1/f^\gamma$, where the γ exponent is usually close to 1:

$$S_G(f) = \beta \cdot \left(\frac{f_0}{f}\right)^\gamma. \quad (2.14)$$

In contrast to frequency-invariant thermal or shot noise, flicker noise strongly depends on the frequency.

2.6.4 Exploring flicker noise in single-molecule junctions

In their article Adak et al. proposed the utilization of flicker noise to study coupling at the metal–molecule interface. They studied the origin of flicker noise in single-molecule junctions and found that flicker noise is the result of configuration changes in the electrode structure due to electrode atoms proximal to the junction fluctuating between metastable positions [29].

A simple model of the conductance of a single-molecular junction can be written as follows:

$$G = G_0 \cdot \frac{\Gamma_L \Gamma_R}{\epsilon^2}, \quad (2.15)$$

where $\Gamma_{L/R}$ are the coupling strengths of the left and right electrodes, respectively; and ϵ is the energy difference between the frontier molecular orbital and the Fermi level [56]. If we consider the coupling strength of the two electrodes to be the same and approximate its value as exponentially decaying with the electrode distance: $\Gamma_L = \Gamma_R = \Gamma_0 \cdot \exp(-\beta z)$, where Γ_0 is a constant, β is the decay factor and z is the separation of the coupled sites, ?? can be written as:

$$G = G_0 \cdot \frac{\Gamma_0^2 \cdot \exp(-2\beta z)}{\epsilon^2}. \quad (2.16)$$

In through-space coupling, we consider the conductance fluctuations to originate from the fluctuations in the separation z , while the coupling Γ_0 is fixed. The conductance noise power is then calculated as follows:

$$\begin{aligned} \Delta G^2 &= \left(\frac{\partial G}{\partial z}\right)^2 \cdot \Delta z^2 = (2\beta)^2 \cdot \left(G_0 \cdot \frac{\Gamma_0^2 \cdot \exp(-2\beta z)}{\epsilon^2}\right)^2 \cdot \Delta z^2 = \\ &= (2\beta \Delta z)^2 \cdot G^2, \end{aligned} \quad (2.17)$$

resulting in $\Delta G^2 \sim G^2$ scaling of the conductance noise power, which can be converted to the basis of the commonly used relative conductance noise:

$$\frac{\Delta G}{G} = 2\beta \Delta z, \quad (2.18)$$

Chapter 2. Literature Review

that is, the relative conductance noise does not depend on the conductance in through-space coupled systems.

In through-bond coupling, the conductance fluctuations originate from the fluctuations of the coupling strength (Γ_0), while the separation (z) is fixed. If we calculate the noise power as previously:

$$\begin{aligned}\Delta G^2 &= \left(\frac{\partial G}{\partial \Gamma_0}\right)^2 \cdot \Delta \Gamma_0^2 = 4 \cdot \left(G_0 \cdot \frac{\Gamma_0 \exp(-2\beta z)}{\epsilon^2}\right)^2 \cdot \Delta \Gamma_0^2 = \\ &= 4 \cdot G \cdot \Delta \Gamma_0^2,\end{aligned}\tag{2.19}$$

resulting in $\Delta G^2 \sim G$ scaling of the conductance noise power. We can again convert this to the relative conductance noise:

$$\frac{\Delta G}{G} = 2\Delta \Gamma_0 \cdot G^{-0.5},\tag{2.20}$$

which results in $\Delta G/G \sim G^{-0.5}$ scaling.

Equations 2.17 and 2.19 indicate that the flicker noise behavior of single-molecule junctions is influenced by the molecule–electrode coupling and this phenomenon can be utilized to differentiate between *through-space* and *through-bond* coupling, as demonstrated by Adak et al. [29].

Using their STM–BJ measurement setup to contact molecules, they conducted measurements at room temperature on 3 different organic molecules with the same anchor groups (see Figure 2.13(a) for the chemical structure of the molecules studied). These molecules were hypothesized to couple differently to the gold electrodes because of the placement of their anchoring group and their structure. Molecule 1 forms stable Au–single-molecule–Au bonds through the linker groups, so it is a good example for through-bond coupling. Molecule 2 also forms bonds through the linkers, but as one of the linker is positioned differently, charge transfer is mediated by through-space interaction on that side. Molecule 3 also conducts by through-bond connection. First, they made simple break-junction measurements to determine the average conductance of the molecular configurations using the 1D conductance histograms. These histograms are shown in Figure 2.13(b), and a representative molecular trace is plotted in the inset for each molecule. The colors of the plots correspond to the colors of the molecular structures in Figure 2.13(a).

To measure the noise, they modified the measurement by introducing a *hold* period, where they paused the junction elongation for 100 ms after pulling a fixed distance, where it was most likely that a molecular junction formed. In Figure 2.13(c), they show a representative conductance versus time trace (red) measured with this method along with the displacement of the tip (blue). In the hold period where the displacement is constant, the conductance is recorded at an applied bias voltage of 200 mV and with a sample rate of 100 kHz. After 100 ms, the displacement of the tip continues with the same speed, until the junction breaks. Then, the metallic contact is reformed, to repeat the measurement. From all of the measured traces, only those are selected for further analysis that have a

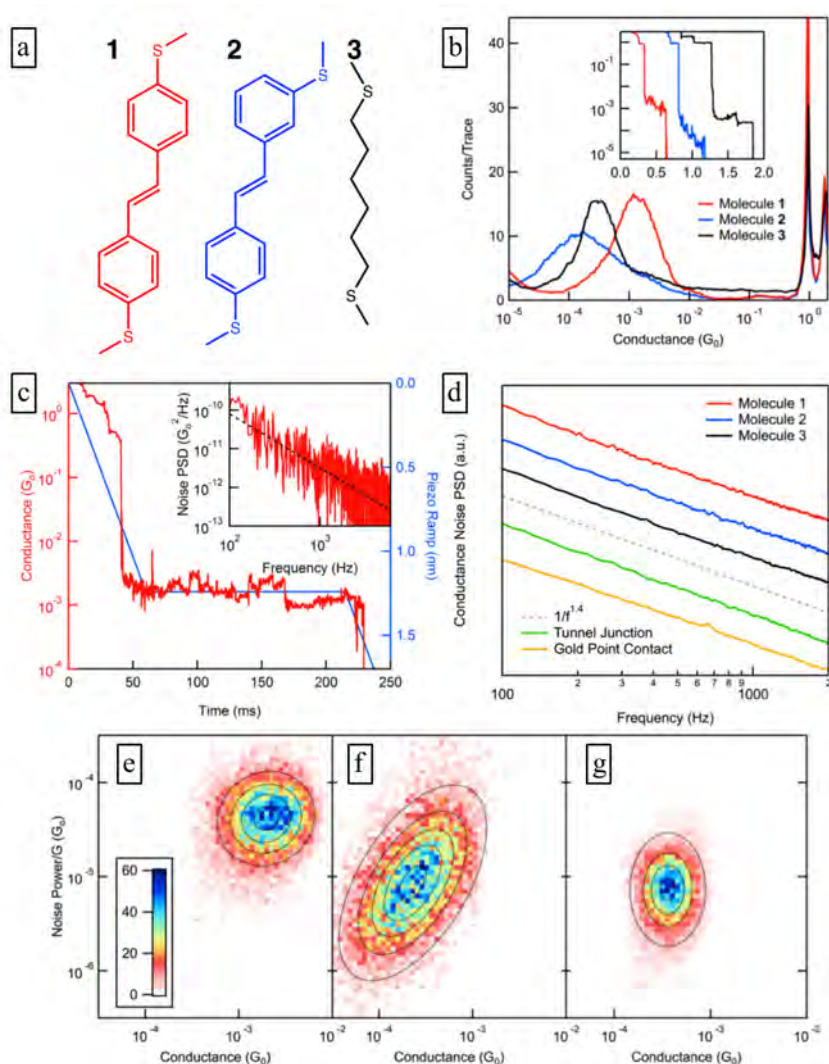


Figure 2.13: Flicker noise as a probe of electronic interaction at metal–single-molecule interfaces (a) Chemical structures of target molecules. (b) 1D histograms for the molecules studied. The color of the histograms corresponds to the colors of the molecular structures in panel (a). The inset contains representative traces for each molecule. (c) Representative conductance and displacement vs. time traces for a single noise measurement. Inset: Conductance noise PSD calculated for the constant displacement section in the main plot. (d) Averaged conductance noise PSDs. The colors correspond to the studied molecules in panel (c) and the average PSDs of a tunnel junction and gold point contact is added for comparison (green and yellow lines). (e)–(g) Two-dimensional histograms of the normalized flicker noise power versus the average junction conductance for molecules 1-3, respectively. Source: [29]

conductance within two standard deviations of the molecular conductance histogram peak at the beginning and end of the hold period. Next, for each trace, they calculated the

Chapter 2. Literature Review

noise power spectral density (PSD), by Fourier transforming the conductance measured during the fixed displacement portion. They plotted the noise PSD of the example trace for molecule 1 in the inset of Figure 2.13(c). For the selected traces, they also calculated the averaged PSDs for each molecule and compared them to the averaged PSDs of tunnel junctions and gold point contacts. Each averaged PSD scales with $f^{-1.4}$, so they argued that flicker noise originates from the electrodes and not the system that bridges them.

From the noise PSD, the conductance noise power is extracted by integrating over the frequency range from 100 Hz to 1 kHz. They calculated the two-dimensional histogram of the flicker noise power normalized by the average junction conductance (G_{AVG}) against the average conductance for each molecule, these are displayed in Figures 2.13(e) to 2.13(g). The normalized flicker noise power observed for molecules 1 and 3 does not vary with changes in junction conductance (scale with $G^{1.1}$ and $G^{1.0}$, respectively), while molecule 2 shows a strong correlation with it (with a $G^{1.7}$ scaling).

In conclusion, the study revealed the relationship between the normalized noise power and the average conductance of the junction. The normalized noise power scales with the power of the conductance: G^n , where the exponent n indicates the coupling type: $n \approx 1$ for through-bond, $n \approx 1.5$ for mixed coupling, and $n \approx 2$ for through-space coupling.

In another study, Magyarkuti et al. used the same technique to differentiate between monomer and stacked dimer molecular junctions [30]. In monomer junctions, one single molecule couples to the electrodes through the linkers, while dimer junctions are formed when the electrodes are bridged by two molecules coupled through a molecule–molecule interaction. They used STM-BJ setups to study 2 molecules, DAT (4,4"-diamino-*p*-terphenyl) and DAF (2,7-diaminofluorene) (see molecular structures in the insets of Figures 2.14(a) and 2.14(c), respectively) at room temperature. They added the molecules in solution and also studied different concentrations. First, they calculated 1D histograms to determine junction conductances (right panels in Figures 2.14(a) and 2.14(c)), found two conductance peaks for both molecules (denoted by arrows) and hypothesized that the lower peak corresponds to dimer junctions. They also calculated the 2D histograms (Figures 2.14(a) and 2.14(c)) from which they concluded that in the junction evolution monomer junctions are formed first and then, increasing the electrode separation, the formation of dimer junctions follows.

To study the flicker noise of these molecules, they performed the same measurement as explained above, only the hold portion was longer (150 ms). By analyzing the 2D histograms of normalized noise power versus conductance, they found that the noise power of the monomer junctions scales with $G^{1.16}$ and $G^{1.05}$ and of the dimer junctions $G^{1.76}$ and $G^{1.78}$ for DAT and DAF, respectively. For the monomers, the scaling exponent is close to 1, indicating through-bond coupling between the molecule and the electrodes, while for the dimers, this value is close to 2, indicating through-space coupling between the two molecules, which is in agreement with their hypothesis.

In summary, this method introduced great potential in the utilization of noise as a probe of the metal-molecule coupling. However, because of the fixed distance elongation before the hold period of the measurement, it also has limitations. Although they statis-

tically determined the distance that most likely results in a molecular junction, a portion of the traces must be discarded because they do not show molecular features.

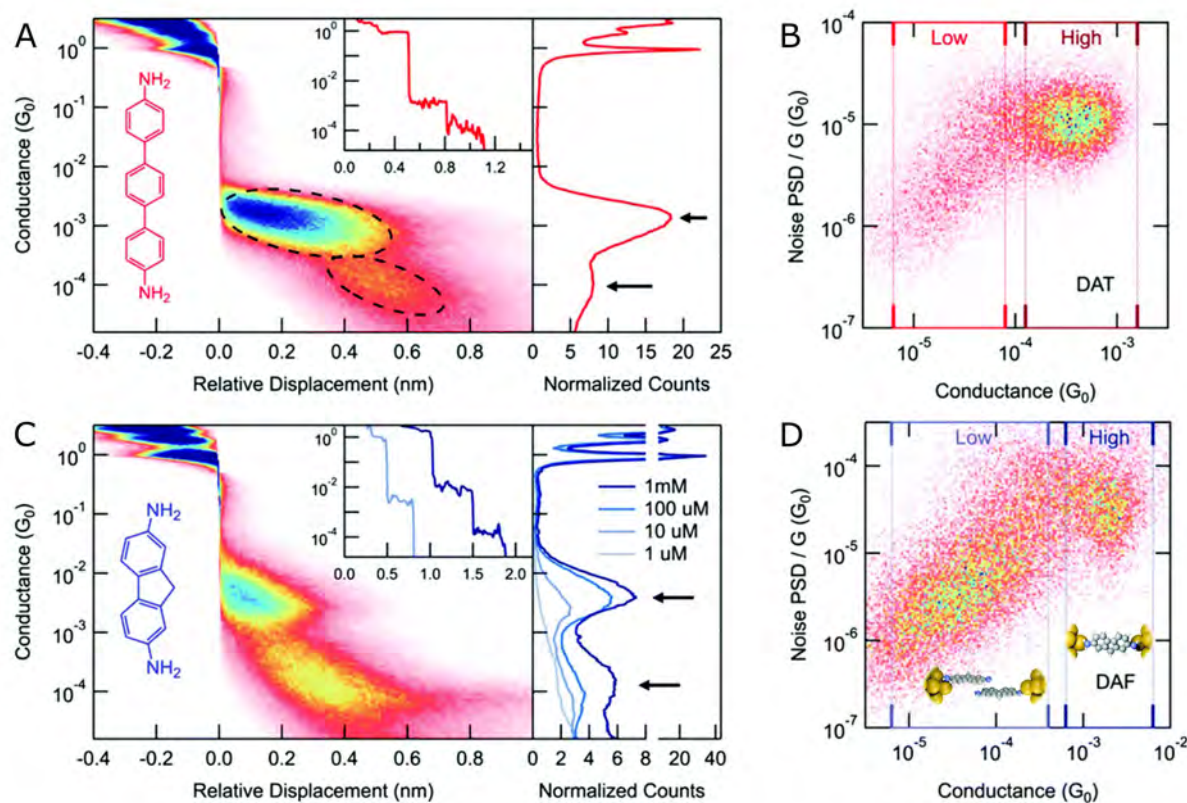


Figure 2.14: Characteristics of stacked dimer molecular junctions. (a) Statistical analysis of the conductance traces of DAT. *Left: 2D conductance–displacement histogram of the traces aligned at $0.5 G_0$. Molecular structure and representative conductance trace displayed in the insets.* (b) 2D histogram of noise power versus conductance for the hold portions of the measurements for DAT. (c) Statistical analysis of the conductance traces of DAF. *Left: 2D conductance–displacement histogram of the traces aligned at $0.5 G_0$. Molecular structure and representative conductance trace displayed in the insets.* (d) 2D histogram of noise power versus conductance for the hold portions of the measurements for DAF. *The inset shows the illustration of the dimer and molecular configurations.* Source: [30]

Pan et al. introduced a method to bypass the limitations of the hold method. Their method provides the opportunity to characterize the evolution of the charge transport mechanism in the single-molecule break junction process through electronic noise [72]. Instead of stopping the elongation process to perform the noise analysis, they slow the opening process and study the noise of small intervals along the conductance trace. To study the temporal evolution of a molecular junction, they slide a short-time window

Chapter 2. Literature Review

along the conductance trace and calculate the noise power in the window. They repeat this process for all measured traces, and for each window they determine the scaling exponent so they obtain a continuous curve of the scaling exponent. The scaling exponent curves along with the 2D conductance–displacement histograms for 3 different molecules are displayed in Figure 2.15.

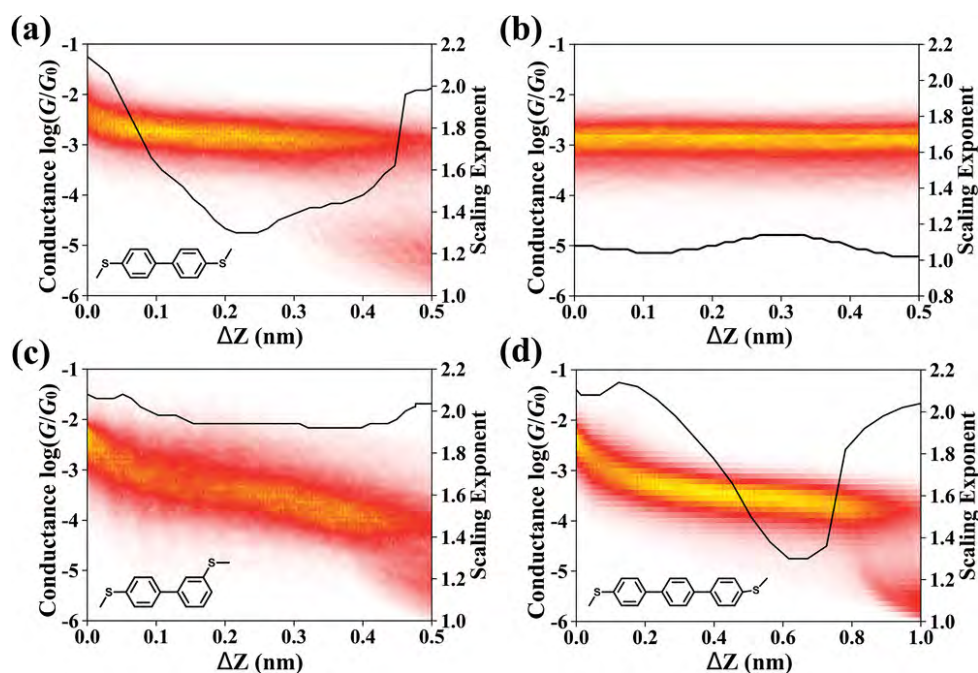


Figure 2.15: Scaling exponent curves as a function of displacement The structure of the molecules is displayed in the insets. (a) and (b) are extracted from the dynamic break junction and static hold measurements for the same molecule, respectively. Source: [72]

Figures 2.15(a), 2.15(c) and 2.15(d) show the exponent curves for three distinct molecules, with their structures depicted in the figures, in conjunction with the two-dimensional conductance–displacement histograms. Their findings reveal that the exponent curves exhibit a *U shape*. For molecule *a*, an analysis was performed where the results were compared to an exponent curve derived from a collection of traces extracted from a static hold measurement, ensuring the analyzed portions matched the length of those in dynamic measurements. As anticipated, the static measurements yield scaling exponent values near 1, indicative of through-bond coupling between the molecule and the electrodes. The exponent curves for molecules *a* and *b* exhibit similarities: initially, the scaling exponent approximates 2, followed by a decrease to approximately 1, and upon contact rupture, the scaling exponent increases back to 2. The authors propose that this pattern suggests the electrode–molecule coupling strength is initially weak when the junction is newly formed but intensifies subsequently.

Flicker noise analysis has proven to be a great tool in the study of electrode–molecule coupling. In this section, two measurement methods from the literature that study the

noise power scaling of molecular and tunnel contacts were introduced. Mechanical stability is crucial in both methods. The first method used hold measurements, where the junction elongation process is stopped for the time of the noise measurement. These static measurements were used to distinguish between the coupling interactions in monomer and dimer junctions. However, these measurements lack reliability because the elongation process is stopped after the STM tip has moved a fixed distance. A more reliable method would be if the tip movement stopped when a trigger conductance that indicates the presence of the molecule was reached. In section 3.4, I introduce a measurement control system with real-time control capabilities that allows such measurements. The second method utilized dynamic break junction measurements to study the temporal evolution of the electrode–molecule interaction during the elongation process. I implemented such an analysis for my measurements and used a sophisticated trace selection technique to develop a better understanding of electrode–molecule interactions in gold–4,4′-bipyridine–gold contacts.

Chapter 3

Measurement Technique and Analysis Software Development

As mentioned in chapter 2, there are several methods to study molecular junctions. In our laboratory, both STM-BJ and MCBJ setups are available. For the analysis of binary conductance switching detailed in chapter 4, I made measurements with our cryogenic MCBJ setup which is vacuum-sealable and was developed to fit inside a liquid helium dewar, so that we can make measurements at temperatures as low as 4.2 K. Later, I also took measurements at room temperature. There is a separate sample holder dedicated for room-temperature measurements, and I used both this sample holder and the low-temperature sample holder without cooling down for measurements at room temperature. For some measurements, I used the STM-based setup too, and although these results are outside the scope of this dissertation, some results used as comparison were derived from data recorded using this setup.

In the following sections, I first summarize some general considerations regarding the measurement technology and measurement control, then describe both the room-temperature and the cryogenic MCBJ setups and also the sample preparations in detail, followed by a description of the room-temperature STM-BJ setup. Then I explain how the FPGA-based measurement control system developed by András Magyarkuti [41] changed the way we make measurements. Finally, I collect the data analysis software developments motivated by the evolution of the measurement control and the amount of additional data.

3.1 Measurement control and measurement technological considerations

Although having very different working principles, both MCBJ and STM-BJ measurement setups can be managed by the same measurement control setup. The outline of the measurement control setup is shown in Figure 3.1. A data acquisition device (DAQ) is connected to the computer that runs the measurement control program. Coarse move-

Chapter 3. Measurement Technique and Analysis Software Development

ments are performed by step motors driven by the digital output of the DAQ. The analog output sets the voltage applied to the piezo actuator to fine-tune the movement, and this is the output that sets the bias voltage to the sample. There is an optional resistor in series with the sample (see the measurement technological considerations in the following paragraph), and the current is recorded through the analog input after being amplified by a current to voltage converter because nanowires typically have low conductance.

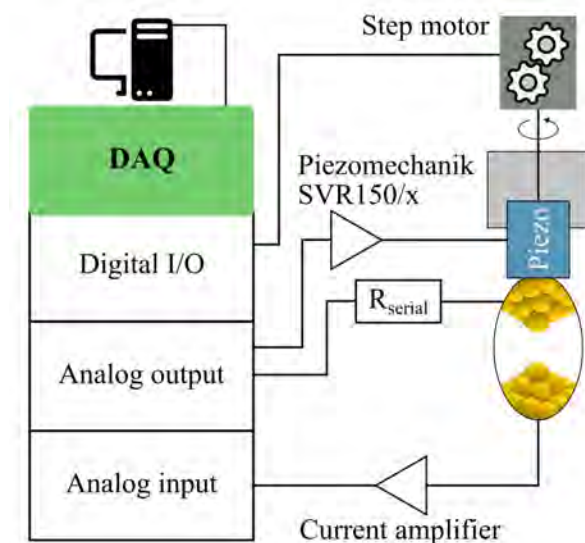


Figure 3.1: Components of the measurement control system. *The DAQ device controls the measurement, and the user interacts with the system through the computer.*

The conductance range of metallic junctions lies in the range of $(1 - 100) G_0$, while this range for organic molecules is much lower: $(10^{-5} - 10^{-2}) G_0$. Let us say that we want to cover the $(10^{-5} - 10) G_0$ conductance range in our measurement – which is typical for our measurements. With an applied bias of 100 mV, the current ranges from 10 pA to 10 μ A. Using a simple linear current to voltage converter (see the simplified circuit diagram in Figure 3.2(a)) to amplify the current, we can cover the metallic range well, but the noise level would be too high to measure the molecular range. To cover such a large range with the same setup, special devices or circuit considerations are necessary.

One solution is to use a logarithmic current to voltage converter which has nonlinear characteristics because it utilizes two diodes as the feedback element. The one I used was developed by Gábor Mészáros, the circuit diagram of the device is shown in Figure 3.2(b) [76]. It can amplify the smaller currents in the molecular range and does not overload even for the higher currents of the metallic range. I used this type of current to voltage converter in my low-temperature current–voltage characteristics measurements for the study of the switching mechanism of 4,4'-bipyridine (see chapter 4). However, this type of complex circuit requires careful calibration and because of the diodes used, it has a relatively high time constant, making the response time slower. This amplifier is not

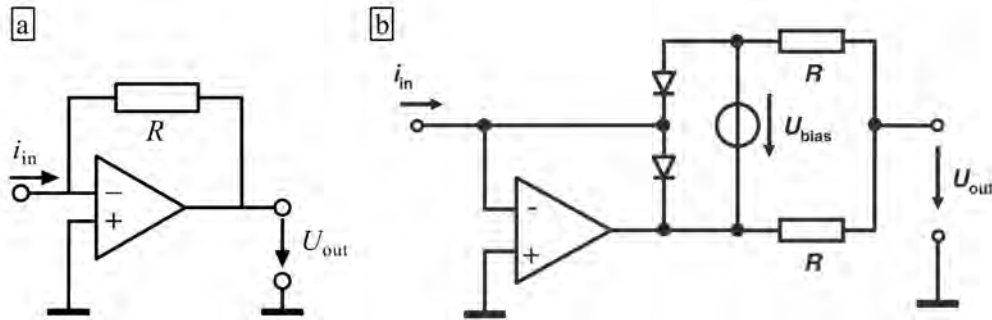


Figure 3.2: Simplified circuit diagrams of the current to voltage converters used in our measurements. (a) *Linear current to voltage converter, where the gain is determined by the value of the feedback resistance (R)* (b) *tunable logarithmic current to voltage converter, two diodes are used as the feedback element.* [76]

optimal for noise measurements because its complex nature might introduce instrumental noises. Due to the slower response time and the possible noise contribution, I used a different layout for my further measurements.

Another solution utilizes a linear current to voltage converter, but paired with a resistor with sufficiently large resistance in series with the sample. Incorporating a resistor in series with the junction allows us to measure higher conductance with the same amplifier gain. When the junction has significantly higher resistance than the series resistor, nearly all the bias voltage drops on the junction. Thus, the measured current corresponds to the junction conductance similar to when there is no series resistor. Conversely, if the junction's resistance is similar to the series resistance, the voltage drop on the junction decreases. Consequently, the same current indicates a higher junction conductance compared to when there is no series resistor. In my measurements, I used a 100 kOhm resistor in series with the sample and a FEMTO-DLPCA-200 current amplifier [77].

At this point, there might be several offsets (e.g. from the analog input/output of the DAQ) present in the measurement setup. These can be removed by setting the current and bias offsets in the measurement control program before starting the measurement. First, we set both the bias and current offsets to zero, then follow a 3-step process. In the first step, we determine the bias offset. After checking that the junction is closed, we connect a separate resistor ($R_{\text{calibration}}$) in series with the sample (typically 12900Ω that corresponds to the conductance $1 G_0$). The bias offset shifts the bias value either in the positive or negative direction, so if we change the polarity of the applied bias, we see a difference in the absolute value of the measured current. Now we adjust the bias offset until the absolute value of the measured current is the same when the polarity of the applied bias is changed. In the second step, we determine the exact value of the resistor in series, R_{serial} (if present), using that the junction is closed, so its resistance is much lower than the calibration resistors ($R_{\text{calibration}}$). We set the value of R_{serial} in the measurement control program such that the measured resistance is exactly the value of

$R_{\text{calibration}}$. In the final step, we determine the current offset. We remove the resistor used for the calibration and completely rupture the junction. No current should flow through the junction because of the large electrode separation; therefore, the measured current is equal to the current offset.

In a measurement, one also has to consider other measurement technical considerations, such as signal loss or environmental effects. It is important to limit the distance that a small signal needs to travel before it is amplified or recorded, especially in noise measurements. To protect against environmental noise, the setup is always placed on top of a vibration isolation platform.

3.2 Mechanically controllable break junction setups

In chapter 2, I provided an introduction to the fundamental principles of MCBJ setups. In the following sections, I concentrate on the experimental setups employed in my own measurements, with particular attention to the procedures for sample preparation and details specific to each setup.

3.2.1 Sample preparation

In these measurements, two distinct sample types are utilized, both crafted manually with a high degree of skill and, occasionally, considerable patience. The first type of sample, as depicted in Figure 3.3(b), is constructed from a phosphor bronze sheet Figure 3.3(b) that has been precisely cut to specifications. Initially, a thin lead layer is placed centrally as padding and is subsequently bisected with a sharp blade to create two lead islands intended for epoxy deposition. To enhance the adhesion between the lead islands and the epoxy, the surface of the lead islands is incised in a grid pattern using a blade. Upon these lead islands, epoxy droplets [78] are deposited, within which a high-purity metallic wire is situated—specifically, a gold wire with a purity 99,99% and a diameter 0.1 nm [79]. The wire is submerged in the epoxy so as to leave three sections exposed: the two ends and the central section. The objective is to position the epoxy dots in close proximity without permitting them to touch or fully cover the middle portion of the wire. It is crucial to ensure that the central section of the gold wire remains uncoated with epoxy to prevent potential contamination that might compromise the results. The two ends of the wire extending over the epoxy edges are subsequently utilized to connect the sample to the sample holder. To establish contact with the gold wire, a twisted pair of very thin, insulated copper wire is employed; each end is soldered to the gold wire extremities over the fixation points, with the opposite ends affixed to the PCB within the sample holder. The second type of sample, illustrated in Figure 3.3(a), operates under similar principles but is based on a printed circuit board (PCB) sheet, which is scored at three locations to separate the conducting surface of the PCB into four insulated sections. A thin lead layer is applied to the middle sections, divided by the central score line, and used to solder copper clamp bases onto the surface.

Chapter 3. Measurement Technique and Analysis Software Development

Each copper base contains two drilled holes at either end to permit the attachment of the copper clamp top via small screws. Prior to securing the top clamps, the metallic wire – the same gold wire – is placed upon the copper pads centrally and thereafter compressed with the clamp tops. This sample is termed a mechanically fixed sample. In this configuration, it is unnecessary for the gold wire to extend over the fixation points because both the copper clamps and the PCB are conductive. To the gold wire, a twisted pair of very thin, insulated copper wire is again used, with the soldering conducted on the middle sections of the PCB surface and the counterpart ends soldered to the PCB within the sample holder.

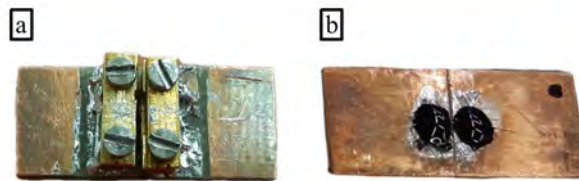


Figure 3.3: Photos of samples with different fastening mechanisms (a) *Sample fastened by copper clamps with their base soldered on top of a PCB board and the top part* (b) *Sample with the gold wire fixed by two epoxy dots to fasten.*

It is important to note that sample preparation does not end here. If we were to place this sample in the sample holder, we would find that we could not break the wire in the available movement range. To make sure that the wire breaks as expected, it needs to be thinned first. The wire is thinned in the middle between the two fix points. To achieve this, we have a special device in which the sample is glued to a vertical surface with a sharp blade in front of it. We place this setup under a microscope, center the blade in front of the gold wire, and approach the blade to the surface of the wire. Once they are in touch, we move the vertical surface holding the sample up and down to make the cut a small notch with a size of approximately 50%-70% of the diameter of the wire. This method is best suited for epoxy samples because the copper clamps are two wide and tall to see the wire from the side. So for the mechanically fixed samples, we usually make the cut by hand: we place the sample under a microscope and make a determined cut with the sharp blade by hand. Achieving the notch with a singular cut is optimal, as it not only ensures that the wire breaks during the measurement but also determines the point of rupture.

It is noteworthy that before beginning sample preparation, each building block underwent a cleaning process using acetone and isopropyl alcohol to eliminate contaminants, followed by rinsing with distilled water to remove any residual substances, and dried using nitrogen gas.

Both types of sample have advantages and disadvantages that we need to consider when measuring. The mechanically fixed sample is great for quick sample preparation, as the screws are easy to remove or reattach. However, the stability greatly depends on the

height of the bottom copper pads, because the higher the pads, the higher the wire lies above the bending beam, resulting in a lower transmission coefficient between the vertical movement of the piezo and the horizontal elongation of the wire. The first samples had quite high copper pads that affected the results. Later, the lab technicians made a new set of copper pads, where the bottom part is hollowed out in the middle and the top part is T-shaped, which improved stability by placing the gold wire closer to the PCB sheet surface. I used this mechanically fixed sample configuration in my measurements. Later, a hemisphere shape was etched into the middle part of the top clamps for easier molecule dosage. The preparation of epoxy samples is more time-consuming and requires more experience, but if we pay attention, we can create samples where the distance between the dots is very small, making the loose electrodes in the middle shorter and thus more stable. The downside of epoxy samples is that they seem to be more susceptible to contamination. In certain instances, unexpected peaks were detected in the histograms prior to the introduction of the molecule to the contact. These anomalies can be attributed to contaminants present within the epoxy components. Nevertheless, this contamination was not universally observed across all epoxy samples, indicating that meticulous preparation can effectively mitigate this issue.

3.2.2 Low-temperature and room-temperature MCBJ setups

The MCBJ setups in our laboratory have the same building blocks but are placed in a different frame depending on the purpose of the measurement. Both frames contain a step motor for coarse movement, a piezo actuator and a sample chamber, with the necessary connections to control them and to record the data.

The low-temperature sample holder has a long pipe-like structure to fit inside the liquid helium dewar. The bottom (low-temperature) part shown in Figure 3.4 consists of the sample chamber, which houses the sample, the piezo actuator, and a differential screw that connects to the step motor located at the top of the sample holder. This bottom part is inserted into the liquid helium dewar and slowly lowered until it is fully immersed in liquid helium for low-temperature measurements. The top (room-temperature) part sticks out from the liquid helium dewar, this is where the data acquisition device connects to control the movement of the step motor and piezo actuator, and where the bias is applied and the current is measured (see Figure 3.5(a)).

The room-temperature sample holder (see Figure 3.5(b)) is a compact version of this, it has the same connections but instead of being inserted into the dewar, a frame with three legs keeps it in place.

The sample chambers of each setup have two slits in the inner wall where the bending beam of the sample slides in. The sample side usually points down (except for the molecule dosage in liquid form, see next section) and the bottom part of the bending beam touches the pushing rod of the piezo actuator. In Figure 3.4 the bending beam is further supported by a spring on the sample side, but this configuration is not compatible with in-situ evaporation of molecules (see the next section), so in my measurements the spring was

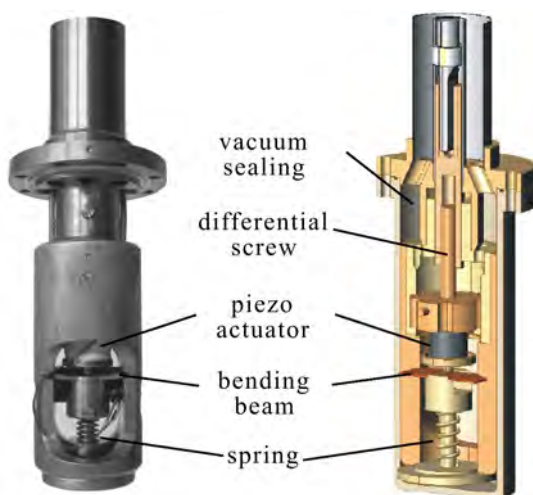


Figure 3.4: Black and white photo and cutaway diagram of the sample chamber of the low-temperature MCBJ sample holder. *The bending beam of the sample slides into the two slits engraved in the sides of the sample chamber, the piezo actuator is above the sample and the bending beam is supported by a spring from below, to increase stability.*

removed. The two ends of the twisted pair on the sample are soldered on the PCB sheet built inside the sample chamber. Each sample holder is vacuum-sealable, which is essential for cryogenic measurements but optional for room-temperature measurements.

3.2.3 Molecule dosage techniques

In situ molecule dosage techniques are the most commonly used methods to introduce molecules to the system. Using these methods, the molecule can be added at any point during the measurement, enabling clean measurements prior to the molecule dosage. These clean measurements can be used to test the purity of the system, to verify that the molecule is incorporated between the electrodes once it is added.

In situ evaporation of molecules in MCBJ setups

The sample is placed in the sample holder as previously described. A small quartz tube is filled with the target molecule and placed inside the tungsten filament of a small light bulb, which is then placed below the sample as shown in Figure 3.6(a). Then the sample chamber is closed, optionally vacuum sealed, and if we want cryogenic measurements, cooled down. When we want to add the molecule to the system, we stop the measurement and break the wire completely. Then the light bulb is switched on and the heat of the tungsten wire melts and evaporates the molecule crystals, which are then deposited on the sample wire. After a few closing–opening cycles are repeated, the molecules deposited on top of the wire can incorporate between the two metal electrodes, forming the molecular contact of interest.



Figure 3.5: Sample holders during measurements. (a) Low-temperature measurement setup. *The room-temperature part of the sample-holder has all the connection outlets. During measurements, proper grounding is important, otherwise the noise level would be high.* **(b) Room-temperature measurement setup during a measurement.** *This setup is more compact, but has the same connection outlets. The setup is placed on a vibration isolation platform.*

In the low-temperature measurements, the evaporation of the molecule on top of the metallic surface can take significantly longer, and we must wait until the close environment cools back down before continuing the measurement; otherwise, strong drifting can be observed as a result of the decreasing local temperature.

Adding molecules in solution using a liquid cell

The dosage of the molecules in liquid solution can be a bit tricky in MCBJ setups. As seen previously, in most cases, the sample is upside down in the sample holder. This is not suitable for dosage with solution. Therefore, the room-temperature sample holder is turned upside down in the three-legged frame. In this way, we can drop the solution onto the sample surface. However, this is still not very effective because there is nothing stopping the solution from flowing off the sample, especially when it is bent. To prevent the solution from flowing off the sample, a liquid cell can be used. The liquid cell is a ceramic frame that sits around the sample and contains the solution during the measurements. This is not suitable for use with the mechanically fixed MCBJ sample, and even the epoxy sample needs some modifications. No lead padding is used under the epoxy



Figure 3.6: Photomontage of the measurement setup illustrating molecule dosage techniques. (a) In situ evaporation of molecules. *The sample is placed into the sample holder, as seen on the right. A small quartz tube is filled with the target molecule and placed inside the tungsten filament of a small light bulb, which is then placed below the sample for evaporation.* [40] **(b) Molecule dosage in solution using a liquid cell.** [40]

dots, and the dots need to be as small as possible to fit inside the liquid cell. The two overhangs need to be longer in order to guide them above the liquid cell to contact it with the sample holder. As depicted in Figure 3.6(b), the wire is threaded through the o-ring, then the o-ring is placed around the epoxy dots. The liquid cell is placed on top and fixed from above with three springs to keep it in place. The solution is dosed from above and is contained by the liquid cell.

To mix the solution, we first specify the desired concentration, which is around 1 – 4 mM. It is best practice not to store the mixed solution, so we mix very low amounts. We mainly use mesitylene (1,3,5-trimethylbenzene) as the solvent.

3.3 Room-temperature scanning tunneling microscope-based break junction setup

The room-temperature STM-BJ setup uses the same frame as the room-temperature MCBJ setup shown in Figure 3.5(b), the main difference being that it is turned upside down and we have an STM inside the sample holding chamber. It is important to note that the directions of movement need to be reversed compared to the MCBJ setup. The

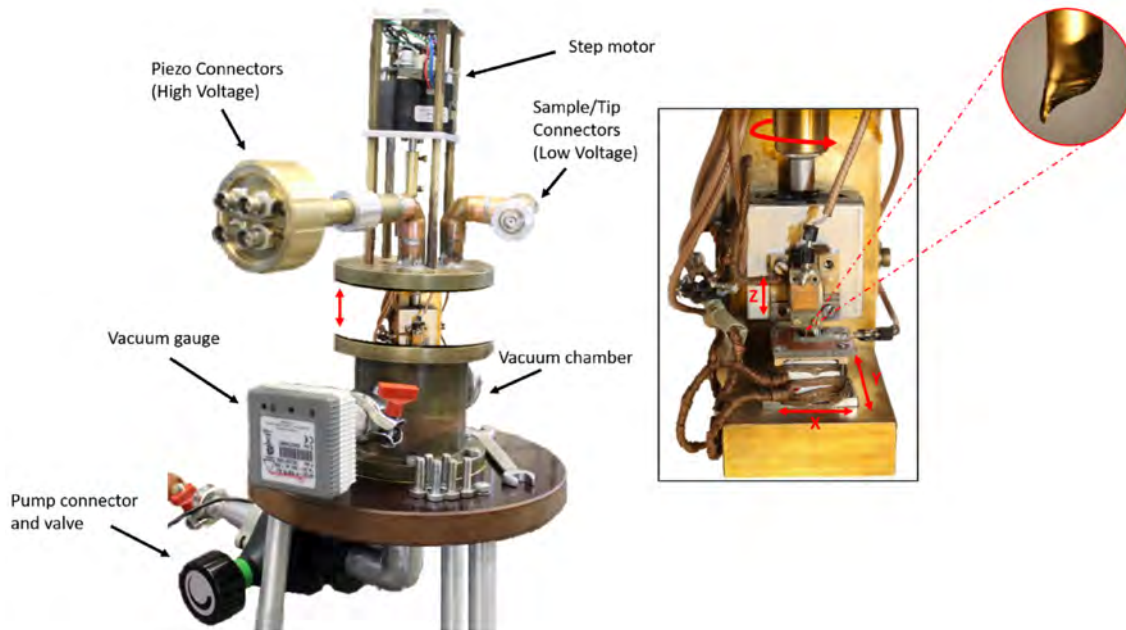


Figure 3.7: Room temperature STM-BJ setup reproduced from [41]

same movement that is used to elongate the wire in the MCBJ setup to break the wire now pushes the STM tip into the gold-plated surface.

3.4 FPGA-based measurement control

The MCBJ method ensures great control over the sample thanks to the high reduction ratio between the movement of the piezo actuator and the elongation of the metallic wire. However, reliably stopping the opening/closing process in a given configuration requires even more control over the measurement. As mentioned in chapter 2, there are several attempts to measure on a junction by stopping the opening/closing process when a selected molecular configuration is formed; however, these are all affected by the stochastic nature of the opening/closing process. András Magyarkuti developed a measurement control system based on a Field-Programmable Gate Array (FPGA) [41], which is an integrated circuit that can be reconfigured to meet specific use case requirements after the manufacturing process. Because the process is controlled on the hardware level, it enables shorter reaction times compared to software-controlled measurements. Rapid detection of events makes it possible to stop at a predefined conductance value, capturing the junction when a trigger conductance is reached. The structure of the measurement control system is shown in Figure 3.8(a). The program controlling the measurement runs on the FPGA, and this manages the cards that control the step motor (NI 9403) and the piezo actuator controlled by the voltage Piezomechanik SVR150/x [80] through the analog

output NI 9263, while recording the current flowing through the junction amplified by a FEMTO-DLPCA-200 current amplifier [77] with a 24-bit resolution acquisition board with an anti-aliasing filter (NI-9239).

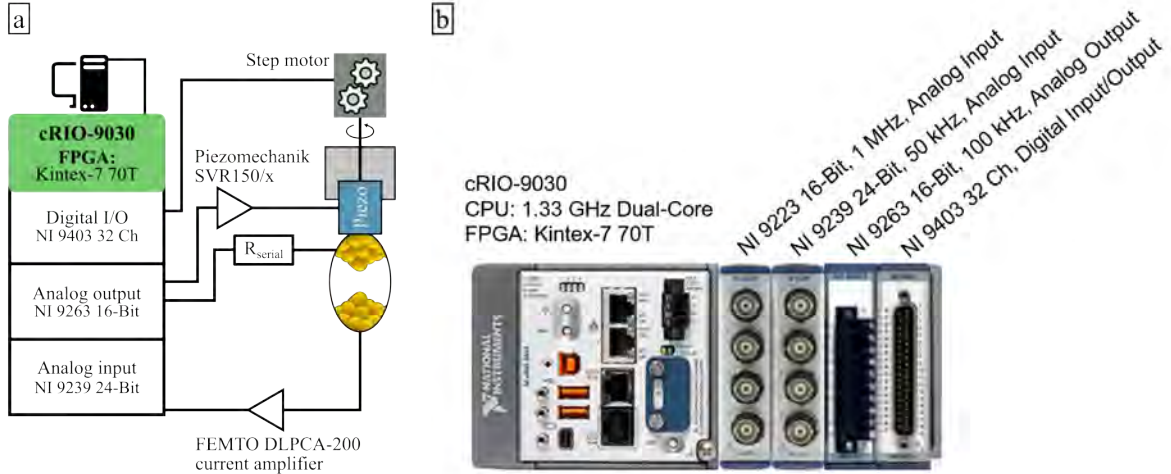


Figure 3.8: Measurement control setup (a) *Schematic structure of measurement control setup.* (b) *Photo of the measurement controls* [41]

The flow chart of a simple measurement is shown in Figure 3.9(a). The colors of the individual processes correspond to the different colored parts in the example plots in Figure 3.9(b). In the beginning of the measurement, we start with a metallic contact with a junction conductance $> 10 G_0$. In the *opening process*, the voltage applied to the piezo actuator is increased to elongate the gold wire until a certain trigger conductance ($10^{-2} G_0$) is reached. Then, the voltage on the piezo actuator is kept constant and the *hold period* begins, where a predefined bias signal is applied: a 3 s long constant 100 mV signal in this example. Once this signal is over, the opening process is continued: the piezo voltage increases until the conductance decreases below $10^{-5} G_0$. After the opening process is over, the *closing process* begins: the piezo voltage change is reversed, closing the junction, until the closing trigger conductance is reached ($10^{-4} G_0$). The second *hold period* begins and the bias signal is applied again while the piezo voltage is kept constant until the signal ends. Finally, the junction is closed, so that the conductance reaches $> 10 G_0$, by decreasing the piezo voltage. By closing the junction, the cycle can start again and the process of opening–hold–opening–closing–hold–closing process can be repeated thousands of times. The opening/closing portions are called *pull/push traces*, while the hold portions *pull/push hold traces*, referring to the process stopped to apply the bias signal. The data is stored in binary files; the pull/push traces and the corresponding hold traces are stored separately. Apart from directly measured data, there is a lot of metadata to store that is important in the analysis.

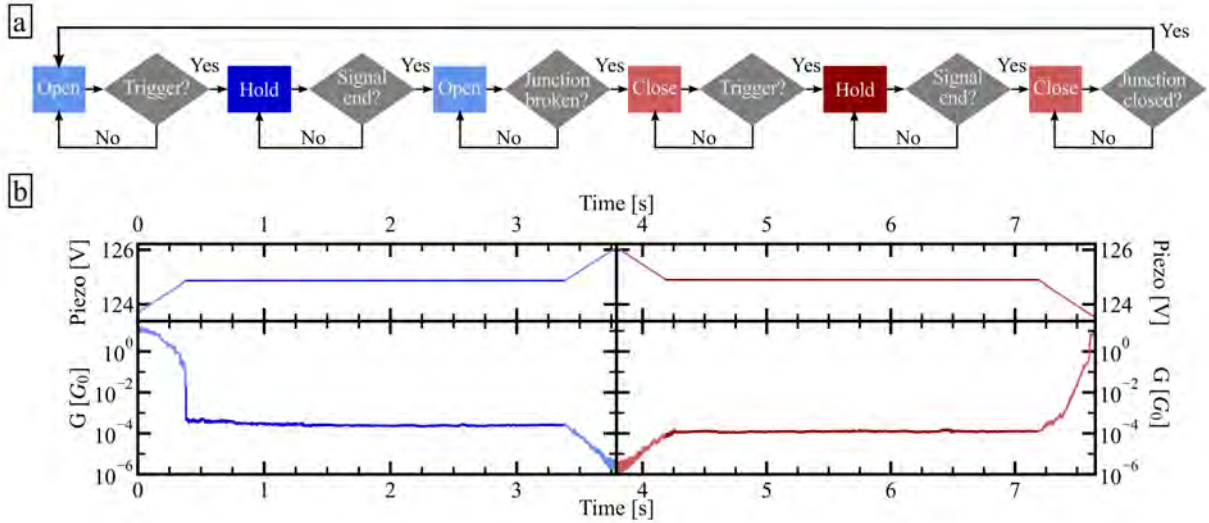


Figure 3.9: Measurement flow. (a) **Flowchart of a typical measurement.** The number of steps in this flowchart symbolize the increase in complexity compared to a simple BJ measurement. (b) **Example measurement with a 3 s long hold portion.** The colors correspond to the color of the rectangular process boxes in (a). When the voltage applied to the piezo is constant, the junction is held steady, and a constant bias signal is applied while the current is measured. However, as I will show in later chapters, this bias signal can be arbitrarily defined.

The measurements in enhancing our understanding of the conduction properties of single-molecule nanowires; however, they also introduce new challenges. The length of a typical BJ conductance trace is 1 – 2 seconds, i.e. $\sim 50000 - 100000$ points with a sampling rate of 50000. However, the length of the hold portion depends on the length of the applied bias signal, which can become long, especially at low temperatures, where the contact is more stable. Typically, the length of the hold portion is 3 – 60 times longer than the simple BJ measurement, leading to a lot more data points taking up memory on the computer. This aspect needs to be taken into account in the data analysis.

3.5 Data analysis software developments

Initially created by András Magyarkuti, the legacy data analysis software was implemented using Igor Pro. Yet, as our team advanced towards machine learning algorithms for data sorting, the limitations of the Igor Pro framework became apparent, leading to the development of essential extensions in Python by Nóra Tenk and András Magyarkuti.

In my analysis, Igor Pro served well initially, but managing vast data volumes (of

the hold measurements) presented challenges due to its interactive programming style, with the analysis code designed to load 100 traces at once. It was necessary to change the data analysis software, and we had to decide whether to update the old codes or rewrite the whole in a different language. Nóra and András opted for Python to develop machine learning algorithms for the PC analysis of molecular junctions, primarily due to its widespread use in machine learning and data science. Python is widely used in research, even in molecular electronics, which makes collaboration with other groups easier, as IgorPro is not that well known. Python also has useful and well-documented packages and is easily integrated with GitHub for version control and collaboration. My goal was to rewrite the legacy codes in Python to better handle these large amounts of data and to unify the analysis software. In this process, I changed the data storage to make it more accessible and rewrote the previously existing data processing pipelines in Python. Following the optimization of the data structure, the data analysis workflow needed to be adjusted accordingly. I remodeled the data analysis software in Python, developing the essential tools (like trace loading, 1D and 2D histogram calculations, correlation matrix calculation, etc.) based on the existing IgorPro codebase and adding advanced analysis procedures necessary for the complex analysis of the measurement data. In the development of the data analysis code, my objective was a well-documented easy-to-understand code to aid student training, improve code reusability, and make collaboration easier, as this was a shortcoming of previous analysis code, making training and collaboration more work-intensive tasks. The noise processing codes were exclusively written in Python by implementing the basic noise analysis codes written in Igor Pro by Zoltán Balogh and supplementing them with advanced analysis methods.

3.5.1 Optimized data architecture for high-performance evaluation

The straightforward method to store data is a simple ASCII file, which is easy to access. However, it is not suitable for storing large amounts of data because it would take up a lot of space, which is not cost-efficient. To address this problem, data storage was changed to binary files, each file containing 100 pull/push traces separately, divided by the number -133. Each trace was stored with its corresponding metadata, but the metadata was simply stored in the same array as the trace data, and for hold measurements, the voltage and current values were stored in the same array. This storage system was very efficient but hard to understand without a *key* to identify metadata, which was hidden deep in the measurement code. In addition, there was a finite number of spaces reserved for the metadata, limiting the number of values to be saved. Exceeding this limit would mean that, for any future metadata, the file structure would have to be expanded. So, the first goal of the redesign process was to optimize data storage, preserving storage efficiency but making data access easier, by saving data in `hdf5` format.

An HDF5 file is a container for two kinds of objects: datasets, which are array-like collections of data, and groups, which are folder-like containers that hold datasets and

other groups. [81] HDF5 files maintain the efficiency of storing data but have a hierarchical structure. In this way, the metadata and the measurement data can be stored grouped together for each individual trace and easily accessed by their name.

The traces are stored in 100 trace blocks (except for the first block, which contains only 99 traces). For each trace, the pull and push conductances are grouped together, and for each conductance, metadata are stored as attributes. The resulting data structure is shown in Figure 3.10. Naming the metadata and structured storage made collaboration easier because the data is accessible even in the absence of a key. All necessary functions and the data structure are available in a GitHub¹ repository which makes them easily accessible.

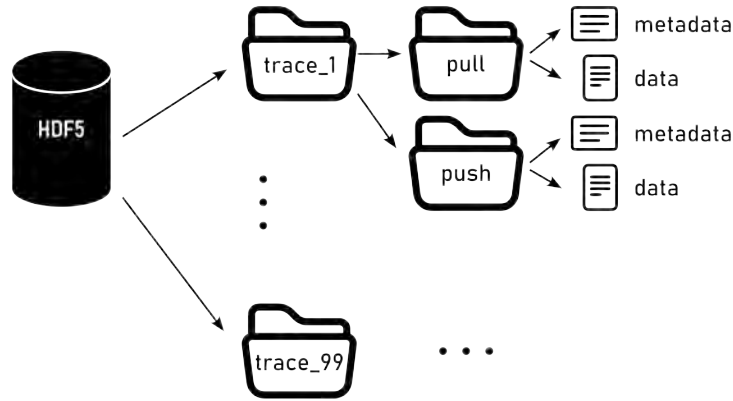


Figure 3.10: File structure Both the simple BJ data and the hold data are stored in `hdf5` file formats. The metadata and the measurement data are stored together in a hierarchical structure, and can be reached using text keys.

3.5.2 Data analysis developments for hold measurements

The biggest part of the development was handling the hold current and bias voltage data. In the hold measurements, any arbitrary bias signal can be applied, and the post-processing can become complex based on this signal. The analysis of a hold trace is demonstrated in Figure 3.11.

In the simplest case, the bias voltage is constant, but it is more interesting to study the voltage dependence e.g. with a step-like bias signal or a triangle signal for studying the current voltage (see the details in chapter 6). I developed the necessary functions to cut the measured data into smaller chunks and separately analyze them. By separating the bias steps, we can calculate the relative conductance noise for each bias plateau and study its voltage dependence. The bias plateau edges are determined by calculating the derivative of the bias signal and finding the peaks that correspond to significant voltage

¹https://github.com/gretemezei/mcbj_stmbj

changes. Two neighboring peaks enclose the current data for a plateau, so noise analysis is carried out for each enclosed region.

When the bias steps are combined with the measurement of current–voltage characteristics as shown in Figure 3.11(a), the separation becomes more difficult because the $I(V)$ portion is between two edge points (these points are denoted by black dashed lines), but it is not a bias step, so it must be handled differently. The bias plateau edges are denoted by black dashed lines. By entering the number of the plateau that is followed by the $I(V)$ portion (the first in this case), the software knows that the region enclosed by the next edge positions is the $I(V)$ curve.

After finding the individual bias steps, the current of each step is analyzed: first, the power spectral density is calculated, then the relative current noise is determined. To calculate the power spectral density, we perform the Fourier transformation as in Equation 2.9. As discussed in section 2.6, the measured signal is divided into segments and the number of segments for evaluation is defined by the parameter `num_fft` and each segment consists of a power of two number of points. In Figures 3.11(b) to 3.11(d) I show the evaluation of the three bias steps from Figure 3.11(a). Two examples are shown for the `num_fft` parameter. In the first case, `num_fft = 1`, the program determines the largest power of two that fits in the plateau and performs the FFT for this range; the edges of the interval are denoted with dark blue dashed lines. In the second case, `num_fft = 5`, the intervals for which the FFT is calculated are divided by the yellow dashed lines. In both cases, we discard the beginning and the end of a plateau, but this is desired: the sudden voltage change at the transition between two plateaus can lead to instabilities we want to avoid.

Then, the power spectral densities are calculated for the three plateaus with both `num_fft` parameters. The PSDs for the three plateaus are shown in Figures 3.11(e) to 3.11(g), respectively. The mean squared deviation of the current ($\langle \Delta I^2 \rangle$) is given by the integral of the spectral density over the whole frequency range, as in Equation 2.6. Experimentally, it is calculated for a finite frequency range, because of the frequency resolution and the limitation imposed by the Nyquist theorem. We further limit the range, depending on the measurement, as depicted with the yellow background in Figures 3.11(e) to 3.11(g). The detailed statistical analysis of traces like these is discussed in chapter 6.

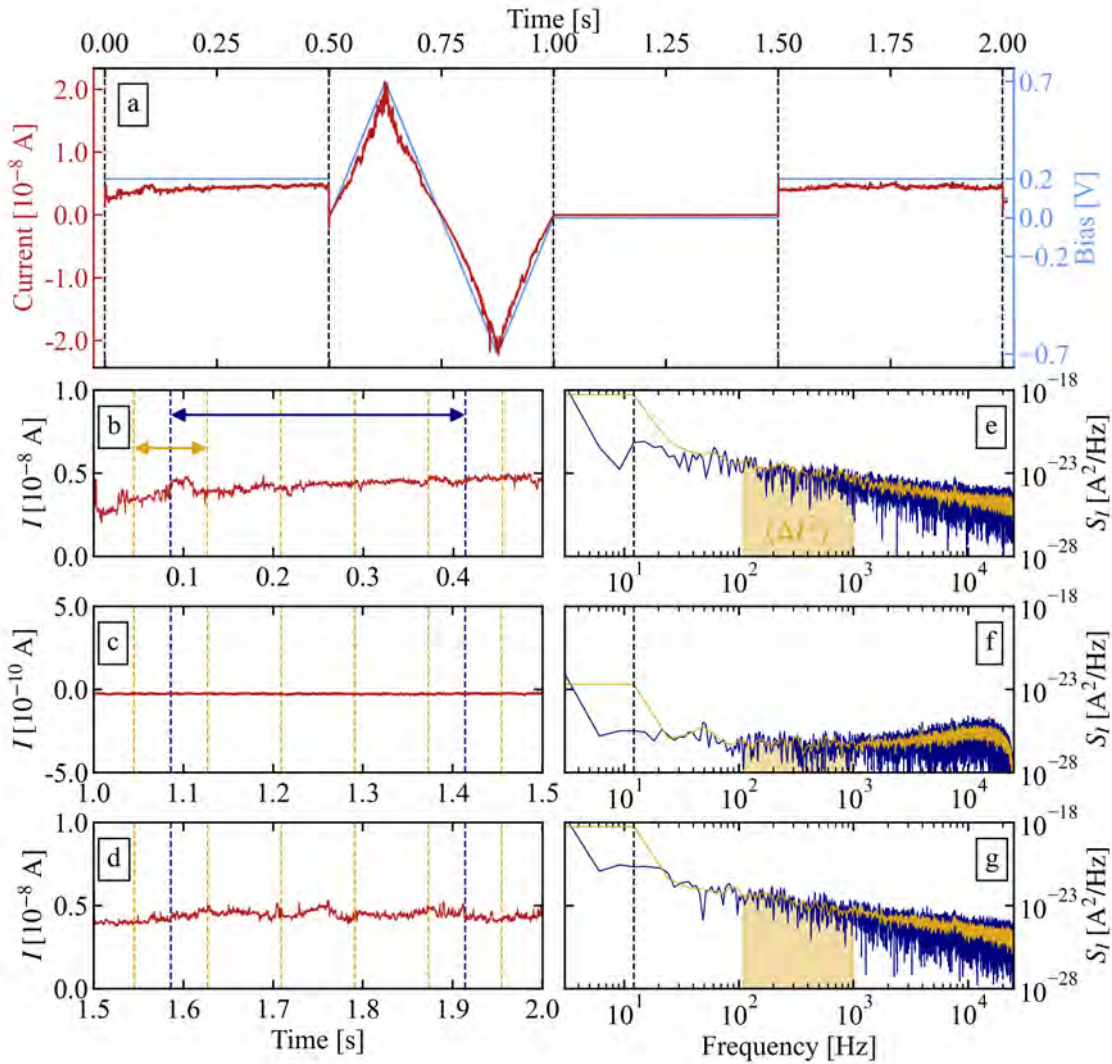


Figure 3.11: Demonstration of power spectral density calculation for a hold trace with a complex bias signal (a) Bias signal and measured current as a function of time for a hold trace recorded in the closing process. The signal consists of a 200 mV step, an $I(V)$ signal with a maximum bias of 700 mV followed by a 0 mV and a second 200 mV bias step. The bias step edges are determined from the peaks in the derivative. The individual bias plateaus are then analyzed separately. (b)-(d) The measured current for each bias plateau in order. The intervals for the FFT calculation are determined based on the `num_fft` parameter. Dark blue dashed lines show the interval boundaries for the `num_fft = 1` case, and yellow dashed lines for the `num_fft = 5` case. A single interval is denoted with a double pointed arrow with the corresponding color. (e)-(g) Power spectral densities calculated for the individual bias plateaus. The PSDs are calculated for the current in (b)-(d), respectively. The colors correspond to the regions enclosed by the same colored dashed lines in subfigures (b)-(d).

Chapter 4

Binary Conductance Switching in Au–BPY–Au Single-molecule Nanowires

As introduced in chapter 2, there are molecular systems that show switching with different external stimuli, which is a promising application possibility. Therefore, molecules that have two or even three distinct conductances depending on some tunable parameter are of utmost interest. Such a molecule is the 4,4'-bipyridine, introduced in chapter 2, which has two different binding geometries with two distinct conductances, depending on the distance between the enclosing gold electrodes. By changing the electrode distance with a small sinusoidal modulation to the piezo actuator, Quek et al. were able to mechanically switch between these two configurations in their room-temperature STM-BJ setup [54].

Their measurements rely on the assumption that molecular contacts are formed after a fixed electrode displacement, so they stop the opening process after the STM tip has moved a certain distance, then apply a short (~ 60 ms) periodic signal to the piezo actuator to mechanically perturb the junction, repeatedly compressing and stretching it with an amplitude of 2 \AA . Then, they filter the traces that actually exhibit molecular features indicating that a molecule was indeed caught in the junction during the period of mechanical perturbation. The selected traces showed a periodic change in conductance indicating periodic switching between the two binding configurations, for example traces from their article, see Figure 4.1 [54].

This form of measurement is inefficient because it is highly dependent on the likelihood of a molecule being positioned between the electrodes at a specific pull distance. In order to acquire a statistically significant dataset, a considerable number of individual traces must be measured. Therefore, my goal was to investigate the switching behavior of the BPY molecule using our cryogenic measurement system, where conditions are substantially more controlled than in room-temperature measurements. I carried out measurements at $T = 4.2 \text{ K}$ temperature with the mechanically controllable break junction setup (see chapter 3) and thanks to the exceptional stability at low temperatures, I was

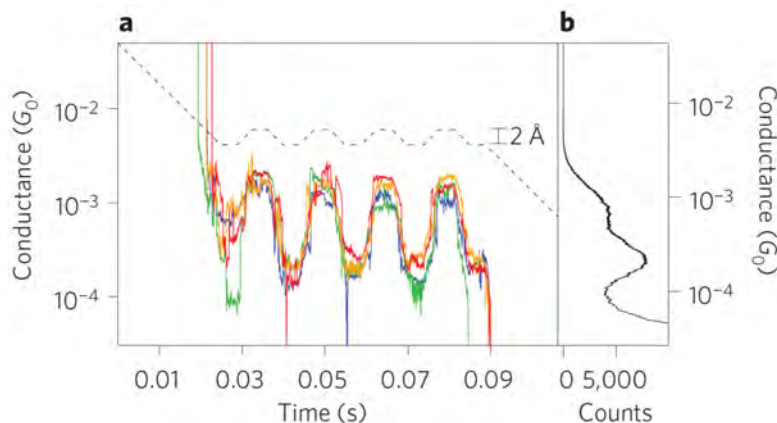


Figure 4.1: Periodic switching between the two stable configurations of Au–BPY–Au junctions The conductance (colored lines, each color corresponds to individual opening measurements) changes periodically with the perturbation signal (dashed curve) with an amplitude of 2 \AA applied to the piezo actuator. The conductance histogram is shown on the right for comparison. Source: [54]

able to map the response of the junction to the manipulation of external parameters, such as the electrode distance and the applied bias, in detail.

In this chapter, I show that – similar to room-temperature measurements – switching of the BPY molecule can be achieved at low temperatures by mechanical actuation (adjusting the electrode separation), and that, in addition to mechanical switching, stochastic switching between the same conductance states can be achieved by applied voltage. I will also show how the parameters of the probabilistic switching are tunable with voltage and electrode separation. Finally, I compare the results of my measurements with different model considerations [P1].

4.1 Conductance of Au–BPY–Au molecular junctions in low-temperature measurements

Using high-purity gold wires, I performed measurements with the sample preparation method and setup introduced in chapter 3. After the setup is cooled in liquid helium, the first step is to test the purity of the system. I recorded a few thousand BJ traces before introducing the molecule into the system and created the 1D conductance histogram. I verified that the histogram showed the characteristic traits of a clean 1D conductance histogram: a sharp peak at $1 G_0$ conductance corresponding to the single-atomic wire; and a consistent, peak-free tunneling region at conductances below $1 G_0$, as shown in Figure 2.9(c). In these measurements, verifying the purity of the system is crucial because then we can be certain that we are studying the configurations of the target molecule and not some contamination that was introduced with the sample.

Chapter 4. Binary Conductance Switching in Au–BPY–Au Single-molecule Nanowires

This was followed by the in-situ evaporation of BPY, and the presence/appearance of the target molecule was investigated by 1D conductance histograms. A representative example of opening-closing (blue/red) conductance trace pair is displayed in Figure 4.2(a), while the opening and closing 1D histograms (blue and red, respectively) created from thousands of these low-temperature traces are shown in Figure 4.2(b) with the reference opening 1D histogram acquired with the same setup at room temperature (light-blue area graph). Utilizing the atomic chain pulling mechanism of gold mentioned above, the voltage applied to the piezo actuator is converted into displacement units using the distance between two adjacent peaks in the plateau length histogram of the $1 G_0$ plateaus of the measurement, as this type of calibration is common practice in the literature [13, 14, 82].

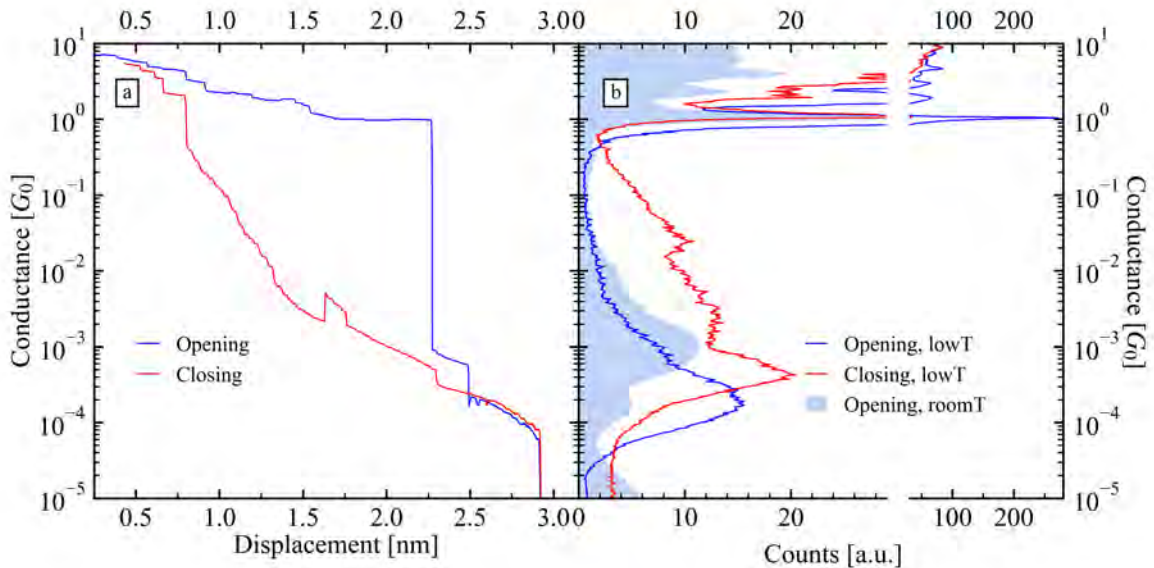


Figure 4.2: Molecular traces and histograms. (a) *Example opening-closing trace-pair showing molecular features and (b) the corresponding 1D histograms generated from 3800 traces measured at low temperature. For comparison, I also plotted the 1D histogram of previous room-temperature molecular measurements [43] as light blue area graph (constructed from 15200 traces).*

If we compare the histograms with those in the literature, we find that the room-temperature conductance histogram nicely reproduces the common double-peak structure of BPY showing a pronounced peak at $G \approx 10^{-3} G_0$ and a smaller peak at $G \approx 3 \cdot 10^{-4} G_0$ [54, 83, 84]. These two peaks (corresponding to different binding geometries) are commonly referred to as HighG and LowG configurations. Based on the literature [54], in the HighG configuration, the molecule couples to the side of the gold electrodes due to the small gap size, while at larger gap size the molecule slides to the apex of the electrodes,

Chapter 4. Binary Conductance Switching in Au–BPY–Au Single-molecule Nanowires

resulting in the decreased LowG conductance, as mentioned in chapter 2. In contrast, the low-temperature opening histogram (blue) shows one peak in the LowG region, but a closer look reveals a small shoulder in the HighG range in addition to the pronounced peak [46, O1]. This phenomenon was attributed to the low-temperature *single-atomic-chain-pulling* mechanism [46], which is typical for gold. While breaking a macroscopic gold contact at low temperature, the single-atomic contact formed can become very long, consisting of two or more gold atoms that form a chain [13, 14, 82]. This phenomenon is not as common at room temperature because the high surface diffusion suppresses the formation of long atomic chains. When the single atomic chain formed in the opening process ruptures, the constituting atoms snap back to the surface of the electrodes, so the resulting gap is so wide that it cannot accommodate the HighG molecular configuration anymore.

Comparing the low-temperature opening and closing histograms (blue and red curves in Figure 4.2(b), respectively), we can make the following observations: the peak positions in the closing histogram are shifted toward higher conductances, and although the lowG peak remains dominant, the HighG peak looks more pronounced compared to the same peak of the opening histogram. This characteristic can be explained by the adhesion between the molecule and the gold electrodes [85]: during the opening process, a stretched molecular junction forms in the larger gap between the gold electrodes; on the other hand, while closing the junction, both the molecule and the electrodes are relaxed, and no strain acts on the junction, leading to higher conductances. This also explains how the relative dominance of the HighG to LowG conductance peaks changes: the HighG peak becomes more pronounced in the closing histogram because there is no restriction to the formation of the HighG configuration, as we have seen in the opening process, where the restricting factor is the wide gap formed as the gold electrodes rupture [O1].

4.2 Analysis of mechanical switching of Au–BPY–Au molecular junctions

As shown above, the characteristic conductances of the two configurations of the BPY molecule are also observed in the low-temperature measurements, although slightly different from those of the room-temperature measurements. Thus, the question arises whether the mechanical coupling presented by Quek et al. can be performed under cryogenic conditions. My goal was to take advantage of the enhanced mechanical stability provided by the low-temperature measurement environment to reproduce the mechanically controlled switching and to perform long and well-controlled molecular measurements with sub-Ångstrom resolution electrode separation tuning.

Based on the room-temperature measurements of Quek et al., I studied how changing the electrode separation affects the molecular binding configuration at low temperature. In Figures 4.3(a) to 4.3(c), I demonstrate the reproduction of this mechanical switching on a timescale two orders of magnitude longer than in their study, utilizing the enhanced

Chapter 4. Binary Conductance Switching in Au-BPY-Au Single-molecule Nanowires

mechanical stability of the junction in the low-temperature environment. Due to the exceptional stability, we can also resolve the sub-Ångstrom displacement interval where I observed conductance hysteresis along the displacement cycles Figure 4.3(c).

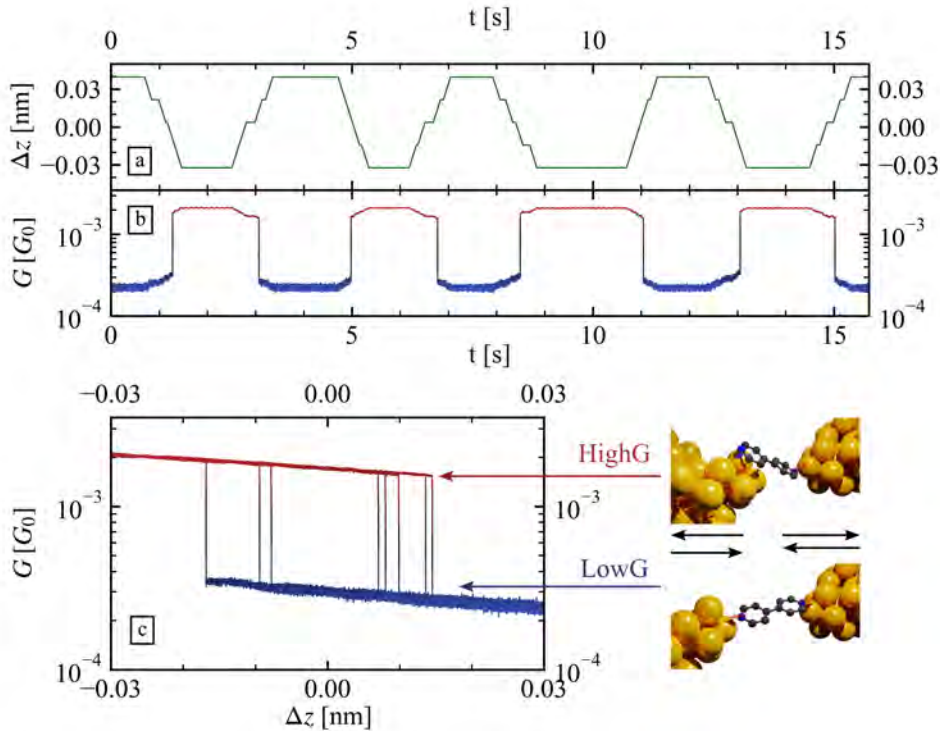


Figure 4.3: Mechanical switching demonstration. (a)-(b) Manually changing the piezo-voltage results in change of the conductance. As a result of the electrode distance change, the conductance switches from one state to the other and back. (c) Hysteric behavior of switching observed.

In my measurement, I slowly changed the voltage applied to the piezo actuator to open and close the gold electrodes while monitoring how the conductance changed depending on the voltage applied to the piezo actuator. I started from a metallic contact, changing the piezo voltage until the single-atomic contact ($1 G_0$) ruptured and then the HighG plateau appeared, followed by the LowG plateau, after further pulling. Then, I started to move the electrodes closer to each other, resulting in a jump in conductance to the value that corresponds to the HighG configuration. The mechanical switching based on the change in electrode distance could be repeated several times back and forth, the contact was held stable for several ten seconds, in contrast to the room-temperature measurements shown in Figure 4.1 in the introduction of this chapter, where the studied time frame was only around 60 ms. In Figure 4.3, I show an approximately 15 s long manually driven switching sequence consisting of four back-and-forth switching cycles between the HighG and LowG conductances. The electrode displacement and the conductance are shown in

Chapter 4. Binary Conductance Switching in Au–BPY–Au Single-molecule Nanowires

Figures 4.3(a) and 4.3(b), respectively. Plotting the conductance as a function of the electrode displacement (Figure 4.3(c)), it is observed that the HighG to LowG and the reverse LowG to HighG switch do not occur at the same electrode separation, which means that the $G(\Delta z)$ curve shows a hysteresis, and inside the hysteresis both configurations can be stable.

4.3 Current–voltage characteristics of Au–BPY–Au single molecular junctions

The precise control over experimental conditions, paired with the capability to maintain a stable molecular contact for an extended amount of time, makes the fundamental investigation of molecular contacts possible, e.g. with $I(V)$ characteristic measurements. My goal was to determine whether an electrical signal can induce a switching similar to the mechanical one. To achieve this, after forming a molecular contact by manually tuning the voltage applied to the piezo actuator, I performed $I(V)$ characteristic measurements in various configurations by applying a triangular bias signal between (–500 mV, 500 mV). In my measurements, many of the observed $I(V)$ characteristics were similar to those shown in Figure 4.4: at low bias voltage, the current state of the junction is stable; however, when the applied voltage is increased, the junction exhibits *binary probabilistic* switching between two distinct conductance states, where the switching rates increase with higher applied voltage.

After I collected 465 $I(V)$ curves, I determined the two switching conductances (fitting the linear portions of the $I(V)$ curve, where no switch occurs) for each curve and created a histogram of both the HighG (on) and LowG (off) conductance values and compared them to the low-temperature closing 1D conductance histogram from Figure 4.2(b). The calculated distributions of the on and off conductance states are plotted in Figure 4.5 with red and blue, respectively. The peak positions resemble the peaks of the low-temperature closing 1D conductance histogram plotted as a gray area graph, indicating that the molecular junction is switching between the HighG and LowG conductances from the closing segment of the measurement.

This observation is in agreement with the assumption that the difference between the peak positions in the opening and closing histograms is caused by the strain that acts on the junction in the opening process but is absent in the closing process. Due to the relatively slow movement of the electrode in the process, the strain acting on the molecule is reduced, the junction is relaxed throughout the $I(V)$ measurements, resulting in similar LowG and HighG conductance values as observed in the closing histogram. These findings indicate that, in addition to mechanical switching, we can also achieve electric switching between the two configurations of the BPY molecule.

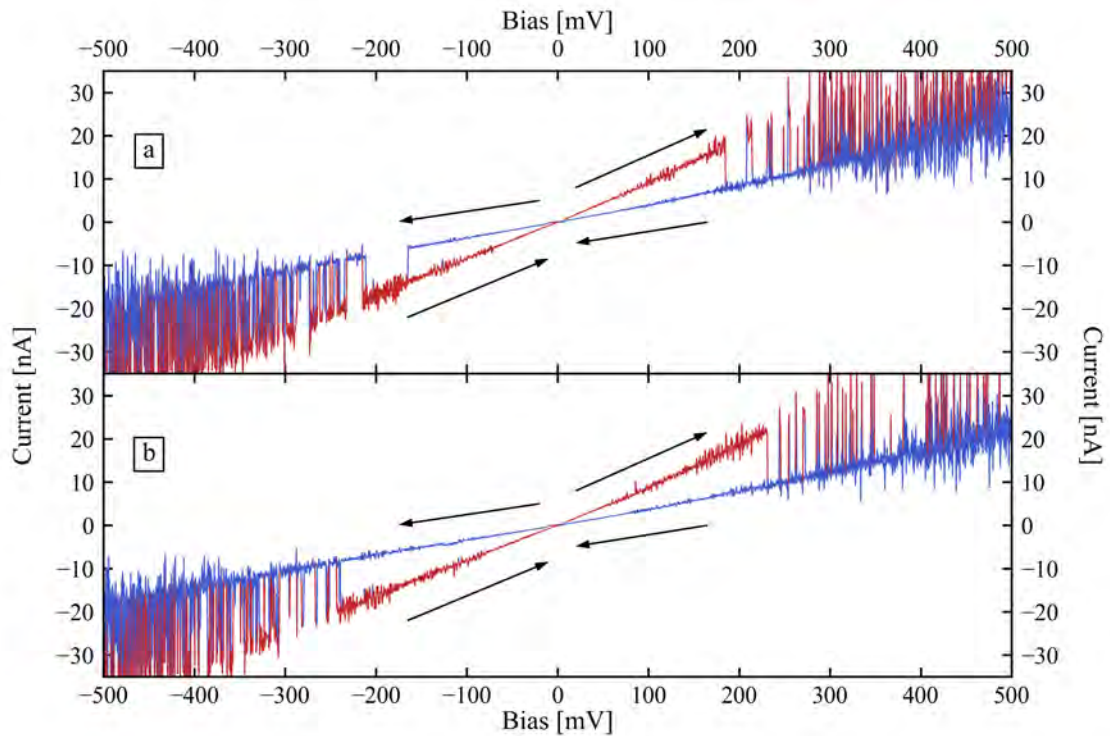


Figure 4.4: Current-voltage characteristics measurements at low temperature. (a)-(b) Sample $I(V)$ curves measured at $T = 4.2$ K. The arrows indicate the direction of the voltage-ramp.

4.4 Switching dynamics as a function of electrode separation

So far we have seen the hysteretic feature in the mechanical switching and the possibility to induce conductance switching by increasing the applied voltage. On the basis of these observations, we expect that inside the hysteresis, both the HighG and LowG configurations are possible, and the increasing bias induces switching when we are in the displacement range inside the hysteresis, and depending on the conductance plateau where we stop the movement, one of the conductance states is going to be more stable. To support these expectations, I have investigated the connection between the bistable electric switching and the displacement of the electrodes.

For this analysis, I manually searched for the displacement interval with hysteretic conductance switching with a low bias of 30 mV, to avoid electrical switching (see the black curve in Figure 4.6(a)). After finding the hysteresis, I moved to different displacement values along the hysteretic curve (marked with green dots in Figure 4.6(a)) and recorded the temporal evolution of the junction conductance under the influence of an elevated bias voltage of 150 mV. Snippets of the measured conductance over time are

Chapter 4. Binary Conductance Switching in Au–BPY–Au Single-molecule Nanowires

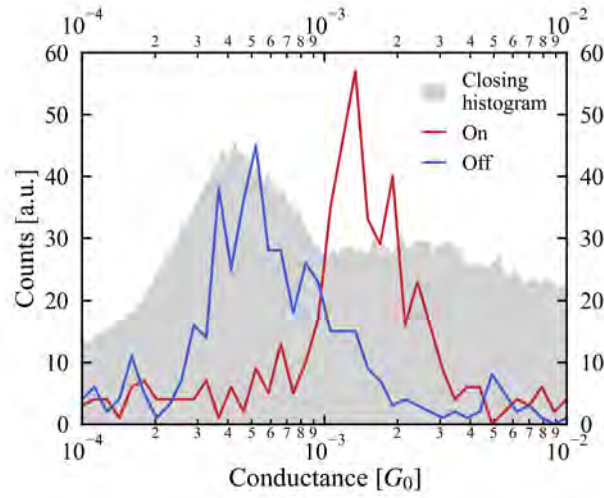


Figure 4.5: Comparison of conductances measured in the $I(V)$ characteristics cycles with 1D closing break junction histogram. The distribution of the conductance values determined from the slope of 465 $I(V)$ curves for the on (red) and off (blue) states. The gray shaded area serves as a comparison basis reproducing the closing conductance histogram from Fig. 4.2(b).

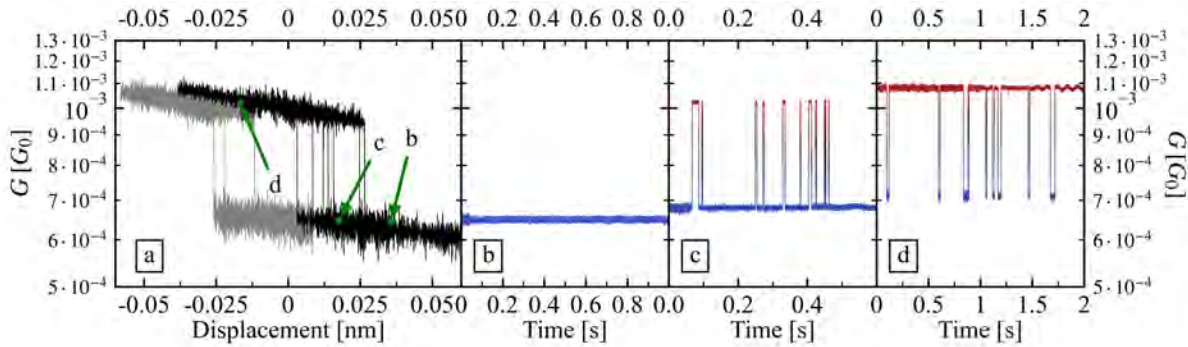


Figure 4.6: Demonstration of the switching mechanism. (a) Switching by modulating the piezo voltage manually results in a hysteresis. (b)-(d) Depending on where we stop in the hysteresis, we see different voltage-dependent switching: outside the hysteresis we see no switching ((b)), inside the hysteresis one of the states is more stable, and it depends on the conductance where we stopped the piezo modulation which one it is. ((c)-(d))

shown in Figures 4.6(b) to 4.6(d) for the points b - d , respectively. As expected based on my previous observations, the conductance remains stable at point b , and we observe a binary conductance switching inside the hysteresis loop (at point c), where the lower conductance state is more stable, since the junction clearly spends more time in that state. A binary conductance switching was also observed at point d , where the higher conductance

Chapter 4. Binary Conductance Switching in Au–BPY–Au Single-molecule Nanowires

state appeared to be more stable. At first glance, this might seem like an unexpected behavior, as point d lies outside the hysteresis loop. However, this can be explained by considering a small drift in electrode separation caused by thermal or mechanical instabilities, or by electrode relaxation commonly encountered in BJ measurements. The average displacement between the centers of the HighG and LowG conductance plateaus in the 2D conductance–displacement histograms ($\sim 2 \text{ \AA}$) is nearly an order of magnitude lower than the sub-Ångstrom displacement interval of the conductance hysteresis loop (see Figure 4.3(c)). Therefore, even a very small change in electrode separation can shift the junction out of the hysteresis region. Following the several-minutes-long measurement ($\sim 400 \text{ s}$), I looked again for the hysteretic displacement region and found that the hysteresis had shifted, placing point d near the center of the new hysteresis loop (see the gray curve in Figure 4.6(a)). By comparing the black and gray curves, I estimated that the drift of the molecular junction during the measurement was below 40 pm (approximately 15% of the gold–gold interatomic distance in a gold chain), which is a quite exceptional stability, highlighting the power of low-temperature measurements.

These measurements show that inside the hysteresis loop, both configurations are stable and an elevated applied bias voltage can induce switching between the two. From Figures 4.6(c) and 4.6(d) we can qualitatively read that in the observed switching interval, the system spends more time in the initial state. To quantitatively support this hypothesis, I also studied the distribution of the times spent in each conductance state.

I analyzed the recorded conductance (as shown in the top of Figure 4.7) when the elevated bias of 150 mV was applied. To determine the times spent in each state, the switching locations need to be determined first. I calculated the gradient of the conductance (bottom of Figure 4.7), because in cases where the conductance abruptly changes as a result of the switching event, a peak appears in the gradient. Peaks that exceed a predefined prominence are identified as switching events, and the direction of the switch is determined by the sign of the gradient (positive: LowG to HighG, negative: HighG to LowG). The time between two opposite switching events is the time spent in the HighG/LowG state denoted by τ_{HighG} , τ_{LowG} , respectively.

The difficulty of this method lies in finding the right prominence value: on the one hand, if we choose a prominence that is too large, there might be switching events that we miss; on the other hand, if the chosen prominence is not large enough, even small conductance fluctuations might be identified as switching events. I determined an optimal prominence value on a smaller but representative dataset. I visually found the switching positions, then fine-tuned the prominence value, so all switching events are correctly identified. Then, I tested how well the set value works by checking random portions of a larger dataset.

The proper determination of switching events is important because if we miss a switching event, not only do we have fewer data for the statistics but the time between two opposite switches deviates. For example, if the prominence value chosen is too large and we miss a LowG to HighG (HighG to LowG) switch, then the time spent in the LowG (HighG) configuration will be significantly longer, as it is the sum of the times spent in

Chapter 4. Binary Conductance Switching in Au–BPY–Au Single-molecule Nanowires

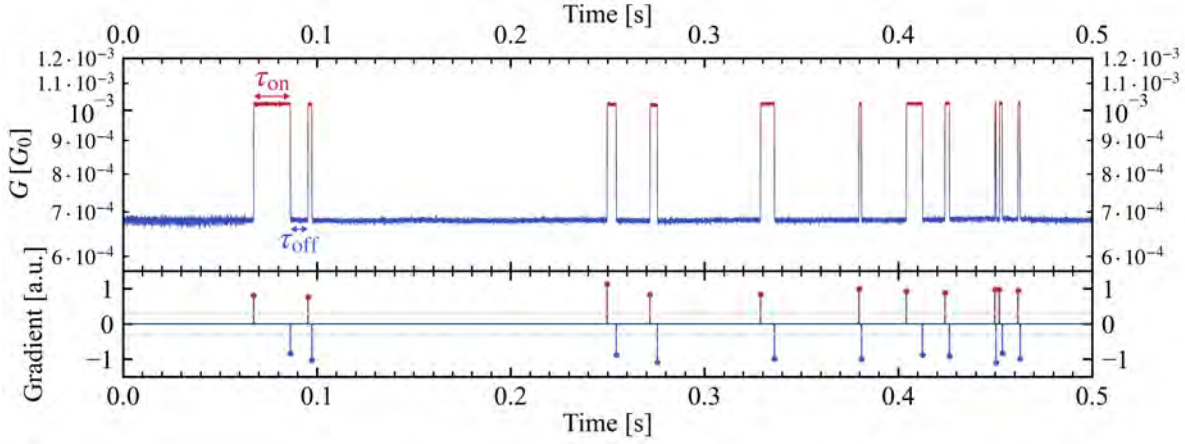


Figure 4.7: Location of switching events. To locate switching events, I calculate the gradient, because a sharp peak appears in the gradient where the conductance changes abruptly, which is easy to locate. The peaks that exceed a predefined prominence are identified as switching events and the time between two opposite switching events is the time spent in the HighG/LowG state denoted by τ_{HighG} , τ_{LowG} , respectively.

the LowG, the HighG and the next LowG (HighG, LowG and next HighG) configuration. If the chosen prominence value is large enough to not misidentify small fluctuations as switching events, but still small enough, then if the conductance change occurs throughout several datapoints, the gradient is higher than the prominence for each of these points. Then, all of these may be identified as switching events in the same direction, which is clearly an error, as the switching always happens between two distinct conductance values, so the adjacent switching events should happen in the opposite direction. These errors can be eliminated with an extra filter condition that takes the position of the largest gradient to be the location of the switching event. This introduces some uncertainty in the accurate location of the switching event, but in most cases all switching events are identified.

To study the distribution of the switching times, I assembled the observed switching times to a histogram that is equidistantly binned along the logarithmic time axis. I fit the data with the exponential probability density function $\rho(\tau) = (A/\tau_0) \cdot \exp(-\tau/\tau_0)$, where τ_0 is the average time, and the term A accounts for the unnormalized nature of the distribution. The latter is mostly related to a minor number of missing data points in the distribution below the temporal resolution of our setup. Integrating this density function for the width of the bin i we obtain

$$n_i^{\text{log}} = Ae^{-\tau/\tau_0} \left(1 - e^{-\left(10^{\frac{1}{N}} - 1\right) \cdot \tau/\tau_0} \right), \quad (4.1)$$

where n_i^{log} is the number of data points in bin i , and N is the number of logarithmically

Chapter 4. Binary Conductance Switching in Au–BPY–Au Single-molecule Nanowires

equidistant bins within one decade. Note, that this function simplifies to the common

$$n_i^{log} = \frac{A}{\tau_0} e^{-\tau/\tau_0} \cdot \tau \cdot \frac{1}{N} \quad (4.2)$$

formula in the $N \rightarrow \infty$ limit. In my analysis, I fit the switching time histograms with Equation 4.1 using typical binning values of $N = 8$.

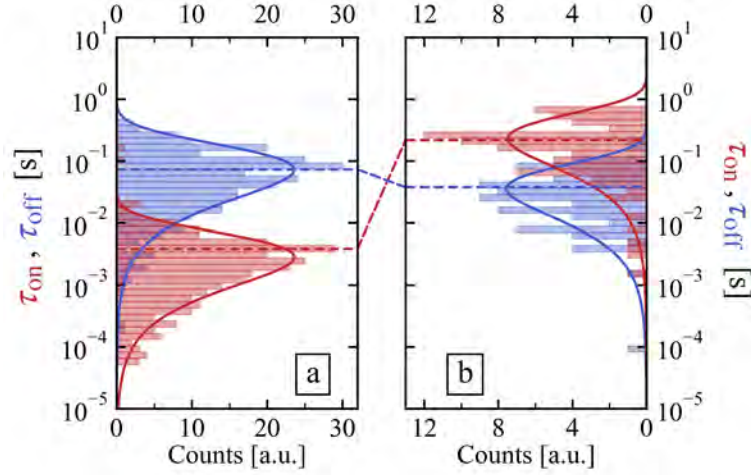


Figure 4.8: Switching times distribution ((a)-(b)) *Distribution of the time spent in the on and off states at points c and d in Figure 4.6(a), respectively. The switching rates are tuned by changing the distance between the electrodes.*

In Figures 4.8(a) and 4.8(b) I plotted these distributions for points *c* and *d*, respectively. I found that by changing the displacement, we can tune the relative weight of the conductance states because the conductance plateau at which we stop the movement of the piezo will be more stable.

Based on these and further similar measurements, we found the following clear tendencies:

- (i) The bistable electrical switching is observed around the displacement range of the low-bias conductance hysteresis (see Figures 4.6(c) and 4.6(d)).
- (ii) Within this range, the average times spent in the two states cross each other: at a smaller displacement the HighG state is dominant, while at a larger displacement there is a shift toward the LowG state (Figures 4.8(a) and 4.8(b)).
- (iii) Moving further away from the hysteresis, the electrical switching vanishes (Figure 4.6(b)), and despite elevated voltages, the corresponding state remains stable.

4.5 Voltage dependence of the switching dynamics

In the measurement described above, the molecular junction was created and the electrode spacing was tuned manually. Although this method is well suited for the individual analysis of single junctions, performing statistical analysis on larger numbers of molecular junctions is difficult. To enable a statistical study of the characteristics of voltage-induced molecular switching, I performed automated measurements using the FPGA-based measurement system introduced in chapter 3. I programmed and used a modified break junction measurement scheme, in which the real-time FPGA controller monitors the conductance and stops the electrode movement once a predefined trigger conductance is reached. Then, when the voltage signal is over, the opening of the junction continues until the junction ruptures, which is followed by the closing process, where the junction is reformed and the whole process is repeated several times. At this point, the voltage on the piezo actuator (i.e. electrode separation) is held constant, and an arbitrary bias voltage signal is applied to the junction. In my measurements, I used a trigger conductance of $G = 0.005 G_0$ and applied a staircase-like bias voltage pattern with 15 s long plateaus (see Figure 4.9(a)) and repeated the automated measurement 8000 times. Approximately 8% of the measurements produced molecular contacts that were stable throughout the voltage sweep, and of these stable molecular contacts $\approx 5\%$ (35) matched the displacement range, where voltage-dependent bistable switching was observable. It is important to note that this number is partially related to the low molecular pick-up rate in low-temperature measurements [46] and the small width of the hysteretic loop.

I used these 35 independent traces to study the voltage dependence of the bistable switching. The analysis of an individual measurement is shown in Figures 4.9(b) to 4.9(f). The distributions of the switching times (τ_{HighG} and τ_{LowG}) are displayed in Figures 4.9(c) to 4.9(f) for the 15 s long plateaus with the driving voltages 50 mV, 100 mV, 125 mV and 150 mV, respectively. At 100 mV, 125 mV and 150 mV driving voltages, a distinct peak appears in the distributions, and the position of the peak shifts toward shorter times as the applied voltage increases. In the 50 mV measurement, the significantly lower number of switching events results in fewer counts, so the peaked nature of the distribution is less pronounced. However, the characteristic values τ_{HighG} and τ_{LowG} can still be determined, showing that lower voltage results in a slowing of the switching process. The distributions of τ_{HighG} and τ_{LowG} are well fitted by the exponential probability density function defined above (Equation 4.1), plotted with solid lines in Figures 4.9(c) to 4.9(f)). This exponential distribution implies stochastic switching events that are independent of the time elapsed since the last switching event. The $\langle \tau_{\text{HighG}} \rangle$ and $\langle \tau_{\text{LowG}} \rangle$ average times are extracted from the fits and plotted versus the driving voltage in Figure 4.9(b) with a logarithmic timescale. The colors of the points correspond to the colors of the distributions. The points in both the HighG and LowG datasets fall on a straight line, which is confirmed by a good fit with a linear function on the logarithmic timescale (i.e. $\log(\langle \tau_{\text{HighG/LowG}} \rangle / \tau_0) = a_{\text{HighG/LowG}} + b_{\text{HighG/LowG}} \cdot V_{\text{bias}}$, where the reference time $\tau_0 = 1$ s, to ensure a dimensionless argument for the logarithm), as plotted with solid lines.

Chapter 4. Binary Conductance Switching in Au–BPY–Au Single-molecule Nanowires

This means that as the voltage increases linearly, the switching in both states accelerates exponentially.

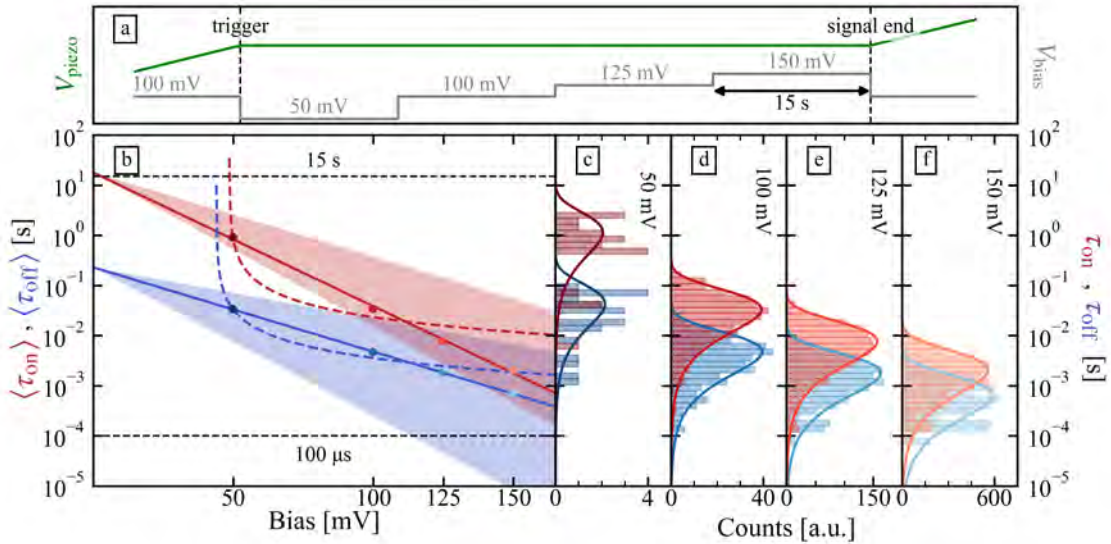


Figure 4.9: Bias dependent switching times. (a) **Layout of the measurement:** after a trigger conductance is reached, the piezo movement stops and a step-like bias signal is applied as depicted in the figure. For each step, the times spent in each conductance state are determined and statistically analyzed. (b) **Average times spent in the on (red) and off (blue) state.** The solid line is the line fitted to the measured data, and the dashed line is the expected behavior from the theory. The shaded areas are enclosed by the maximum and minimum slope values at fixed intercept values. Black dashed lines mark the limiting timescales: the upper limit is 15 s, the length of a plateau, while the lower limit is 100 μs , the bandwidth of the measurement. (c)-(f) **Distribution of the times spent in each state at different bias steps.** Increasing the bias voltage shortens the time spent in both states.

To confirm these tendencies observed in the individual measurement, I investigated the correlations between the $a_{\text{HighG/LowG}}$ intercept and $b_{\text{HighG/LowG}}$ slope values for the 35 measurements (Figures 4.10(a) to 4.10(d)). Despite the scattering of the data, clear trends can be identified. Within a given state (HighG/LowG), a larger intercept is consistently associated with a larger slope (see Figures 4.10(a) and 4.10(b)) and similarly, if a state shows a larger slope or intercept, the other state tends to show larger corresponding values as well (see Figures 4.10(c) and 4.10(d)). The clear correlation between the slope values b_{HighG} and b_{LowG} in Figure 4.10(c) supports the idea that switching speeds up simultaneously in both states. This is further illustrated by the red- and blue-shaded regions in Figure 4.9(b), which were constructed using the intercept values for the on and off states of the example data in Figure 4.9(b), but accounting for the variation of the slope values around these intercepts across all data. This variation is also shown by the horizontal error bars in Figures 4.10(a) and 4.10(b)), where the dark (filled) red and blue dots highlight the example trace shown in Figure 4.9(b).

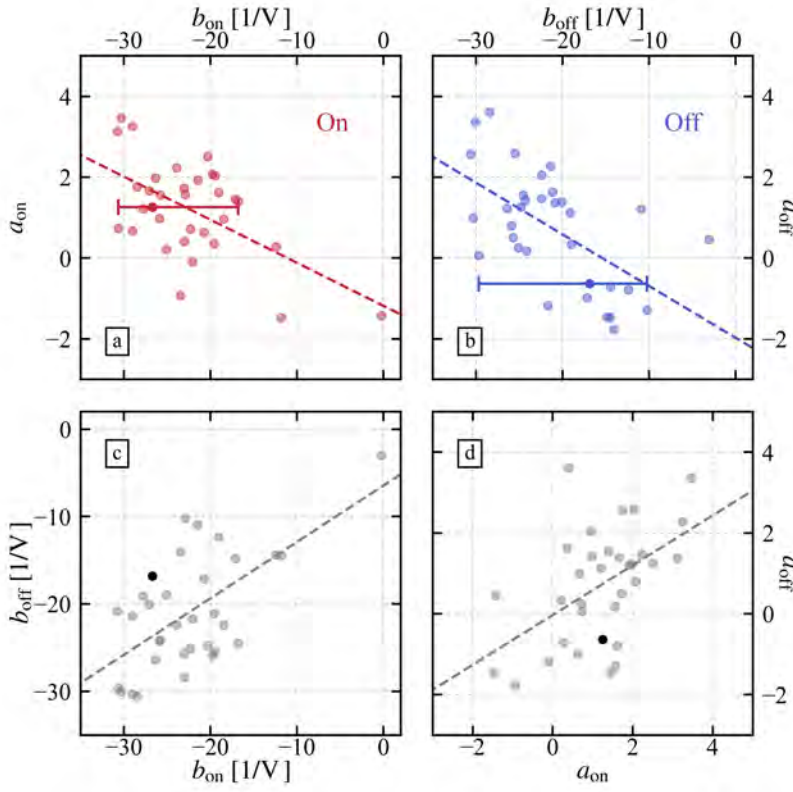


Figure 4.10: Statistical analysis of the switching times. ((a)-(d)) *Statistics of the parameters of the line fit to the average switching times for 35 separate measurements. The darker points emphasize the parameters for the measurement for which the analysis is illustrated in Figures 4.9(b) to 4.9(f). For reference, the dashed lines in all panels indicate the best-fitting linear functions.*

In summary, the analysis of the voltage dependence of the switching dynamics leads to the following key conclusions:

- (i) The switching times in both states are well fitted with an exponential probability density function (Figures 4.9(c) to 4.9(f)).
- (ii) In both states, the switching speeds up exponentially as the applied voltage increases linearly (Figure 4.9(b)).
- (iii) The switching times of both the HighG and the LowG states accelerate simultaneously, while the dominant state generally remains unchanged throughout the investigated voltage range (Figure 4.9(b)).

It is important to note that this latter behavior contrasts sharply with mechanical actuation, which clearly reverses the dominance of the two states, as shown in Figures 4.8(a) and 4.8(b). This distinct difference between the effects of mechanical manipulation and

voltage control also suggests that the applied voltage does not directly affect the electrode separation.

4.6 Comparing the experimental results with possible theoretical models

Finally, I discuss our observations on bistable resistance switching using simple model considerations. We modeled the molecular states using a double-well potential in configuration space, taking into account the energy E released by the electrons to the molecule during a single scattering event (see Figure 4.11). In our general model, the transition between metastable states occurs with probability $\Gamma(E)$ after the molecule receives E energy from the electrons. Based on the fit of the force measurements model in the literature, the binding energies of the HighG and LowG molecular configurations are 1.6 eV and 0.9 eV, respectively, showing a significant energy difference of around 700 meV [86]. In principle, switching between states with such an energy offset would require the overcoming of an even higher barrier (E_b) in the lower energy configuration. However, these energy values correspond to fully relaxed molecular configurations. In our case, the switching occurs within the sub-Ångstrom hysteretic conductance region, where both states remain stable. Here, we expect the HighG state to be stretched and the LowG state to be compressed, leading to a much smaller energy difference and barrier between the two configurations. This interpretation is consistent with our observation that a voltage range of approximately ≈ 100 mV can trigger the switching.

In our model, basically four possible scenarios can be distinguished for the energy release by the electrons: when electrons pass through the molecular contact from electrode 1 (electrode 2) towards electrode 2 (electrode 1), from the top down (bottom up) direction as in Figure 4.11; and when electrons from electrode 1 (electrode 2) do not pass through the molecular contact, i.e. they are scattered back into electrode 1 (electrode 2).

Let us consider the first case, where the electrons come from electrode 1 and travel to electrode 2. The probability of a scattering event within a unit time interval ($P_{el,1\rightarrow 2}^{-E}$) is proportional to the transmission probability through the molecule (\mathcal{T}) and to the probability of scattering from an occupied state in the higher chemical potential electrode to an unoccupied state at lower energy in the lower chemical potential electrode, which is described by the integral of the Fermi function:

$$P_{el,1\rightarrow 2}^{-E} \sim \mathcal{T} \cdot \int f_1(\varepsilon) \cdot (1 - f_2(\varepsilon - E)) d\varepsilon, \quad (4.3)$$

where f_1 and f_2 are the Fermi functions of the two electrodes with a chemical potential difference $\mu_1 - \mu_2 = eV$, and we consider $eV > 0$, i.e. the first electrode has higher chemical potential. By applying the well-known $\int f_0(\varepsilon)(1 - f_0(\varepsilon - a)) d\varepsilon = a \left(e^{\frac{a}{kT}} - 1 \right)^{-1}$ identity

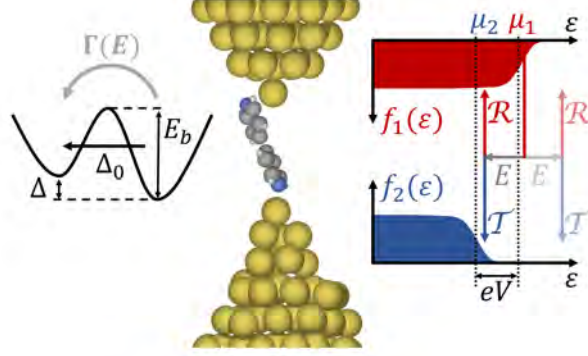


Figure 4.11: Illustration of the model considerations: the double-well potential with energy difference Δ , barrier height E_b and tunneling probability Δ_0 between the two states (left panel), Fermi distribution of the electrodes with applied drive voltage eV and transmission (reflection) coefficient \mathcal{T} (\mathcal{R}) (right panel). The probability of a switching event consists of two parts: (i) the probability P^{-E} that an electron in an occupied state releases energy E and transitions to an unoccupied state (right panel), and (ii) the probability $\Gamma(E)$ that the molecule switches to its other state after absorbing this energy (left panel). In the vibrational pumping model, the absorption of energy E from molecular vibrations by the electrons must also be taken into account (see the semitransparent arrows in the right cartoon). In this case, not only the transmitted electron but also the reflected electron can access unoccupied final states, and thus the ration $\mathcal{R}/\mathcal{T} \approx 10^3$ makes the cooling of the vibrational mode much more efficient than the pumping [P1].

for the f_0 Fermi function the above integral simplifies to

$$P_{el,1 \rightarrow 2}^{-E} \sim \mathcal{T} \cdot \frac{E - eV}{e^{\frac{E - eV}{kT}} - 1}, \quad (4.4)$$

and similarly for the other three scenarios:

$$P_{el,2 \rightarrow 1}^{-E} \sim \mathcal{T} \cdot \frac{E + eV}{e^{\frac{E + eV}{kT}} - 1}, \quad (4.5)$$

$$P_{el,1 \rightarrow 1}^{-E} = P_{el,2 \rightarrow 2}^{-E} \sim \mathcal{R} \cdot \frac{E}{e^{\frac{E}{kT}} - 1}. \quad (4.6)$$

In the zero-temperature limit, later two equations yield zero values because the numerator in the exponential function is always positive. This is also true for Equation 4.4 when $eV < E$, but the limit $eV > E$ yields $\mathcal{T} \cdot (eV - E)$.

In the following, I analyze simple cases of our general model in which the molecule can gain energy, and compare the expected voltage scaling of the switching time with the experimental results.

4.6.1 Simple two-level system (TLS) models

First, I discuss the coherent two-level system model with a finite energy difference (Δ) and a finite tunneling probability between the two states (Δ_0) [32, 87]. After diag-

Chapter 4. Binary Conductance Switching in Au–BPY–Au Single-molecule Nanowires

onalyzing the corresponding TLS Hamiltonian, a two-state system with a well-defined $E_{TLS} = \sqrt{\Delta^2 + \Delta_0^2}$ excitation energy is yielded. Considering a $eV > E_{TLS}$ voltage excitation and $T = 0$ K temperature (i.e. $E_{TLS}, eV \gg kT$), Equation 4.4 simplifies to

$$P_{el,1 \rightarrow 2}^{-E_{TLS}} \sim \mathcal{J} \cdot (eV - E). \quad (4.7)$$

The further processes (Equations 4.5 and 4.6) provide practically zero contribution. Assuming a constant energy-independent tunneling probability and electron-molecule coupling strength, the voltage scaling of the switching time is obtained as $\tau \sim (eV - E_{TLS})^{-1}$.

As another approach, we can consider an incoherent two-level system with a wide barrier, excluding tunneling through the barrier. In this case, transition occurs only when the energy released by the electrons is exceeds ($E > E_b$).

In this limit, similar to the coherent case, Equation 4.4 simplifies to Equation 4.7 and the voltage scaling of the overall switching rate is obtained by an energy integral within the $E_b < E < eV$ energy window:

$$P \sim \int_{E_b}^{eV} \mathcal{J} \cdot (eV - E) dE = \frac{\mathcal{J}}{2} \cdot (eV - E_b)^2, \quad (4.8)$$

i.e. the switching time scales with $(eV - E_b)^{-2}$.

The red and blue dashed lines in Figure 4.9(b) represent the best fits using the $\tau \sim 1/(eV - E)$ voltage scaling, which is clearly inconsistent with the experimental data. Even if we neglect the divergence at $eV = E$, which may be smoothed by a broader energy distribution, the high bias $1/V$ scaling predicted by this simple model is significantly shallower than the voltage dependence observed in the experimental data. The same discrepancy applies to the $1/V^2$ scaling in the incoherent model. The $1/V$ ($1/V^2$) dependency would yield a factor of 3(9) speedup by increasing the drive voltage from 50 mV to 150 mV. This clearly deviates from the observed ≈ 2 orders of magnitude speed-up (see Figure 4.9(b)). In Figures 4.10(a) and 4.10(b) this 3-fold and 9-fold speed-up would relate to slope values of $b \approx -5 \text{ V}^{-1}$ and $b \approx -10 \text{ V}^{-1}$, which are also much shallower slopes than the typically observed $b \approx (-30 - -20) \text{ V}^{-1}$ values. Consequently, these TLS models can be excluded.

4.6.2 Temperature activated switching model

So far, we have considered only the case $eV > E_{TLS}$ (or $eV > E_b$), however, when the effect of finite temperature is taken into account, a transition can also occur for $eV < E_{TLS}$ (or $eV < E_b$).

In our experiment, we use 50 – 150 mV drive voltage, and we consider the same order of magnitude for the excitation energies. These energy scales are orders of magnitude larger than the $kT \approx 0.36$ meV thermal energy at 4.2 K temperature. In this limit Equation 4.4 simplifies to

$$P_{el,1 \rightarrow 2}^{-E} \sim \mathcal{J} \cdot (E - eV) \cdot e^{-\frac{E - eV}{kT}}. \quad (4.9)$$

Chapter 4. Binary Conductance Switching in Au–BPY–Au Single-molecule Nanowires

The other processes described in Equations 4.5 and 4.6) yield small contributions, their effect can be neglected in comparison with the dominant term in Equation 4.9.

In the $eV < E_{TLS}$ limit of the coherent two-level system model, this result yields the following voltage scaling of the switching time:

$$\tau \sim \mathcal{J}^{-1} \cdot (E_{TLS} - eV)^{-1} \cdot e^{\frac{E_{TLS} - eV}{kT}}. \quad (4.10)$$

In a similar $eV < E_b$ limit of the incoherent two-level system model, the overall switching rate is obtained by integrating Equation 4.9 for $E > E_b$ energies:

$$P \sim \int_{E_b}^{\infty} \mathcal{J} \cdot (E - eV) \cdot e^{-\frac{E - eV}{kT}} dE = \mathcal{J} \cdot kT \cdot (E_b - eV + kT) \cdot e^{-\frac{E_b - eV}{kT}}. \quad (4.11)$$

The switching time is the inverse of this switching rate.

The voltage scaling in both the coherent and incoherent cases is determined by the $\sim \exp((E - eV)/kT)$ exponential term. This scaling would provide a slope of $b = -e \cdot \log(e)/kT \approx -10^3 \text{ V}^{-1}$, whereas the largest measured slopes are restricted to $b \approx -30 \text{ V}^{-1}$ (see Figures 4.10(a) and 4.10(b)). Furthermore, since at $T = 4.2 \text{ K}$ the energy in the numerator of the exponent is orders of magnitude larger than the thermal energy in the denominator, we can conclude that such a temperature-activated process can be excluded also.

4.6.3 Vibrational pumping model

Previously, we have considered models in which electrons transfer enough energy to switch the molecule in a single step. Alternatively, in multistep processes, electrons release smaller quanta $E = \hbar\omega$ into a molecular vibrational mode, with the transition occurring once the accumulated energy in this vibrational mode reaches the barrier energy (Figure 4.12). To describe the vibrational pumping, we implement the local heating model in Ref. 88 on a single-molecule structure.

In this limit, not only the $\hbar\omega$ energy release to the vibrational mode, but also the $\hbar\omega$ energy absorption from the vibrational mode should be considered. The corresponding Fermi function integrals are obtained by replacing $E = \hbar\omega$ by $-E = -\hbar\omega$ in Equations 4.4 to 4.6. At $T = 4.2 \text{ K}$ the zero temperature limits can be considered, yielding $P_{el,1 \rightarrow 2}^{+E} \sim \mathcal{J} \cdot (E + eV)$, $P_{el,2 \rightarrow 1}^{+E} = 0$ and $P_{el,1 \rightarrow 1}^{+E} = P_{el,2 \rightarrow 2}^{+E} \sim \mathcal{R} \cdot E$. Note that vibrational pumping obviously requires $eV > \hbar\omega = E$. Taking into account that the energy release probability from the vibrational mode scales with its occupation number n , while the probability for energy absorption by the vibrational mode scales with $n + 1$, and summing over all possible non-zero energy release and absorption processes for the electrons, the following balance equation can be obtained:

$$(n + 1) \cdot \mathcal{J} \cdot (eV - \hbar\omega) = n \cdot [\mathcal{J} \cdot (\hbar\omega + eV) + 2\mathcal{R} \cdot \hbar\omega]. \quad (4.12)$$

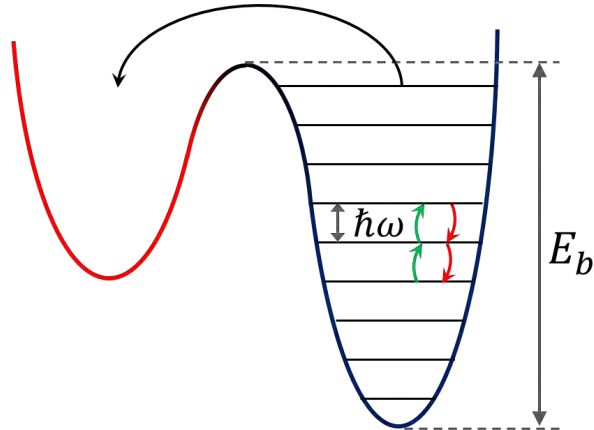


Figure 4.12: Vibrational pumping model: *the transition occurs when the vibrational mode is pumped to the barrier height energy (E_b) in the actual state, through electrons releasing (absorbing) $\hbar\omega$ quanta to (from) the vibrational mode [P1].*

This balance yields the equilibrium average occupation number of the vibrational mode as:

$$\bar{n} = \frac{\mathcal{T}}{2} \cdot \left(\frac{eV}{\hbar\omega} - 1 \right). \quad (4.13)$$

Considering the $\mathcal{T} \approx 10^{-3}$ transmission probability of the molecule, the $eV < 150$ mV voltage range and $\approx 10 - 100$ meV typical vibrational energies [89], $\bar{n} \ll 1$ follows, i.e. vibrational pumping and related local overheating of the junction is unrealistic. As a simple explanation, this result is related to the fact that the vibrational mode is much more efficiently cooled than excited in the $\mathcal{T} \ll 1$ limit.

4.6.4 Double-well potential inversion model

Following the approach in Ref. 51, we can consider a scenario in which the electric field acting on the junction induces a deformation of the potential barrier as illustrated in Figure 4.13. In this case, increasing the voltage lowers the barrier for the initially favored state while raising it for the initially unfavored state (see the bottom part of the figure). This would be expected to yield a crossing of the switching times, as illustrated in the top panel. However, our experimental results do not show this crossing; instead, the switching times speed up simultaneously as the voltage is increased, i.e., we exclude this model.

4.6.5 Heuristic model relying on the molecule's energy dependent transition probability

We have seen that both temperature activation and the vibrational pumping are unrealistic in our experimental situation. Simple two-level system models, which rely only on the voltage dependence of the Fermi function integrals and a constant Γ_0 , also fail to

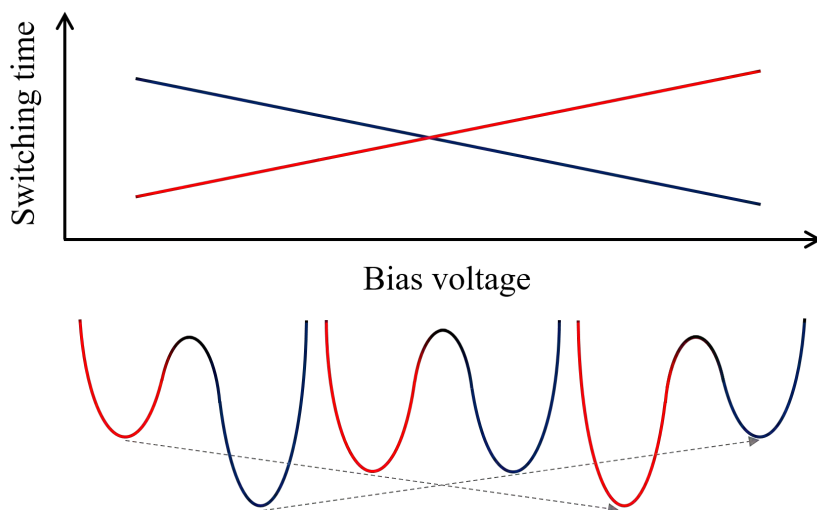


Figure 4.13: Double-well potential inversion model. *The bottom part shows the reversal of the dominance between the two potential wells as the voltage increases, which results the crossing of the switching times (see the top part). The red/blue colors illustrate the high and low conductance states, respectively [P1].*

capture the observed behavior. To explain the simultaneous exponential decrease of the switching times with linearly increasing voltage, we can consider a strong (exponential) energy dependence of the molecule’s transition probability $\Gamma(E)$. This could reflect an energy-dependent tunneling probability between two conformational states, as implied in the figure, but several other mechanisms, like barrier reduction under applied voltage or the influence of electron-wind forces, may also contribute. A more complete understanding of the underlying microscopic processes would require first-principles modeling.

4.7 Conclusion

In this chapter, I have presented our investigation of voltage-controlled probabilistic conductance switching in Au–4,4′-bipyridine–Au single-molecule junctions, utilizing a low-temperature mechanically controllable break junction (MCBJ) setup. I have demonstrated that bistable conductance switching (where the system alternates between two distinct molecular binding configurations) persists at cryogenic temperatures. Furthermore, I have shown that binary switching between these configurations can be induced not only through mechanical manipulation but also via the application of an external voltage. In this voltage-controlled switching regime, the relative dominance of the two conductance states can be tuned via electrode displacement, while the applied voltage governs an exponential acceleration of the switching dynamics. The clear distinction between mechanical and electrical control mechanisms suggests fundamentally different underlying processes: mechanical actuation alters the preferred molecular configuration, whereas voltage pri-

Chapter 4. Binary Conductance Switching in Au–BPY–Au Single-molecule Nanowires

marily modulates the transition kinetics without affecting the structural configuration of the electrode (i.e. electrode separation).

Through analysis of the voltage-dependent switching rates and comparison with various theoretical models, I have demonstrated that simple two-level system models, thermally activated processes, vibrational pumping mechanisms, and double-well potential inversion models can all be excluded as the primary explanations for the observed behavior. Instead, we propose a heuristic model based on the exponential energy dependence of the molecule's transition probabilities, providing a plausible framework for understanding the voltage-controlled switching dynamics observed in our experiments.

Chapter 4. Binary Conductance Switching in Au-BPY-Au Single-molecule Nanowires

Chapter 5

Temporal Noise Measurements on Au–BPY–Au Single-molecule Nanowires

As presented in chapter 2, the investigation of $1/f$ noise in molecular junctions can provide valuable information on the transport properties and the underlying molecular configurations. Previous studies have demonstrated that the resistance scaling of the noise is closely linked to the nature of the molecule–metal coupling. Specifically, it depends on whether the electronic orbitals responsible for charge transport also participate in the formation of a chemical bond (*through-bond* coupling) or if the coupling is due to spatial overlap without direct chemical bonding (*through-space* coupling) [29]. By exploiting these characteristics, noise measurements can be used to distinguish between different molecular junction configurations. For example, they can differentiate monomer single-molecule junctions, which exhibit through-bond coupling at both electrode interfaces, from dimer junctions, where the intermolecular coupling is dominated by through-space interactions [30]. Furthermore, the resistance scaling of noise can be used to reveal molecular folding events, where a folded and unfolded molecule configuration shows through-space and through-bond characteristics, respectively [90].

Such noise measurements pose an additional challenge beyond basic break-junction conductance trace measurements: It is not sufficient to simply apply a low-noise measurement technique; the configuration (i.e., the conductance state) must also be stabilized during the noise measurement period. In chapter 2, two different techniques were introduced for the noise analysis of molecular junctions. One method uses very slow break-junction traces, taking advantage of the plateau-like stability of certain configurations. In this case, the conductance remains stable during the slow tuning of the electrode separation, allowing the noise spectrum to be calculated within these stable regions [72]. The other more direct “trial-and-error” approach involves randomly stopping mid-rupture and holding the electrodes stationary to measure current fluctuations as a function of time [29, 30].

Chapter 5. Temporal Noise Measurements on Au–BPY–Au Single-molecule Nanowires

I used the first method (also known as *temporal noise measurement*) to investigate the noise characteristics of Au–BPY–Au molecular junctions. This method has the advantage that it does not require special alterations to the measurement system and, under ideal conditions, can provide large datasets suitable for detailed statistical analysis, such as the PCA-based trace selection technique introduced in chapter 2. In this chapter, I first present how I implemented and performed the temporal noise measurements. Then, I demonstrate how the EPCP-based trace selection technique can help gain more detailed insight into *configuration-specific* noise behavior.

5.1 Basics of temporal noise measurement technique

To investigate the noise phenomena of Au–BPY–Au molecular junctions, I implemented the framework of temporal noise measurement based on methods reported in the literature and applied it to the molecular junction system. This technique is essentially a standard break-junction conductance measurement but requires several specific conditions: (i) very slow tuning of the electrode displacement (i.e., the opening/closing of the junction) to ensure that conductance states remain stable over the timescale of the noise measurements; (ii) current measurement using a digitizer card equipped with an anti-aliasing filter, which suppresses frequency components above the Nyquist-Shannon limit and is crucial for obtaining accurate power spectral density (PSD) data; and (iii) advanced data analysis, as reliable noise characterization requires not only the calculation of the noise spectra but also data preconditioning and the application of filtering criteria to exclude anomalies caused by instabilities or abrupt jumps between plateaus.

An example conductance trace from my temporal noise measurement is shown in Figure 5.1(a). The trace was recorded at room temperature with a 100 mV voltage bias, a 50 kHz sampling rate, and a piezo voltage sweep rate of 8 V/s. The long and stable molecular plateau suitable for noise analysis is visible in the middle of the trace. During my work, I developed the codes required for the analysis of such traces and validated their operation. Furthermore, I studied how the parameters affect the results and, based on this, determined the optimal parameter values for the Au–BPY–Au system, providing a baseline for future studies on other molecular systems.

My evaluation process includes the following main steps: (i) identifying the start of the molecular plateau; (ii) defining the moving time windows for calculating the noise spectra; (iii) filtering based on stability; (iv) calculating the noise spectra and the integrated noise; and (v) repeating the above steps for the entire dataset. In the following, I briefly review the details of this evaluation. To locate the molecular plateau, I aligned each trace such that it crossed the $2 \cdot 10^{-2} G_0$ conductance at 0 V piezo voltage. It is worth noting that, based on my experience, skipping the initial 50 points helps exclude instabilities at the start of the molecular plateau. Then the temporal evolution was analyzed using sliding windows of 256 points (5.12 ms) with a 64 point (quarter window) overlap between successive windows. Two adjacent windows are highlighted with blue

Chapter 5. Temporal Noise Measurements on Au–BPY–Au Single-molecule Nanowires

rectangles in Figure 5.1(a), and the corresponding conductance traces are shown enlarged in Figures 5.1(c) and 5.1(d). For further analysis, only windows where the conductance ratio between the start and end of the segment was less than two (stability criterion) were kept. The PSD (S_G) of these stable windows was calculated via fast Fourier transform (FFT). Figure 5.1(b) shows two example $1/f$ -like PSDs for the highlighted windows. Note that, compared to the $1/f$ reference line (red dashed), the PSDs of the molecular junction exhibit a $1/f$ -like behavior with an exponent γ between -1.3 and -1.5 .

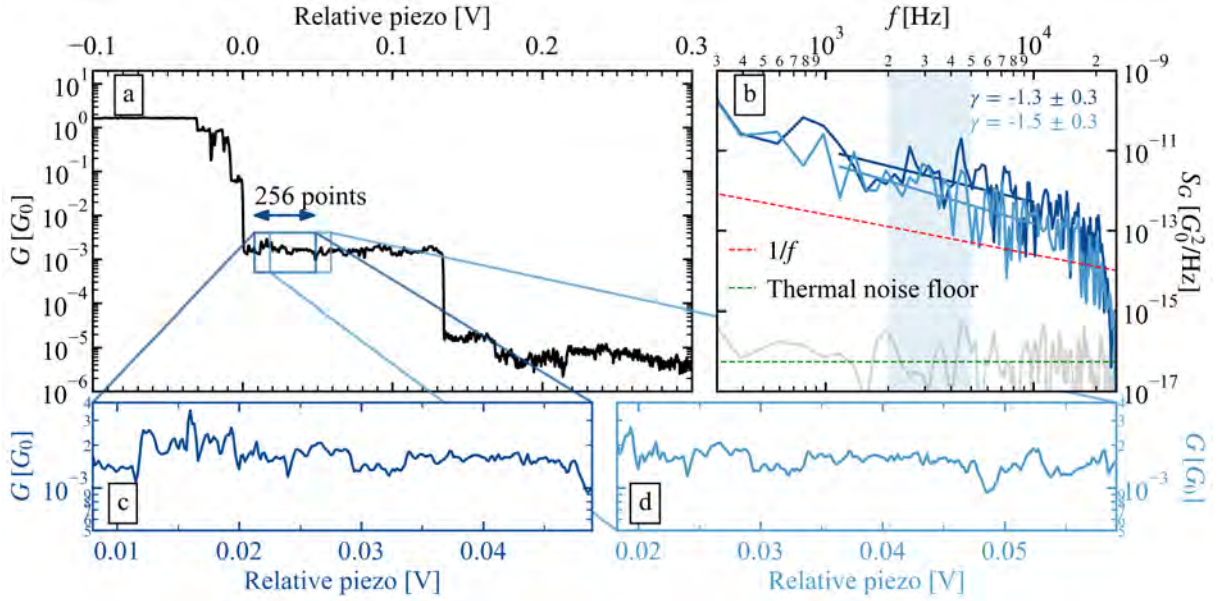


Figure 5.1: Example slow MCBJ trace for temporal noise analysis (a) Example MCBJ opening trace measured at 100 mV bias and 8 V/s piezo voltage sweep rate. Two analyzed windows are highlighted with different shades of blue boxes to demonstrate the procedure (others not displayed for clarity). **(b) Power spectral densities** (light and dark blue lines) are calculated by FFT from fixed-length (256 points) moving (by 64 points) regions of the conductance traces (dark and light blue rectangles in (a)). Gray curve shows the significantly smaller instrumental noise of our measurement system in comparison to the expected thermal noise floor (green dashed line). The red dashed line is a guide corresponding to the $S_G \sim 1/f$ frequency dependence. From these spectra, the relative conductance noise is calculated by numerical integration (see text) to obtain the $\Delta G/G$ values for each window of each trace. The shaded area shows the integration range. **(c)-(d) Sample windows with 256 measurement points.** The snippets of the measurement as highlighted in panel (a), using matching colors with the corresponding noise spectra in panel (b).

As part of the development of the temporal noise analysis technique, I also analyzed the baseline noise level by measuring the PSD of a broken junction (*instrumental noise*), shown as a flat gray line in the figure. When the junction is ruptured, noise mainly originates from the data acquisition card and current amplifier. The PSD of the molecular

contact clearly lies well above both the instrumental noise level and the thermal noise floor calculated from the corresponding conductance (green dashed line). This confirms that the measured noise characteristics are a distinct fingerprint of the molecular system.

5.2 Noise characteristics of Au-BPY-Au single-molecule junctions

Using the previously described technique, I measured and analyzed 8000 Au-BPY-Au molecular traces to determine the conductance dependence of the relative noise of the molecular contact. During the analysis, for each time window that satisfied the stability criterion (the conductance ratio between the beginning and the end of the window is smaller than a factor of two), I calculated the integrated noise in the 2 – 5 kHz frequency band (highlighted in light blue in Figure 5.1(b)) from the noise spectrum. From this, the relative conductance noise was determined as: $\Delta G/G = \sqrt{\langle(\Delta G)^2\rangle}/\langle G\rangle$ where $\langle G\rangle$ represents the average conductance within the given window. It is important to note that, due to the specific nature of the temporal noise measurement technique, the PSD can only be calculated over short time windows. As a result, the frequency resolution of the spectrum is relatively low and the individual frequency components exhibit considerable variation. Although this does not hinder the evaluation of the noise measurements, it leads to significant scattering of individual data points. This limitation is addressed by applying a moving-window analysis, which acts as a moving average, combined with the statistical evaluation of a large number of molecular junctions. By calculating the $\Delta G/G$ for each window of each trace, we obtain several ten thousand pairs of ($\langle G\rangle$, $\Delta G/G$) values to statistically analyze. For the above reasons, the relative noise shows a broad scattering. To visualize the entire distribution, I calculated the 2D $\Delta G/G - \langle G\rangle$ histogram by defining bins (20 bins/decade) along the conductance and relative noise axis and counting the points that fall into each bin; see the resulting 2D histogram in Figure 5.2(c) with the 1D histogram in Figure 5.2(a) as reference. In this histogram, it can be observed that as the conductance decreases, the relative noise shows a slight increase. However, because of the broadening of the data points, resolving the average trends within the conductance range of different molecular configurations becomes challenging. To obtain the typical trend as a function of the conductance, we can take a vertical slice from the 2D histogram, i.e. the 1D histogram of the relative noise in a given conductance bin. This histogram exhibits a Gaussian profile along the logarithmic $\Delta G/G$ axis (see Figure 5.2(d)), from which the *most probable* $\Delta G/G$ value is identified by the peak position of the fitted Gaussian function (see the colored fitting curve in panel Figure 5.2(d)). The Gaussian fitting also enables the creation of a normalized 2D histogram of relative noise versus conductance, by fixing the offset and amplitude parameters of the fit for each slice to 0 and 1, respectively. This normalized histogram is shown in Figure 5.2(e), with the most probable $\Delta G/G$ values highlighted as a white line plot.

As shown in the previous chapters, based on the literature, in the HighG configuration

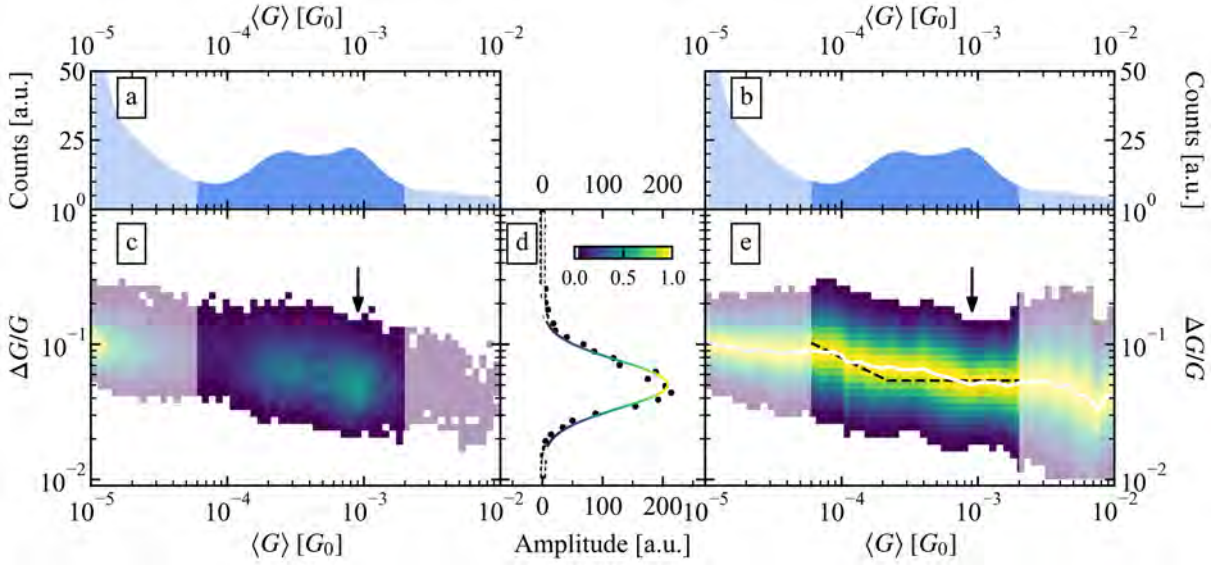


Figure 5.2: Analysis of the conductance dependence of relative conductance noise (a)-(b) 1D conductance histograms of the 8000 measured traces in the molecular and tunnel region. (c) 2D relative conductance noise – conductance histogram. Yellow colors corresponds to high counts, and dark blue colors corresponds to low counts. The arrow indicates the slice for which we take the count values and plot them as a function of the relative noise, to find the mean value by fitting a Gaussian function. (d) Gaussian fit of the indicated slice. The counts in the highlighted slice are plotted with black dots, and the colored line represents the Gaussian function fitted. To scale each Gaussian for comparison, the offset and amplitude parameters are fixed as 0 and 1, respectively; see the color scale of the Gaussian. (e) 2D relative conductance noise – conductance histogram normalized via Gaussian fitting. For each slice in the original 2D $\Delta G/G - \langle G \rangle$ histogram, the scaled Gaussian is then plotted as a colormap. The mean value is also plotted for each slice as a white line to see how the relative conductance noise scales with the conductance on average. The black dashed line is the expected scaling of the relative noise, based on the hypothesis explained in the main text. White shaded areas in (a)-(c) and (e) indicate conductance regions where the 1D histograms have a low count, where the Gaussian fits are not reliable; or the conductance is below $6 \cdot 10^{-5} G_0$, which is close to the instrumental noise level.

of the BPY molecule, the aromatic ring couples directly to the apex of the electrodes. In contrast, in the LowG configuration, the molecule is stretched between the electrodes and connected via its nitrogen linker groups. Based on this, one would expect that in the HighG configuration, charge transport through the aromatic ring involves a significant through-space contribution, whereas in the LowG configuration, transport is predominantly through-bond. These trends are also expected to be reflected in the conductance dependence of the relative noise. As a reference, this initial expectation is represented by the black dashed line in Figure 5.2(e). This line is the combination of the best fit-

Chapter 5. Temporal Noise Measurements on Au–BPY–Au Single-molecule Nanowires

ting $\Delta G/G \approx G^{-0.5}$ tendency at the low conductance and the $\Delta G/G \approx \text{const.}$ at the high conductance limits of the investigated conductance region extrapolated to the entire conductance range assuming a sharp transition at the intersection of these lines. By investigating the typical trend (white line in Figure 5.2(e)), we can conclude that the curve fits well with the expected trend at the edges of the conductance range and exhibits through-space-type $\Delta G/G \approx \text{const.}$ characteristics at the top tail of the HighG peak, and through-bond-type $\Delta G/G \approx G^{-0.5}$ characteristics at the bottom tail of the LowG peak. However, in the intermediate conductance region, a clear deviation from the supposed behavior can be observed. This intermediate conductance region lies near the boundary between the HighG and LowG configurations ($G \approx 4 \cdot 10^{-3} G_0$), where the molecular junction can evolve along a wide variety of possible pathways. As a result, interpreting the unexpected noise behavior is challenging, since the noise contributions from the different molecular configurations cannot be clearly distinguished.

Beside the integrated noise, I also studied the frequency dependence of the noise spectra as part of the analysis. For this, each acquired PSD was fitted by an $S_G \sim f^\gamma$ function within the 1 – 10 kHz frequency interval (see the blue lines in Figure 5.1(b) and the corresponding γ values). For the such obtained exponent values, I calculated the 2D $\gamma - \langle G \rangle$ histogram (Figure 5.3(c)) in the same way to that described earlier. Similar to the integrated noise, the fitted values also exhibit relatively large scattering, but the most probable exponent range can be identified. By using the previously demonstrated Gaussian fitting technique, we can construct the normalized 2D histogram which is plotted in Figure 5.3(e), the slice with the example Gaussian highlighted with a gray arrow. The color scale of the normalized histogram is the same as that of the Gaussian fit in Figure 5.3(d). The most probable γ value in a conductance bin is at the maximum of the fitted Gaussian (white line plotted in Figure 5.3(e)).

In the conductance range of the molecular peaks and above, the most probable value of γ is close to -1.4 (as highlighted by the orange dashed line) which was reported previously in the work of Adak et al., who found that at room temperature, the average noise power for tunnel junctions, gold point contacts, and the molecules studied, the noise power shows a frequency dependence $f^{-1.4}$ [29]. At lower conductances (toned down by the white shaded region), as we progress toward the tunnel region, where the junction is ruptured, the value of γ increases significantly, approaching zero, indicating that the PSDs become flatter in this region, which is in good agreement with the observation of instrumental noise as discussed above.

Based on the frequency analysis, it can be concluded that the molecular junction exhibits $1/f$ -type noise with an exponent consistent with values reported in the literature. Unlike the relative noise amplitude, no conductance dependence is observed in the frequency scaling. Across the entire molecular conductance range, the noise spectrum can be well characterized by an average exponent of approximately -1.4 .

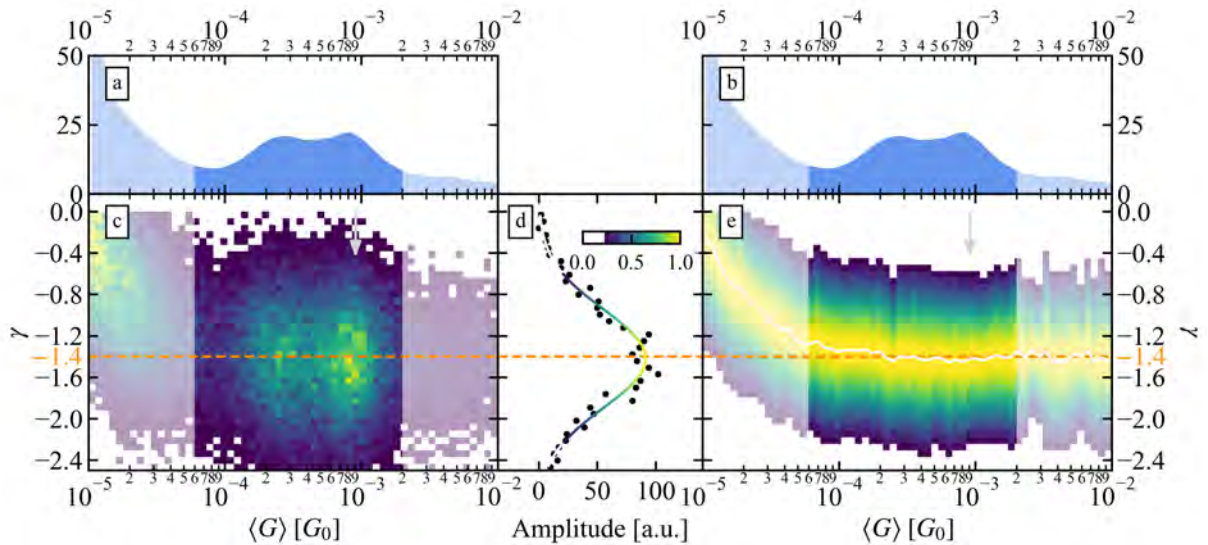


Figure 5.3: Distribution of γ exponent. (a)-(b) 1D conductance histograms of the 8000 measured traces in the molecular and tunnel region. (c) 2D γ -conductance histogram. The distribution of the exponent is visualized by same 2D color map as used for the relative noise. The white shaded region at $\langle G \rangle < 6 \cdot 10^{-5}$ is the region where the junction is already broken, and the tunnel current is measured. In this region, the prominent source of noise is the current amplifier. (d) Gaussian fit of the indicated slice. The counts in the highlighted slice are plotted with black dots, and the colored line represents the Gaussian function fitted. To scale each Gaussian for comparison in the normalized histogram, the offset and amplitude parameters are fixed as 0 and 1, respectively; see the color scale of the Gaussian. The color scale corresponds to that of the normalized 2D histogram in (e). (e) 2D slope-conductance histogram normalized via Gaussian fitting. For each slice of the original 2D γ - $\langle G \rangle$ histogram, the scaled Gaussian is plotted as a color map. To study how gamma scales with conductance on average, the mean value is plotted as a white line. The value of $\gamma = -1.4$ is highlighted for comparison with the literature. White shaded areas are the same as in Figure 5.2

5.3 EPCP-based trace selection technique

Previously, we have seen that in the intermediate conductance regime, where both the HighG and LowG configurations may occur with significant probability, an unexpected noise behavior was observed. To better understand this phenomenon, it would be beneficial to analyze the two molecular configurations separately, which requires categorizing the traces based on their conductance plateaus. In chapter 2, I introduced a PCA-based trace selection method that has the potential to perform such categorization: it can sort the traces into different groups based on the internal correlations within the system. More specifically, based on the correlation and principal component analysis of molecular junctions, we can identify the appropriate principal component that allows us to separate

Chapter 5. Temporal Noise Measurements on Au–BPY–Au Single-molecule Nanowires

molecular conductance traces of different characteristics. Ideally, this method can even form distinct groups corresponding to specific extrema, within which individual molecular configurations are separated.

To investigate whether the PCA-based trace selection could aid in understanding the observed noise phenomena. First, I determined the principal components of the dataset that I used for the temporal noise analysis of the Au–BPY–Au molecular junction. Then I analyzed their properties and tried to identify the principal component most suitable for separating the different molecular configurations.

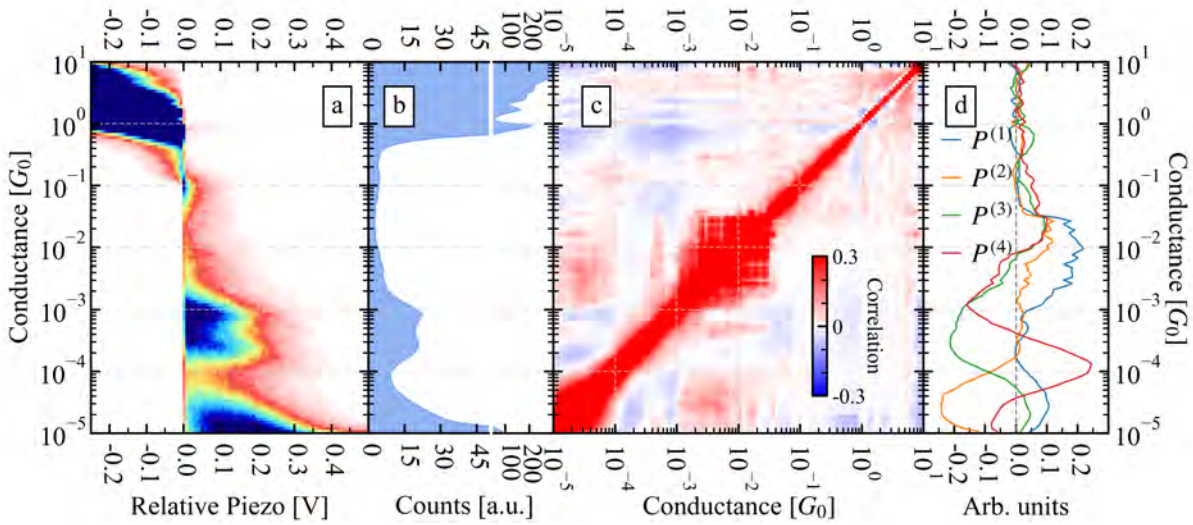


Figure 5.4: Statistical analysis of Au–BPY–Au dataset. (a)-(b) 2D conductance-displacement and 1D conductance histograms for all 8000 traces, respectively. Both the 2D and 1D histograms have 120 bins along the conductance axis (20 bins/decade). (c) Correlation matrix and (d) the first 4 principal components of the dataset.

Figure 5.4(c)-(d) show the 2D correlation histogram of the Au–BPY–Au dataset analyzed during the temporal noise measurements, and the first four principal components (i.e., the eigenvectors corresponding to the four largest eigenvalues of the correlation matrix). For reference, the 2D conductance-displacement histogram and the 1D conductance histogram are also shown in Figure 5.4(a)-(b). The correlation matrix exhibits a complex structure, whose interpretation requires considerable experience [34], however, this complexity can be reduced using principal components by focusing on the most significant correlations.

At this point, it is important to note that the correlation structure shown in Figure 5.4(c) differs somewhat from what is typically reported in the literature [34, P2, O1]. Instead of anti-correlation between the two molecular configurations (blue shades), the figure indicates statistical independence (pale or near-white shades). This is because, while in the literature the molecule typically binds in the nanogap in the HighG configu-

ration after the rupture of the single-atom contact, and the LowG configuration develops only upon further elongation, in my measurements both configurations can form immediately after the rupture of the single-atom contact. This can be seen in the histogram shown in Figure 5.4(a), where the conductance traces are aligned at the rupture point of the single-atom junction (0 V relative piezo voltage), and significant counts appear in the regions corresponding to both conductance peaks, even at small relative piezo values. This behavior resembles what has been observed in low-temperature measurements [46, O1]. A possible explanation is that during the temporal noise measurements, the very slow electrode separation, combined with high mechanical stability, increases the probability of forming highly stretched single-atom configurations or short atomic chains. Upon rupture of these configurations, nanogaps may form with a size favorable for the LowG configuration.

Now, let us analyze the principal components shown in Figure 5.4(d), focusing on the molecular conductance regime. The first and second principal components ($P^{(1)}$ and $P^{(2)}$, blue and orange line respectively) exhibit values close to zero throughout almost the entire range ($\sim 10^{-3} - 10^{-4} G_0$) with only slight deviations observed at the edges. This indicates that these two PCs are insensitive to this region. The third principal component ($P^{(3)}$, green line) significantly deviates from zero across the molecular region, but it is nearly constant, making it unsuitable for distinguishing between the two peaks. In contrast, the fourth principal component ($P^{(4)}$, red line) exhibits a more interesting pattern: it shows large positive and negative values within the molecular region, and the transition point (its zero-crossing) lies precisely between the two conductance peaks. This suggests that it may be suitable for differentiating between the two molecular configurations.

Further on, I investigate the trace groups separated by EPCP method (see chapter 2) using the fourth principal component. The separated two trace classes are demonstrated both by 2D conductance histograms (Figure 5.5(a)-(b)), and by 1D conductance histograms (Figure 5.5(c)). In the latter case, the light blue background histogram represents the reference histogram for the whole dataset, whereas the red and blue lines demonstrate the histograms of the two datasets obtained by the EPCP-based selection. In Figure 5.5(d) the principal component is demonstrated. Based on the 2D conductance–displacement histograms, it can be concluded that double-plateau traces (i.e., the simultaneous presence of both configurations within a single trace) are not characteristic of either group. This confirms the earlier assumption that this principal component is well-suited for separating the two molecular configurations.

5.4 EPCP-aided interpretation of single-molecule flicker noise measurements

I used the demonstrated EPCP-based selection method based on the fourth principal component ($P^{(4)}$) to separate the HighG and LowG configurations and investigate their individual noise characteristics. Figures 5.6(c) and 5.6(d) show the normalized 2D relative

Chapter 5. Temporal Noise Measurements on Au-BPY-Au Single-molecule Nanowires

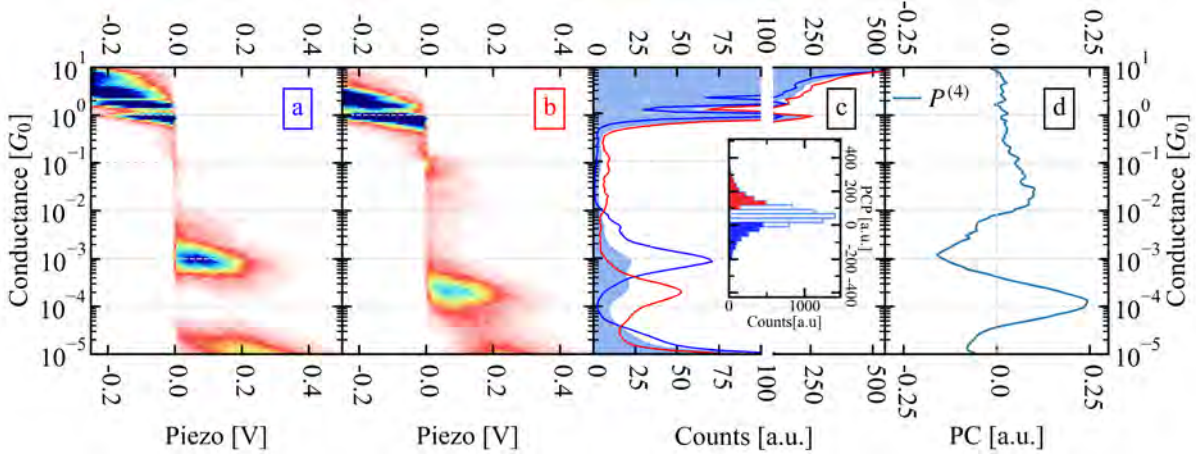


Figure 5.5: Histograms of trace groups selected via the EPCP method using $P^{(4)}$. (a)-(b) 2D histograms of 1600-1600 traces (20-20% of the total traces) sorted into group 1 and group 2, respectively. (c) Total 1D histogram of 8000 traces without selection (light blue area graph) and 1D histograms of traces from group 1 and 2, line plots with blue and red, respectively. The insets contain the histograms of the principal component projection values for $P^{(4)}$. The contributions of the traces in groups 1 and 2 are highlighted with blue and red, respectively. These are the selected 20-20% of all traces with extreme PCP values. (d) The principal component ($P^{(4)}$) used to sort the traces into group pairs.

noise-conductance histograms for the HighG and LowG subsets, each containing 1600 conductance traces. For reference, the corresponding 1D conductance histograms are replotted in Figures 5.6(a) and 5.6(b), with the corresponding subset histograms shown as area graphs. The most probable $\Delta G/G$ values were determined for each subset within the corresponding molecular peak region (indicated by blue and red lines in Figures 5.6(c) and 5.6(d), respectively), while other conductance ranges (white shaded regions) were excluded from the analysis.

Based on the literature, the HighG subset (blue) was anticipated to exhibit constant relative noise ($\Delta G/G \sim \text{const.}$), while the LowG subset (red) was expected to follow a $\Delta G/G \sim G^{-0.5}$ dependence. However, the experimental data do not support this distinction. Instead of the predicted differences in scaling behavior, both subsets show nearly identical trends: in the upper regions of the histogram peaks, the relative noise remains approximately constant, consistent with through-space transport, whereas the lower tails exhibit a $G^{-0.5}$ dependence, characteristic of through-bond transport.

For further analysis, the most probable relative noise curves for both configurations are plotted together in Figure 5.7(b), using the same color coding as before, along with the best-fitting model curves (orange and light blue lines) assuming constant and $G^{-0.5}$ noise behavior above and below a certain conductance threshold, respectively. As a reference, Figure 5.7(a) shows a replot of Figure 5.2(e), the normalized 2D relative noise-conductance histogram for the full dataset, with the most probable relative noise

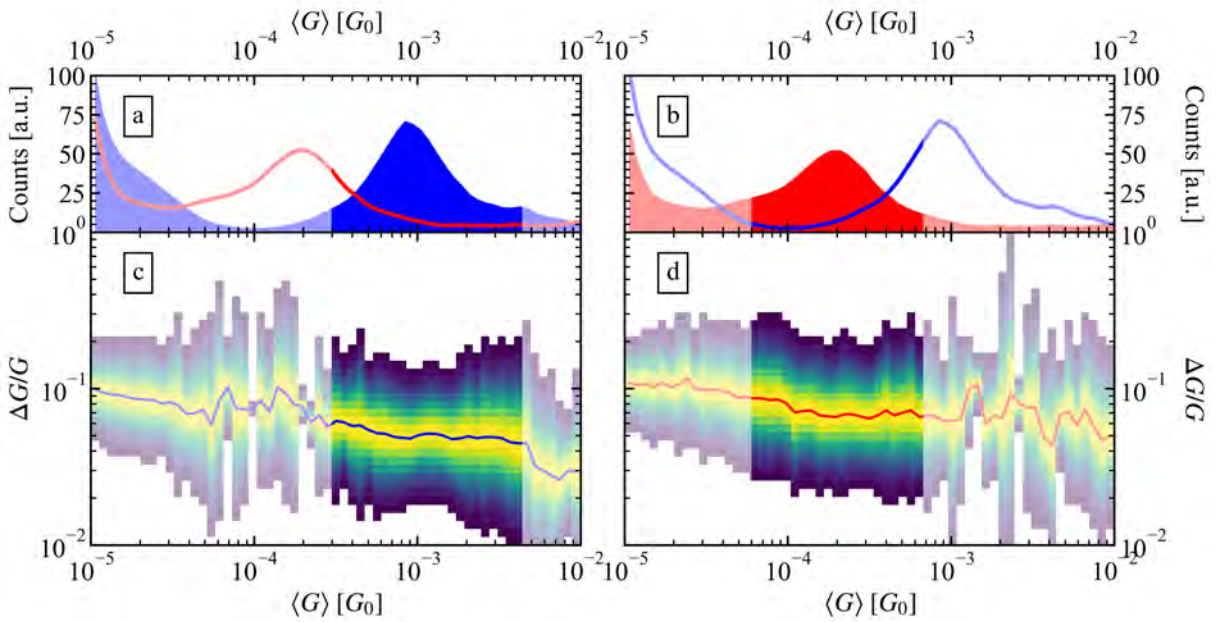


Figure 5.6: Relative noise analysis for HighG (blue) and LowG (red) class separately (a)-(b) 1D conductance histograms of HighG and LowG classes the area plots highlight the group for which the 2D histogram was calculated. (c)-(d) 2D relative conductance noise – conductance histogram normalized via Gaussian fitting. Lineplots represent the trend followed by the most probable $\Delta G/G$ value vs conductance. White shaded areas indicate conductance regions where the 1D histograms have a count less than half of the average count in a bin (i.e. the Gaussian fits are not reliable because there are not enough points for a good fit) or the conductance is below $6 \cdot 10^{-5} G_0$, which is close to the instrumental noise level.

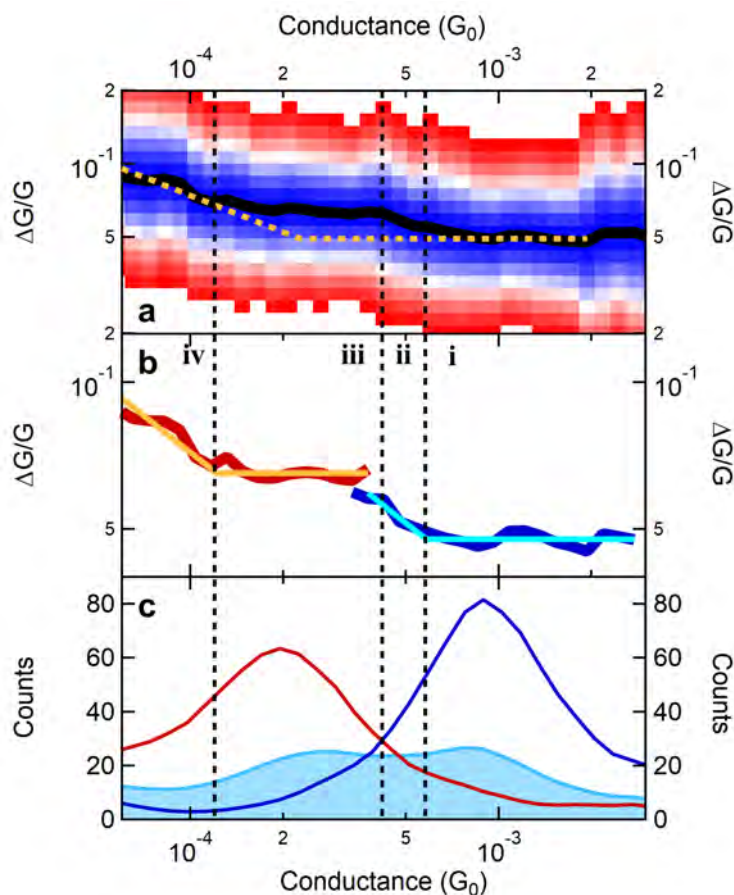


Figure 5.7: Configuration-specific $1/f$ -type noise analysis of Au-BPY-Au junctions. (a) Most probable relative conductance noise versus conductance for the entire dataset (black line). The color scale shows the spread of the noise data. The orange dashed line indicates the hypothetical noise evolution described in the text. (b) Configuration-specific noise analysis showing the noise behavior separately for the HighG (blue) and LowG (red) configurations. The light blue and orange lines are the best-fit model curves. (c) Conductance histogram for the full dataset (light blue area) along with configuration-specific EPCP projections (blue and red lines). Roman numerals and black dashed lines mark the four characteristic regions of junction evolution.

curve in black and the best fit based on the expected trend shown as an orange dashed line. Also for reference, Figure 5.7(c) displays the 1D histograms of the two selected subsets using the same color scheme, with the histogram of the full dataset shown in light blue in the background.

Comparing the noise trends of the two subsets (Figure 5.7(b)), the deviation from the expected behavior (constant noise in HighG and $G^{-0.5}$ scaling in LowG) is most pronounced in the intermediate conductance range. In this region, both the HighG and LowG subsets exhibit trends that are opposite to the initial hypothesis; specifically, the HighG configuration shows through-bond-like behavior, while the LowG configuration displays through-space-like characteristics.

To model the noise characteristics of a given configuration, we consider a simple model with two distinct scaling regimes: $\Delta G/G \sim G^{-0.5}$ and $\Delta G/G \sim G^0$, separated by a sharp transition. Based on the expected noise evolution from this model, four distinct conductance regimes can be identified in Figure 5.7(b) (marked with roman numerals and separated by dashed lines), with the following boundaries:

- The boundary between regimes i and ii is defined at the conductance value $G = 5.8 \cdot 10^{-4} G_0$, where the best-fitting noise trend (light blue) switches from constant to $\Delta G/G \sim G^{-0.5}$ behavior.
- The boundary between regimes ii and iii corresponds to the crossing point of the HighG and LowG histograms in Figure 5.7(c), at $G = 4.2 \cdot 10^{-4} G_0$.
- The boundary between regimes iii and iv is determined analogously to the i/ii boundary, based on the best-fitting curve (orange line) for the LowG subset.

Based on the evolution of the noise characteristics, the possible molecular configurations and molecule-electrode coupling types can be physically interpreted as follows:

- (i) **Top part of the HighG peak:** A constant, through-space-like noise trend is observed, consistent with the expectation in cases of significant π -coupling between the pyridine ring and the electrodes.
- (ii) **Bottom part of the HighG peak:** As the HighG configuration is stretched, the π -coupling between the pyridine ring and the electrodes weakens and disappears, leading to an increase in through-bond-type noise characteristics.
- (iii) **Top part of the LowG peak:** a significant constant, through-space noise contribution is observed again, suggesting that the pyridine ring could couple to the side of the electrode in this region again.
- (iv) **Bottom part of the LowG peak:** As the LowG configuration is stretched, the molecule straightens out, and increasing through-bond-type noise characteristics are again observed, indicating the disappearance of the π -coupling.

Chapter 5. Temporal Noise Measurements on Au–BPY–Au Single-molecule Nanowires

The detailed analysis presented above allowed us to gain a deeper understanding of the noise characteristics in cases where exclusively either the LowG or HighG configurations occur. With this understanding, we reexamine the noise evolution of the entire dataset shown in Figure 5.7(a). This dataset contains numerous traces where the two molecular configurations appear sequentially, but interestingly, the overall noise behavior mirrors the trends seen in the separated subsets, showing a through-space \rightarrow through-bond \rightarrow through-space \rightarrow through-bond transition across the four conductance regions (i–iv). This observation implies that the noise evolution above is not unique to the isolated subsets, rather a specific conductance interval; and the corresponding molecular configuration always shows similar noise evolution.

When the two configurations follow each other in the same trace, the following scenario is plausible: during elongation, the molecule is stretched first, then it jumps from one bonding site to another. This rearrangement likely causes the pyridine ring’s coupling to the electrode to weaken or strengthen alternately, resulting in the observed back-and-forth switching between through-space and through-bond noise behavior. It is also important to mention that the frequent occurrence of through-bond-type noise segments makes the presence of dimer configurations, such as those reported for DAF molecules in [30], unlikely in this system. Such dimer junctions would be expected to exhibit purely through-space noise characteristics, which contradicts our observations.

5.5 Conclusions

In this chapter, I demonstrated the successful implementation of the temporal noise measurement technique to investigate low-frequency noise in Au–BPY–Au single-molecule junctions. By applying this method to a dataset containing several thousand conductance traces, I examined the relative noise characteristics across a broad conductance range and compared them to theoretical expectations. In certain conductance regimes, the observed noise behavior aligned with the anticipated scaling laws, suggesting either through-bond or through-space charge transport. However, in the intermediate regime, corresponding to the transition between the two configurations of the BPY molecule (HighG and LowG), the noise characteristics deviated significantly from the expected trends.

To resolve this discrepancy, I applied a PCA-based trace classification (EPCP) method, which enabled the separation of conductance traces according to molecular configuration. This classification allowed for a configuration-specific analysis of noise, revealing that both the HighG and LowG configurations exhibit an internal evolution in noise behavior: starting with through-space-like characteristics at higher conductance values and gradually transitioning to through-bond-like behavior as the junction is elongated. This analysis suggests that the overall noise behavior of the full dataset may be related to a sequential reconfiguration of the molecule during elongation. Specifically, the molecule likely undergoes structural rearrangements in which the pyridine ring alternately strengthens and weakens its π -type coupling to the electrodes, producing the observed switching in noise

Chapter 5. Temporal Noise Measurements on Au–BPY–Au Single-molecule Nanowires

behavior.

Overall, my results demonstrate that the EPCP-based classification method works well to separate different junction evolution cases, helping us better understand the observed behaviors, especially when mixed junction paths make analysis difficult. Moreover, it also shows that low-frequency noise is a sensitive probe of molecular configuration and evolution in single-molecule junctions.

Chapter 5. Temporal Noise Measurements on Au-BPY-Au Single-molecule Nanowires

Chapter 6

Correlating Noise and Nonlinear Conductance Data in Real-time Controlled Break Junction Measurements

Conductance trace measurements by break junction (BJ) are the most common technique in the study of atomic and molecular junctions. These measurements supplemented with further advanced statistical analysis methods – such as 2D conductance electrode displacement histogram or conductance correlation histogram techniques, – the extracted information mostly provides the understanding of the structural behavior of the investigated system. However, if we want to gain more insight into the underlying physics of atomic or molecular junctions, further measurement techniques, such as $I(V)$ characteristic, noise, force, or thermopower measurements, are necessary. In order to perform these advanced measurements, the given configuration must be kept more or less stable for a sufficient period of time to complete the measurement. Furthermore, because of the randomness of the configurations, the measurements are typically repeated many times to allow meaningful statistical analysis.

In such measurements, the nature of conventional BJ measurements imposes a difficulty: in order to be able to stop the breaking process at a given conductance, i.e. given atomic or molecular configuration, we have to apply unconventional methods. One frequently used approach is when the elongation process is stopped at a fixed displacement position, where previous measurement results indicate that the configuration is formed with a high probability [29, 91, 92]. Another solution, which I also demonstrated in chapter 5, is when the elongation process is slowed down significantly, and during this slow breaking process, we can measure with a quasi-stable contact, or if the breaking is sufficiently slow, we can even stop at a given conductance in a controlled manner using a simple trigger [93].

In the first method, only a relatively small fraction of all measured data will correspond

Chapter 6. Correlating Noise and Nonlinear Conductance Data in Real-time Controlled Break Junction Measurements

to the target configurations, leading to less reliable statistics again or extremely long measurement time, while the second method leads to increased measurement times and requires very high mechanical stability, which can be reached rather in lithography MCBJ measurements, and it leads to a decreased amount of measured traces and less reliable statistics.

Another approach, demonstrated in chapter 4, involves performing measurements in a cryogenic environment, which provides high mechanical stability and precise motion control. This allows for manual fine-tuning of molecular configurations and enables measurements that even take several minutes to be performed. However, this method requires special measurement equipment, such as helium dewar and cryogenic sample holder, making it significantly more complex than room-temperature measurements. Furthermore, temperature itself can affect the physical behavior of the system, meaning that cryogenic measurements cannot completely replace those conducted at room temperature.

To resolve the above issues, our group's aim was to perform BJ measurements at room temperature, in a controlled way, without compromising the elongation speed or the reliability of the statistics.

6.1 Real-time controlled break junction measurements

As introduced in chapter 3, András Magyarkuti developed an FPGA-based system that enables *real-time control* of the measurements [41]. This allows us to perform experiments in which the opening/closing process of a BJ measurement is reliably stopped based on a condition, e.g. when a predefined conductance value is reached. In a molecular measurement, this could be a conductance value that corresponds to a distinct configuration, but in a tunnel junction, we can stop anywhere in the tunneling conductance region to study the underlying conduction mechanism. The flow of the measurement was introduced in section 3.4 and illustrated in Figure 3.9. To summarize, these measurements consist of 2 parts: one is the simple *BJ part*, when the junction is actively elongated/compressed; the second is the *hold part*, when the junction is held stable (see Figure 3.9). I tested this system with simple measurement schemes (the bias signal in the hold part is a simple constant signal, as shown in Figure 3.9) to more complex (combined $I(V)$ characteristics and noise measurements) ones. I made measurements at room temperature and under ambient conditions. In the following sections, I show the stability analysis of hold measurements, where I studied how close to the set trigger value the measurement control system can stop the movement of the electrodes and also how stable the hold measurements are. Then, I proceed with the discussion of more complex measurements, where I combined current-voltage characteristics measurements with noise analysis and complemented the measurements with simulations performed by Zoltán Balogh.

6.2 Stability analysis of hold measurements

To test the stability and the measurement control, I chose the gold tunnel junction, which is ideal for benchmarking, because unlike atomic or molecular configurations that show plateaus and their conductance is therefore less sensitive to changes in electrode separation, the conductance of a tunnel junction changes exponentially with electrode separation. A small change in the electrode separation can cause large changes in conductance (in vacuum conditions, if the electrode separation increases by 1 Å, the conductance decreases an order of magnitude), making it highly sensitive to instabilities.

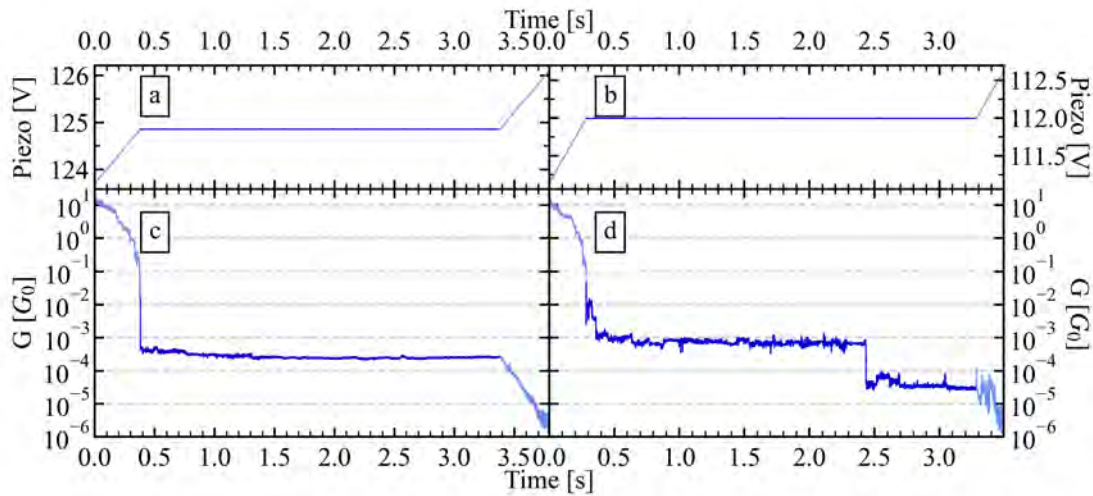


Figure 6.1: Analysis of tunnel hold measurement stability. (a)-(b) Applied piezo voltage during the opening–hold–opening cycle. When the voltage applied to the piezo actuator changes linearly (light blue portions), the electrodes move further from each other. When the piezo voltage is constant (dark blue), the electrodes stop and are held stable. **(c)-(d) Measured conductance during the opening–hold–opening cycle.** Light and dark blue colors correspond to the opening BJ parts and the hold part, respectively.

Typical BJ conductance traces of such a clean gold wire measured at a 100 mV applied bias voltage are shown in Figure 6.1(c)-(d). The trigger value for stopping the movement of the electrodes was $10^{-2} G_0$ and the bias signal was a 3 s long constant 100 mV signal during the hold part. The long plateau visible in the opening traces is a clear consequence of the interruption of the opening process. For analysis, these traces are separated into two parts, as described above. One where the piezo voltage changes linearly (see Figure 6.1(a)-(b)): the electrodes are moving (light blue portions at the beginning and end); and one where the piezo voltage is constant: the electrodes are held still (dark blue portion in the middle). We use the former to perform conventional statistical analysis (with tools such as the 1D conductance histograms) while the latter can be used for more advanced analysis (like noise analysis).

Chapter 6. Correlating Noise and Nonlinear Conductance Data in Real-time Controlled Break Junction Measurements

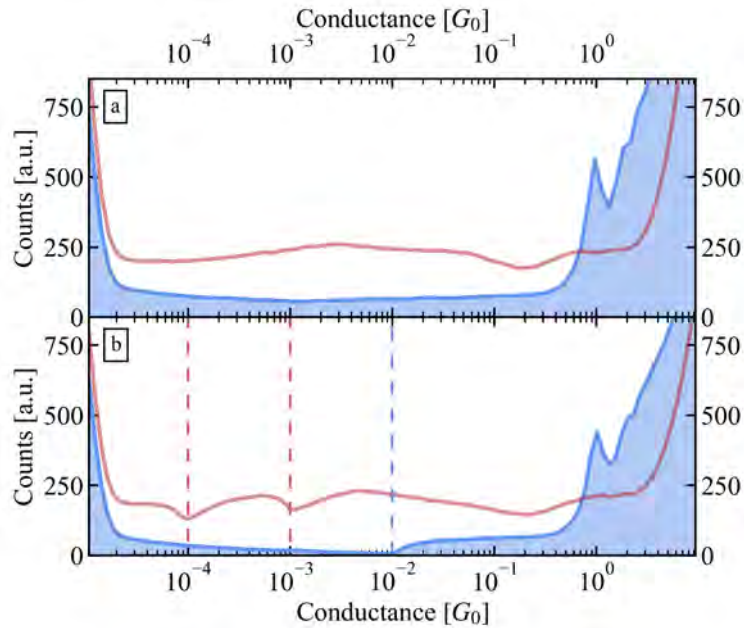


Figure 6.2: Comparison of the 1D histograms (a) without and (b) with hold measurement. Opening histograms are displayed as light blue area plots, while the light red line plots are the closing histograms. The 1D histograms in (a) are calculated for 8000 traces, while the histograms in (b) are calculated for a total of 15000 traces. The trigger conductance values are marked with vertical dashed lines in (b), $10^{-2} G_0$ for the opening and $10^{-4} G_0$ (9000 traces), $10^{-3} G_0$ (6000 traces) for the closing traces.

In both Figures 6.1(c) and 6.1(d), the hold portion starts at a conductance fairly close to the set trigger value. In Figure 6.1(c), the conductance is constant throughout most of the hold interval, but looking closer at the beginning, a sudden conductance change is visible right at the beginning. There is a similar conductance change at the beginning of the hold trace in Figure 6.1(d), but it is followed by a second one later on. Before and after this jump in conductance, the hold trace shows plateau-like characteristics. In both of these examples, the last conductance point before and the first conductance point after the hold portion differ significantly, due to the changes in conductance during the hold portion of the measurement. If we calculate the 1D conductance histograms (shown in Figure 6.2(b) with a light blue area plot) that is commonly the first step in the analysis of BJ measurements, we see a large dip in the counts at the trigger conductance value on the 1D histogram. Similar dips at the set trigger values are observed for the closing histogram too (red curve in Figure 6.2(b)), where two different set trigger values were used during the measurement, $10^{-3} G_0$ and $10^{-4} G_0$. Due to the conductance changes during the hold portion of the measurement, the 1D histograms differ significantly compared to those without hold measurements (see Figure 6.2(a)), and they cause artificial peaks in the 1D histograms, making it difficult – or in extreme cases impossible – to use the 1D or 2D histograms. Considering that these usually serve as the *fingerprint* of the studied

Chapter 6. Correlating Noise and Nonlinear Conductance Data in Real-time Controlled Break Junction Measurements

system, if we cannot use them to identify or check the system, the measurement becomes a *black box*.

The observations detailed above lead to the conclusion that in a measurement series with hold portions, it is important to interlace measurements without hold portions that enable the application of conventional statistical methods to characterize the studied system. These traces can be used to check the presence of the target molecule in molecular measurements or the purity of the system when studying clean metallic nanogaps. So in the following, I carry out the measurements so that each measurement period with hold portion (usually consisting of a few thousand traces) is followed by at least 1000 simple BJ curves without hold, to check the characteristics of the contact.

If we examine Figure 6.2(b) further, we can see that the dips in the histograms are relatively narrow, indicating that conductance change (i.e. the instability) is not substantial on average. To investigate the stability during the hold measurement in detail, I compared the conductance values before and after the hold segment by calculating 2D histograms of the last point before and the first point after the hold portion for the opening and closing directions (see Figures 6.3(d) and 6.3(e)). I also plotted the 1D histograms of both values, which are just the projections of the 2D histograms (Figures 6.3(a) and 6.3(b) for the before and Figures 6.3(c) and 6.3(f) for the after hold points).

The 2D histograms are spread out, especially the one for the opening process. The horizontal spread shows how well the measurement control performs in stopping at the set trigger conductance, while the vertical spread describes the stability of the hold portion. For the closing process, the horizontal spread is small on the 2D histogram, the 1D histogram of the last point before the hold measurement exhibits sharp peaks close to the set trigger values ($10^{-3} G_0$, $10^{-4} G_0$) suggesting that the electrode displacement was successfully stopped when the trigger conductance was reached. This is also true for the opening process; the somewhat larger horizontal spread on the 2D histogram and the tail on the 1D histogram below the trigger value ($10^{-2} G_0$) can be explained by the snapback effect (i.e. large gap opening after the rupture of the single atom junction) [13, 94].

Compared to the sharp peaks in the before histogram, the peaks in the after histogram are widened (especially in the opening process) and shifted depending on the direction of the movement. When stopping during the opening process, the peak is shifted toward lower conductance, and in some cases, the conductance even drops to the instrumental noise level during the hold portion. In the closing process, the shift is less obvious: statistically, the peaks shift toward higher conductance, and despite the junctions being more relaxed and therefore more stable, in some cases the conductance still drops close to the instrumental noise level. These observations indicate that the FPGA-controlled system is very efficient in the detection and fast reaction to the trigger. However, once the movement of the opening/closing process is stopped, we have no control over the atomic-scale processes in the junction.

Chapter 6. Correlating Noise and Nonlinear Conductance Data in Real-time Controlled Break Junction Measurements

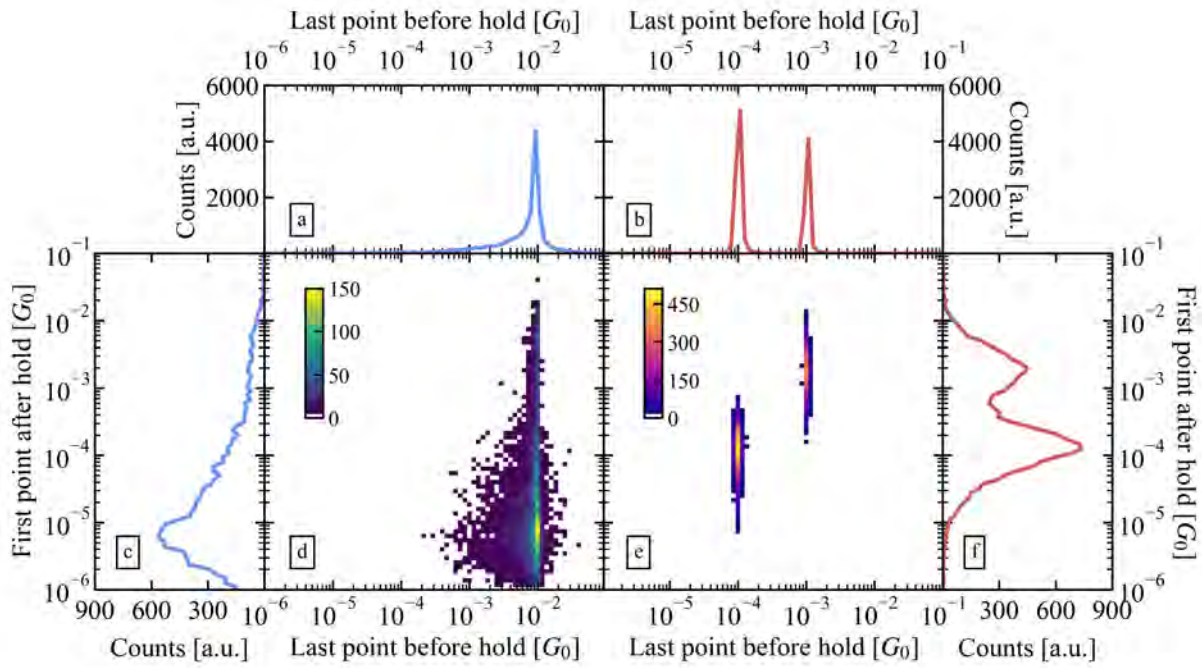


Figure 6.3: Comparison of the conductances before and after the hold portion (a)-(b) 1D histograms of the of the last point before the hold portion, when the the movement of the electrodes is stopped. The peaks are sharp around the trigger conductance, verifying the reaction time of the system. (c)-(f) 1D histograms of the first point after the hold portion, when the movement of the electrodes continues. The widened peaks indicate that even though the stopping happens fast, the stability of the junction depends on other facts that are not so easy to manage. (d)-(e) 2D histograms of the distribution of the last and first conductances.

6.3 Relaxation phenomena in gold tunnel junctions

The hold curve in Figure 6.1(c) shows another important phenomenon of the hold measurements: even though the conductance changes suddenly in the short period at the beginning of the hold portion, as in the example plotted, it may be followed by a period with stable conductance that is a few seconds long. To study how significant this phenomenon is, I created the 2D stability histograms shown in Figure 6.4. I used the 9000 traces where the opening (closing) trigger was set to $10^{-4} G_0$ ($10^{-4} G_0$) and separately filtered the opening and closing traces to only keep those where the conductance does not drop below the $10^{-5} G_0$ base line. This selection left 2988 opening and 8511 closing traces. Then, I used the conductance value at the very last point of the hold portion and normalized each hold trace by dividing the conductance values by this value. From these normalized traces, I made a 2D histogram with the normalized conductance along the vertical and the time passed from the start of the hold portion along the horizontal axis. The 2D stability histograms of the opening and closing traces are shown in Figures 6.4(a) and 6.4(c), respectively, while Figures 6.4(b) and 6.4(d) show the 1D histograms of the cross section at the vertical dashed lines with the corresponding colors.

Let us first consider the 2D histogram during the opening process. It is clearly visible that looking backward in time from the end of the hold segment (3 s), there is a long period of high hit counts around the normalized conductance value of $G_{\text{norm}} = 1$, extending to approximately the 0.5 s range. This means that the change in conductance during the hold segment is typically limited to the first few 100 ms of the segment. After this so-called *relaxation phase*, the established state remains stable for several seconds. This is also clearly shown by the 1D cross-section histograms: the light blue histogram taken at the end of the hold segment is very sharp, with minimal broadening (this can partly come from minimal instability and partly from the noise of the curve). The blue histogram taken at 1.5 s (in the middle of the hold segment) already shows some broadening, but the peak position is clearly at the normalized conductance of $G_{\text{norm}} = 1$, with a significant portion of the points (72% and 84% for the opening and closing processes, respectively) located between the lines representing a factor of two relative to this (horizontal dashed gray lines). In contrast, the dark blue histogram created for the beginning of the hold segment gives a very smeared peak with a significantly upward-shifted position.

This effect is also observed during the closing process but is much less pronounced. The blue band representing high hit counts extends almost to the beginning of the hold segment, only fading and showing some deviation toward lower conductances in the first few 10 ms range. The 1D cross-section histograms (light red) taken at the end of the hold segment and at 1.5 s are very similar to what was seen during the opening process. However, here, the dark red 1D histogram created at the beginning of the hold segment also shows a distinct peak at a somewhat lower conductance with greater broadening.

The relaxation period observed for the opening process can be explained by the contact being stretched, so after the rupture and the detection of the trigger value that stops the elongation, the size of the nanogap formed (i.e. the distance between the electrodes)

Chapter 6. Correlating Noise and Nonlinear Conductance Data in Real-time Controlled Break Junction Measurements

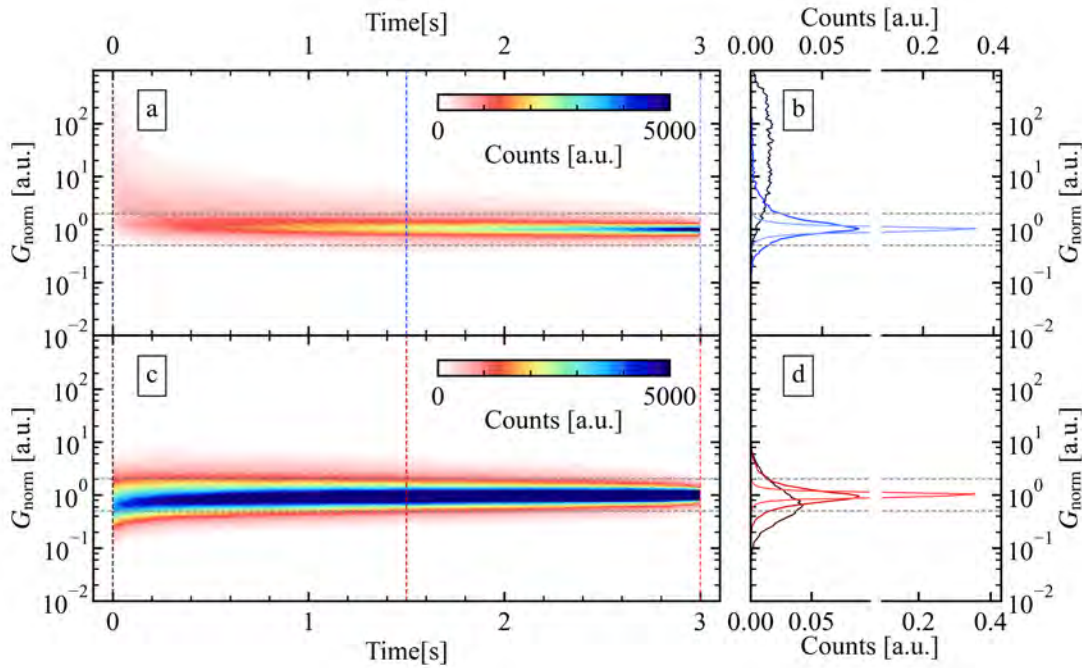


Figure 6.4: Stability of tunnel junction. (a)-(c) 2D stability histograms of the opening and closing traces, respectively. The histograms are calculated from 2988 opening traces and 8511 closing traces. The hold portion lasts 3 s, which means 150000 points with the sampling rate of 50 kHz. For the calculation of the 2D histogram, I used 150 bins (30 bins/decade) along the vertical and 15000 bins along the horizontal axis. Horizontal dashed light gray lines are placed at the normalized conductance values of 2 and 0.5 enclosing the parts of the histograms where the conductance does not change more than a factor of 2. (b)-(d) 1D cross section histograms. The colors (dark blue–blue–light blue and dark red–red–light red, respectively) correspond to the vertical dashed lines at the beginning, middle and end in (a) and (c). Horizontal dashed gray lines are the same as in (a) and (c).

still changes because of the relaxation of the mechanical strain. Following the relaxation period, the contact remains stable. In the closing process, the system is already in a fully relaxed state, so large conductance changes are not observed. The small shift in conductance might be attributed to the mechanical inertia of the measurement system: even though the system reacts fast to the detection of the trigger value, the full stop of the electrode movement happens later. However, this only means a small change in distance, the total spreading of the peak in the 1D histogram is limited to approximately ± 1 order of magnitude, which corresponds to ± 1 Å maximal change in distance, but the characteristic change is a fraction of that. Comparison of the 1D histograms calculated at 1.5 s for the opening and closing histograms reveals that, in the middle of the hold portion (after the relaxation process took place), the contact shows similar stability in both cases, and the broadening of the 1D histograms is similar.

Chapter 6. Correlating Noise and Nonlinear Conductance Data in Real-time Controlled Break Junction Measurements

Based on the above observations, we can draw the following technical conclusions:

- Detailed analysis showed that it is possible to achieve a stable contact during the hold segment for several seconds in both the opening and closing processes.
- The relaxation observed during the opening process can be a few 100 ms long. Therefore, measurements requiring stability should typically start only after this time has passed. The bias signal used for the hold measurements should be defined accordingly.
- The hold measurements during the opening and closing processes are useful for different purposes. On the one hand, the conductance during closing can be tuned to be close to the desired trigger level; on the other hand, the actual conductance value (configuration) during hold measurement in the opening process is more dependent on the self-assembly of the contact.

The above findings enable a more controlled execution of hold measurements and are also valid for molecular contacts, while taking their specific characteristics into account.

6.4 Investigation of noise phenomena in gold tunnel junctions using combined $I(V)$ characteristics and noise measurements

So far, the drive during the hold segment has been a simple constant bias voltage. Although this was ideal for studying stability and relaxation, it hardly takes full advantage of the capabilities of the measurement system.

In previous chapters, we saw that noise measurements, specifically the examination of $1/f$ -type noise, can provide deeper insights into the conduction and bonding mechanisms, as well as other properties of atomic and molecular contacts. For technical reasons, those noise measurements were performed over a relatively short duration and at a constant voltage. This was adequate for basic investigations, but severely limited more complex noise diagnostics [P3, 71, 95].

My goal was to test the capabilities of the FPGA-based real-time measurement system by performing and evaluating measurements similar to the complex noise diagnostics on graphene nanogaps presented in the publication by Pósa et al. [71]. In that publication, the resistance dependence of the relative current noise of graphene nanogaps was complemented by numerical simulations, which required both noise and $I(V)$ characteristic measurements.

In the following sections, I will present the implementation and results of the measurements inspired by the publication by Pósa et al. [71], performed on a gold nanogap (tunnel junction).

Chapter 6. Correlating Noise and Nonlinear Conductance Data in Real-time Controlled Break Junction Measurements

6.4.1 The scheme of combined $I(V)$ characteristics and noise measurements

When conducting noise measurements, two important aspects must be considered regarding the waveform of the applied bias:

- (i) Longer stable segments are desirable for calculating spectra as they allow for better frequency resolution and a higher number of averages.
- (ii) In addition to measurements with a driving voltage, it is advisable to perform measurements with zero voltage. This allows for the determination of the system's thermal noise and/or instrumental background. Subtracting this from the measurements with nonzero bias provides a precise calculation of the excess noise, such as $1/f$ -type noise.

Furthermore, the fixed voltage plateaus used for noise measurements should be supplemented with $I(V)$ characteristic measurements to be used to characterize the specific configuration with the help of numerical simulations. Following these considerations, I defined the complex waveform shown in Figure 3.11, where the applied bias waveform consists of plateaus at distinct bias voltages and a triangular signal to measure the $I(V)$ curve. The plateaus are used for the statistical analysis of noise as seen in chapter 5. However, now, instead of analyzing short static regions in the break junction curve of the slowly elongated junction, the junction is held stable while the bias signal is applied. I demonstrate this combined measurement in Figure 6.5.

Both the opening and closing sequences are interrupted when the given trigger conductance is reached. I plotted one of the opening (light blue) – closing (pale red) trace pairs in Figure 6.5(a), and highlighted the trigger conductance values by dashed-dotted lines with the corresponding color. The applied bias signal, consisting four main sections, is shown in Figure 6.5(b) with a darker blue color: the signal starts and ends with 200 mV bias plateaus, which are used to investigate the $1/f$ -type noise and check the stability of the hold measurement, while the middle part of the signal consists of a triangle signal with an amplitude of 700 mV, followed by a 0 mV. The latter is used to determine the thermal/instrumental noise floor. The measured current through the junction during the hold period of the closing process is plotted in dark red in Figure 6.5(b), and for further evaluation, it is divided into four sections according to the bias signal: one for each plateau and one for the $I(V)$ curve (see Figure 6.5(c)). The analysis of the plateaus is similar to that of the small intervals in chapter 5, however, as the plateaus are longer, they are further divided into smaller segments (see the colored regions divided by vertical dashed lines) and the power spectral densities (PSDs) are calculated for each segment and then averaged to have a smoother PSD (see Figure 6.5(d)).

Chapter 6. Correlating Noise and Nonlinear Conductance Data in Real-time Controlled Break Junction Measurements

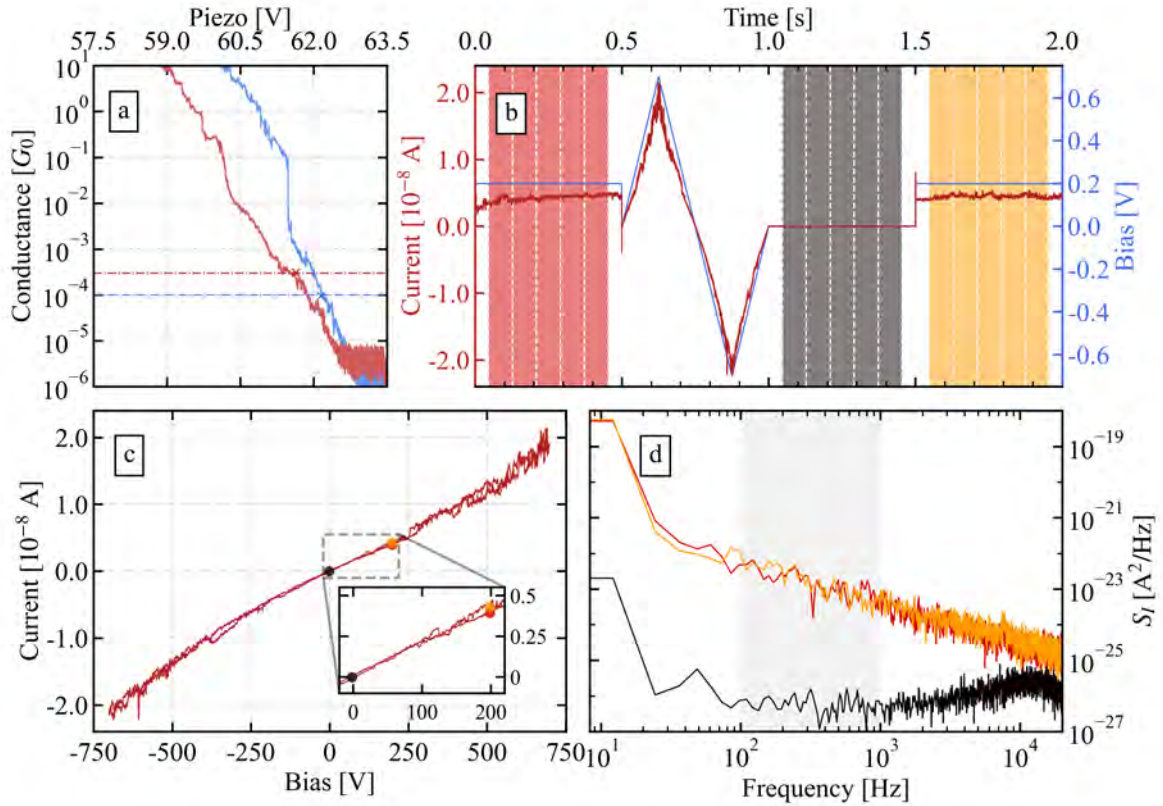


Figure 6.5: Hold measurement with current-voltage characteristics. (a) Opening (light blue) and closing (pale red) break-junction trace pair for the given hold measurement. The dashed-dotted line indicates the trigger conductance values, while the stopping point in the trace is emphasized with an \times on each trace. (b) Combined noise and $I(V)$ characteristics measurement. The $I(V)$ -curve is extracted and plotted in (c). (c) The extracted $I(V)$ curve with the dots corresponding to the average current at the bias value of each plateau. In the inset, the denoted region is zoomed in to show that the average conductances of the two 200 mV plateaus are close and overlap with the $I(V)$ curve. (d) Power spectral density plots for each plateau in (b), calculated for the plateau intervals highlighted with colored regions. Each power spectral density is calculated by averaging 5 subintervals divided by white dotted lines. The PSDs for the 200 mV plateau before and after of the $I(V)$ measurement overlap and separate from the noise floor calculated for the 0 mV plateau, which amounts to the sum of the thermal and instrumental noise.

6.4.2 Conductance dependence of relative fluctuation

Using the waveform presented previously, I investigated the conductance dependence of the relative noise of a gold tunnel junction. To achieve this, I performed hold measurements on a total of 29500 opening–closing trace pairs by setting a range of trigger conductances. To ensure high-quality data for statistical analysis, the 29500 measured

Chapter 6. Correlating Noise and Nonlinear Conductance Data in Real-time Controlled Break Junction Measurements

traces were filtered by selecting those that meet the following stability criteria:

Condition 1: the conductance did not decrease below $10^{-5} G_0$ (i.e. the conductance floor set by instrumental limitation) during the measurement;

Condition 2: the two 200 mV plateaus are compared, and only those traces are selected, where the two mean conductance values do not differ more than a factor of 2;

Condition 3: the branches of the $I(V)$ curves overlap (i.e. the mean squared deviation between the branches is smaller than a threshold, determined based on manual selection of representative curves).

	Condition 1	Condition 2	Condition 3
Opening	12880	8127	2514
Closing	21335	21053	6219

Table 6.1: Number of traces after each filter condition is checked from the total number of traces (29500).

The number of traces selected after each condition is applied sequentially is collected in Table 6.1. As expected, a higher percentage of the opening traces rupture or the plateaus are at different conductances, which can be attributed to the relaxation explained in the previous section.

The relative noise is calculated using Equation 2.11: I numerically integrated the measured PSD curves with or without driving bias voltage over the frequency range between 100 Hz–1 kHz, as indicated with a light gray background in Figure 6.5(d). From the values measured under bias, I subtracted the integrated value of the baseline noise measured at 0 mV and normalized this by the average conductance. The results are displayed on 2D histograms, in both raw and normalized forms (after Gaussian fitting) as applied in chapter 5, for both the opening and closing processes (see Figure 6.6). To avoid the effect of relaxation, we selected the second plateau in the opening process and proceeded similarly in the case of the closing process.

In the 2D histograms without normalization (Figures 6.6(a) and 6.6(c)), it is clearly visible that the density of points is higher at the trigger values. This shows that the previous observations are also valid here, and that during the closing process, we can investigate the desired conductance and we need to apply several set points to cover the studied conductance range. In contrast, during the opening, the relaxation ensures that the studied conductance range can be almost continuously covered with a same number of set trigger values.

Chapter 6. Correlating Noise and Nonlinear Conductance Data in Real-time Controlled Break Junction Measurements

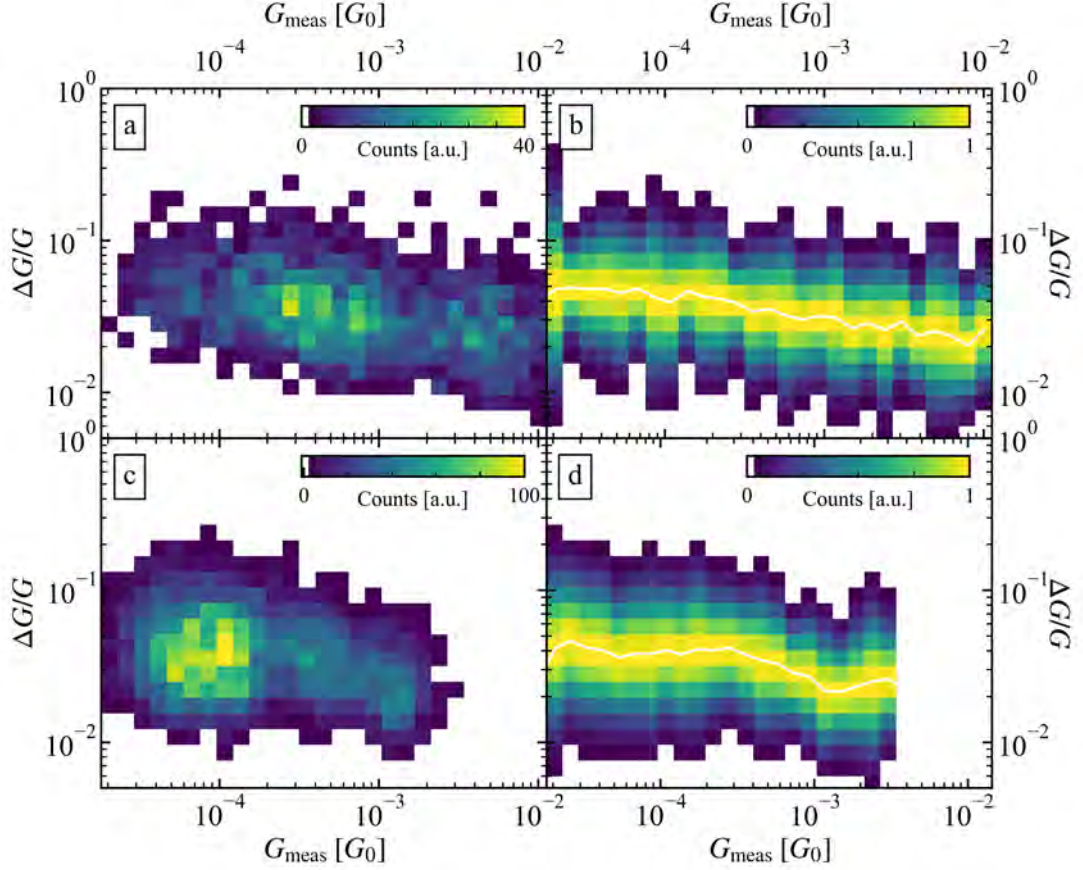


Figure 6.6: Relative noise distributions for the second plateau of opening and closing traces *The histograms are calculated for 2508 (opening) and 6181 (closing) traces. (a)-(b) ((c)-(d)) 2D histogram and normalized histogram for the 2nd 200 mV plateau during the opening (closing). The normalized histograms are calculated with Gaussian fitting as introduced in chapter 5 and explained in Figure 5.2. The white lines in (b)-(d) follow the peaks of the fitted Gaussian functions fitted to the vertical bins of the 2D relative histogram, and represent the mean conductance dependence of the relative noise. The set trigger values are $10^{-4} G_0$, $5 \cdot 10^{-4} G_0$, $10^{-3} G_0$, $5 \cdot 10^{-3} G_0$, $10^{-2} G_0$ for opening ($5 \cdot 10^{-5} G_0$, $10^{-4} G_0$, $3 \cdot 10^{-4} G_0$, $10^{-3} G_0$ for closing).*

In the normalized 2D histograms (Figures 6.6(b) and 6.6(d)), following the white line (the most probable relative noise at a given conductance), it is clear that the relative noise increases slightly as the conductance decreases.

Similarly to graphene nanogaps, transport through gold tunnel junctions is well described by the Simmons model [15, 82, 96, 97] which relies on two key parameters: the Φ height and the d length of the tunneling barrier between the two gold electrodes. To understand the noise trend observed in Figures 6.6(b) and 6.6(d) within the framework of this model, we performed numerical simulations and fitted the simulation data to our

Chapter 6. Correlating Noise and Nonlinear Conductance Data in Real-time Controlled Break Junction Measurements

experimental data.

6.4.3 Fitting of measured $I(V)$ curves and calculation of simulated noise using numerically evaluated Simmons model

The evaluation of the simulation consists of 3 main steps:

Step 1: the measured $I(V)$ curves are fitted using a numerically evaluated Simmons model, to gather the conductance ($G_{\text{sim},r}$) (resistance $R_{\text{sim},r}$), the gap size (d_r) and barrier height (ϕ_r) for each investigated configuration (denoted by r).

Step 2: Using the values $G_{\text{sim},r}$, d_r , ϕ_r obtained from the simulation, we determine the simulated relative noise for each investigated conductance state, considering various barrier length (gap size) and barrier height fluctuation amplitudes (Δd and $\Delta\phi$, respectively).

Step 3: We compare the measured relative noise – conductance dataset with those calculated from different pairs of Δd and $\Delta\phi$ values from the simulation and determine the Δd and $\Delta\phi$ pair best describing the measurements.

The simulation code for the first step was developed in MATLAB by László Pósa and introduced in [71]. In the case of the gold tunnel junctions, the same code was applied to the data set that I measured and prepared. Then I used the simulation results to complete the analysis with steps 2 and 3. In the following, I will focus on presenting my own contributions and interpreting the results. The operation of the simulation code will be described only to the extent necessary to understand my contributions. More detailed information on the simulation can be found in the publication [71] and its associated ESI.

Unlike graphene nanogaps created by nanofabrication, gold nanogaps produced with the break junction technique are highly susceptible to mechanical instability. This can cause random jumps in certain sections of the $I(V)$ curve, even if the contact appears stable based on the hold segments used for noise measurement. These significant jumps can easily corrupt the simulation results.

To ensure suitable data for the simulations, I developed a filtering procedure (referred to above as Condition 3). The essence of this method is to compare the corresponding segments of the $I(V)$ curve (the positive up-down sweep and the negative up-down sweep). For curves without jumps, the segments should overlap well. In contrast, instability-induced jumps result in non-overlapping curves due to their randomness.

To quantify the overlap, I used the normalized squared difference between the two segments as a metric. I manually selected a number of overlapping and non-overlapping curves from the full dataset and, based on a histogram of the normalized squared differences, I determined a threshold value. Any curve with a value below this threshold is considered to overlap and thus satisfies Condition 3. The necessity of this filtering criterion is clearly shown in Table 6.1, which indicates that only about 30% of the curves considered stable by Conditions 1 and 2 also meet Condition 3.

Chapter 6. Correlating Noise and Nonlinear Conductance Data in Real-time Controlled Break Junction Measurements

It is important to note that the possibility of applying such strict filtering criteria is made available by the FPGA-based real-time measurement system. Because this system can achieve the desired conductances with a near 100% success rate, a large number of measured curves are available. This allows for critical selection, ensuring that even after discarding a significant portion of the data, a sufficient quantity remains for detailed statistical analysis.

For the analysis of the $I(V)$ curves obtained after the previously described preparation (filtering) procedure, each curve is divided into four segments: i) from 0 mV to 700 mV, ii) from 700 mV to 0 mV, iii) from 0 mV to -700 mV, iv) from -700 mV to 0 mV. These segments are individually fitted, but it is important to note that the model is symmetric. The linear resistance (then the conductance) is determined by linear fitting the low bias voltage range up to $|150|$ mV. The simulation script uses a set of previously generated simulated $I(V)$ curves, with gap and barrier values from a parameter matrix, using increments of 0.001 nm and 0.01 eV, respectively. The segments of the measured $I(V)$ curve are compared to each simulated $I(V)$ curve, and the closest is accepted (where the least squares difference is lowest). Figure 6.7 shows two examples in which the measured $I(V)$ curves are plotted with a red line, and the $I(V)$ curve fitted based on the simulation is shown with a black line. The insets show the gap size, barrier height, and conductance values derived from the simulated curve, which best describe the measured $I(V)$ curve.

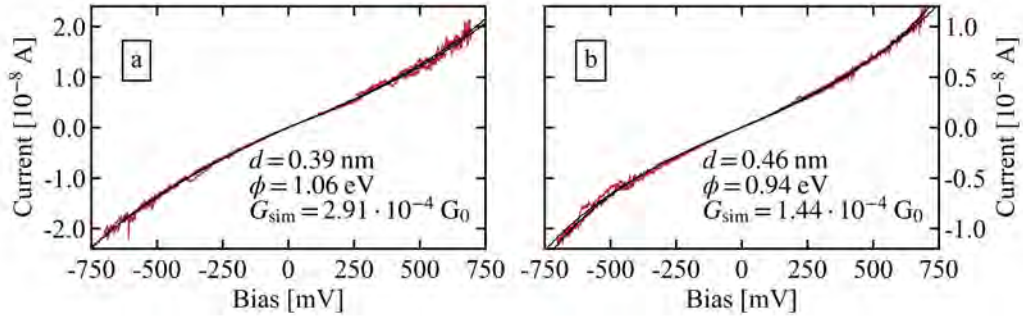


Figure 6.7: Example $I(V)$ curves with the extracted parameters. The measured $I(V)$ curves are plotted with dark red color, the fit from the simulation with black. The $I(V)$ curves are smoothed by applying a moving average with a window size of 10 points for visual clarity. The curve in (b) is the same as in Figure 6.5(b). The parameters like resistance, gap size and barrier height acquired from the simulation for the 4 segments are averaged and indicated in the bottom right corner.

It is important to note that due to the segmentation described above, the fitting of the four individual segments of the $I(V)$ curve, four sets of fitting parameters ($G_{\text{sim},r}$, d_r , ϕ_r) are collected. Each of these 4 parameter sets is used in the statistical analysis. However, since the maximum voltage of the $I(V)$ curve is 700 mV, some of the curves do not exhibit noticeable non-linear behavior within this voltage range. In such cases, the simulation either yields an unreasonably high barrier value (around $\phi = 2$ eV or saturates

Chapter 6. Correlating Noise and Nonlinear Conductance Data in Real-time Controlled Break Junction Measurements

at the maximum barrier height ($\phi = 2.25$ eV in our case). These curves were also discarded to avoid obscuring the statistical results. So, in case of the opening (closing), for the 2514 (6219) selected traces, we had $4 \cdot 2514 = 10056$ ($4 \cdot 6219 = 24876$) sets of fit parameters, but after discarding the parameter sets with saturated barrier height, 8845 (21168) remain.

For these remaining data after the filtering mentioned above, the 2D distributions of the gap size and the barrier height as a function of conductance are plotted in Figure 6.8(a)-(b) and Figure 6.8(c)-(d) for opening and closing, respectively. In the inset of Figure 6.8(a), using the 2D histogram of the simulated vs. measured conductance, I compared the simulated conductance with the measured conductance (i.e., the mean conductance of the constant bias plateaus) and found that they are congruent in both processes.

Based on Figures 6.8(a) to 6.8(d), we can draw the following conclusions:

- Lower conductances correspond to larger nanogap sizes. On a log-linear scale, we see a distribution that is close to a straight line, meaning that as the gap size increases linearly, the conductance decreases exponentially.
- As conductance decreases, the barrier height shows a slightly increasing, nearly constant trend, giving a broader but peaked distribution at each conductance in the range of approximately 0.7 eV to 1.1 eV (see the insets of Figures 6.8(b) and 6.8(d)).

These observations are consistent with the literature and intuitive expectations [82, 97, 98]. In the case of gold nanogaps, the change in conductance can primarily be attributed to the tuning of the electrode distance, and based on the Simmons model, we expect a proportionality of $\log(G) \sim -d$. Ideally, the barrier height would be expected to correspond to the work function of gold (approximately 5.3 eV). However, in the literature, it has been reported that, under ambient conditions, the work function can be significantly reduced from its vacuum value due to the formation of a water film and oxygen uptake on the electrodes [97, 98]. The barrier height values around (1 – 1.1) eV observed at lower conductance are in good agreement with the data from the literature, which were reported for gaps larger than 0.5 nm [97, 98]. At higher conductance values (i.e. smaller gap sizes), it is plausible that the influence of contaminants adsorbed on the electrode tips becomes even more pronounced, potentially contributing to a further slight decrease in the barrier height.

As the next step, the relative noise obtained from the simulation is calculated using the following equation:

$$\left[\left(\frac{\Delta G}{G} \right)_{\text{sim},r} \right]_{\Delta d, \Delta \phi} = \frac{1}{R_{\text{sim},r}} \cdot \sqrt{\left[\left(\frac{dR}{dd} \right)_{\text{sim},r}^2 \cdot \Delta d^2 + \left(\frac{dR}{d\phi} \right)_{\text{sim},r}^2 \cdot \Delta \phi^2 \right]}, \quad (6.1)$$

where $R_{\text{sim},r}$, $\left(\frac{dR}{dd} \right)_{\text{sim},r}^2$ and $\left(\frac{dR}{d\phi} \right)_{\text{sim},r}^2$ are determined from the simulation for a given $I(V)$ curve indexed by r , while Δd and $\Delta \phi$ are variable parameters that we try to determine by fitting the experimental data (see below).

Chapter 6. Correlating Noise and Nonlinear Conductance Data in Real-time Controlled Break Junction Measurements

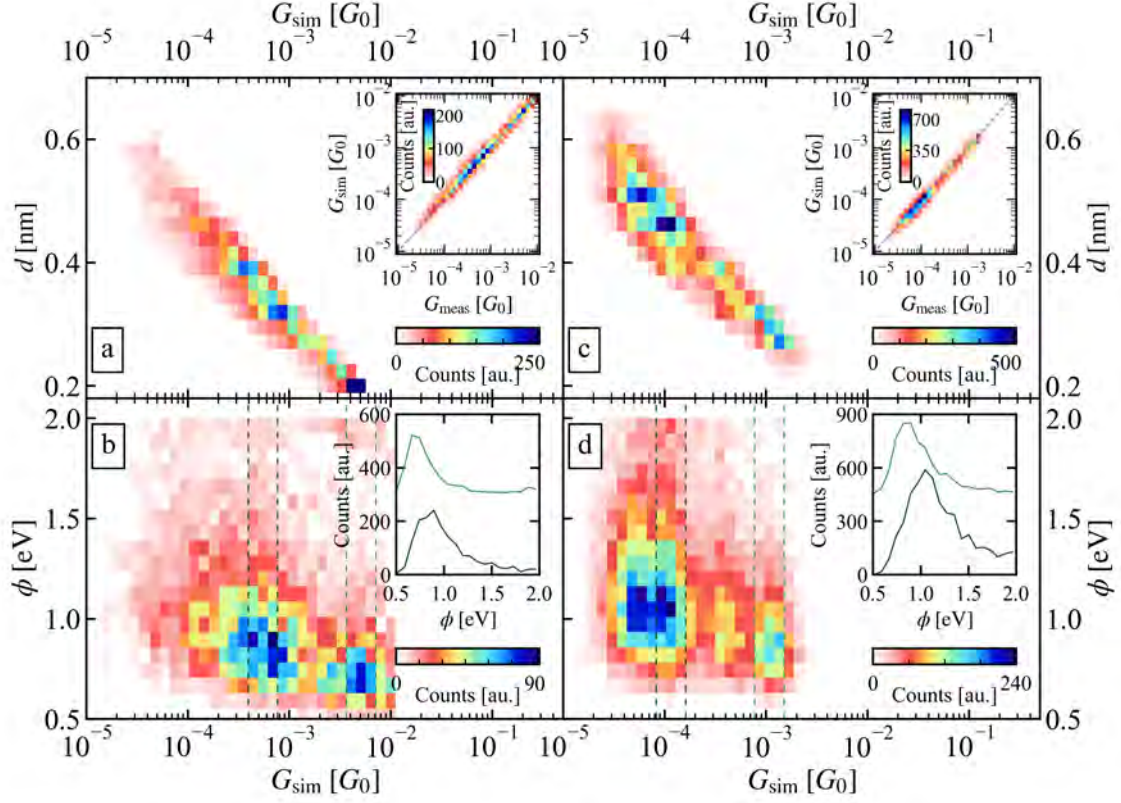


Figure 6.8: Distribution of the gap size and barrier height vs conductance in tunnel contacts acquired from simulation (a)/(c) 2D histogram of the simulated gap size (d) vs conductance (G_{sim}) for the opening/closing. In both processes, the conductance strongly depends on the size of the gap, as expected for a tunnel contact. Insets: 2D histograms of the conductance acquired from the simulation based on the $I(V)$ curves vs the conductance measured on the second plateau. (b)/(d) 2D histograms of the simulated barrier height vs conductance for the opening/closing. The barrier height does not show a strong dependence with the conductance contrary to the gap size. Insets: Distribution of the barrier height in the cross sections surrounded by dashed lines in the main figure. The light green histograms have been vertically shifted to improve visibility.

We can calculate the 2D relative noise–conductance histogram for the relative noise values obtained this way, similarly to how we did for the experimental results. In Figure 6.9, I plotted three examples with different gap size and barrier height fluctuations: Figures 6.9(a) to 6.9(c) show the calculated 2D histograms for only gap size, only barrier height, and both gap size and barrier height fluctuations, respectively. The white line represents the most probable values at the given conductance levels, determined from Gaussian fitting.

It can be seen that a completely different resistance dependence of $\Delta G/G$ is observed depending on whether gap size fluctuations or barrier height fluctuations are considered

Chapter 6. Correlating Noise and Nonlinear Conductance Data in Real-time Controlled Break Junction Measurements

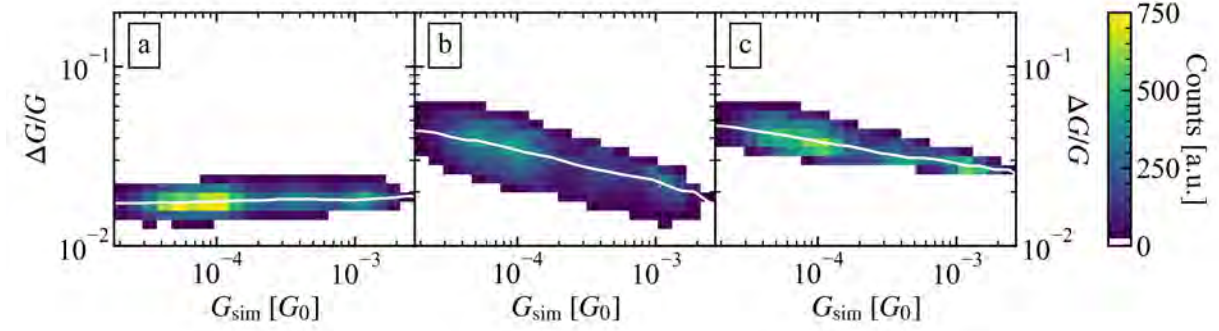


Figure 6.9: Relative noise distributions from simulation As a demonstration, the 2D histograms are calculated for different gap size and barrier height fluctuations for the closing process, the white lineplot is the mean relative noise, $\langle \Delta G/G \rangle$, which follows the peak positions of the Gaussian fits of each vertical bin, as in previous relative noise distributions. **(a) Gap size fluctuations only** Relative noise 2D histogram calculated with $\Delta d = 0.0014$ nm gap size fluctuations. When the gap size is the only fluctuating parameter, the relative noise is constant in the tunnel conductance range. **(b) Barrier height fluctuations** Relative noise 2D histogram calculated with $\Delta\phi = 0.02$ eV. When the barrier height is the only fluctuating parameter, the relative noise exhibits a strong conductance dependence. **(c) Mixed gap size and barrier height fluctuations** $\Delta d = 0.0014$ nm and $\Delta\phi = 0.02$ eV

as the dominant noise source. In the former case, the relative noise remains approximately constant, whereas in the latter, the relative noise shows a clear increase as the conductance decreases. This behavior is consistent with what is expected from the low-bias conductance formula derived from the Simmons model, $G \sim e^{-\sqrt{8m\phi x}/\hbar}$, assuming a constant barrier height (ϕ) and a varying gap size d [P3]. In the mixed case (i.e. when both the gap size and barrier height are allowed to fluctuate) the dependence of the relative noise on conductance is weakened: gap size fluctuations dominate at higher conductance values, while barrier height fluctuations become dominant at lower conductance values.

6.5 Comparison of measured and simulated noise characteristics

To match the simulated relative noise data and obtain the possible fluctuation amplitudes, I calculated the relative noise 2D histogram similar to those shown in Figure 6.9 for different parameter pairs. For the gap size fluctuation (Δd), I chose the range of (0 – 0.015) nm with a step size of 0.0001 nm, while for the barrier height fluctuation ($\Delta\phi$) changed in the range of (0 – 0.15) eV with a step size of 0.001 eV, which results in a 151×151 matrix containing the relative noise 2D histograms for each parameter pair.

From the large number of relative noise histograms obtained as described above, to

Chapter 6. Correlating Noise and Nonlinear Conductance Data in Real-time Controlled Break Junction Measurements

find the parameter pair that best describes the measured relative noise, I compare the most probable relative noise calculated from the measured 2D relative noise–conductance histograms (denoted by $\langle \frac{\Delta G}{G} \rangle_{\text{meas}}$) to those obtained from the simulation (denoted by $\langle \frac{\Delta G}{G} \rangle_{\text{sim},j,k}$, where j and k index the different gap size and barrier height fluctuations, respectively). To measure the similarity of the most probable relative noise traces, I use the square difference (sd) between the measured and simulated data:

$$\text{sd}_{j,k} = \sum_i \left(\left[\log \left(\left\langle \frac{\Delta G}{G} \right\rangle_{\text{meas}} \right) \right]_i - \left[\log \left(\left\langle \frac{\Delta G}{G} \right\rangle_{\text{sim},j,k} \right) \right]_i \right)^2, \quad (6.2)$$

where i indexes the conductance value corresponding to the i -th vertical bin of the relative noise – conductance 2D histogram. So I sum the square difference for each vertical bin (i), and repeat the process for each parameter pair (j, k), resulting in a square difference matrix ($\text{sd}_{j,k}$). The smallest value of this matrix means that the measured and simulated most probable relative noise trends are closest, so the corresponding j -th and k -th Δd and $\Delta\phi$ fluctuations describe best the noise trend observed in the measurements within the framework of our numerically evaluated Simmons model.

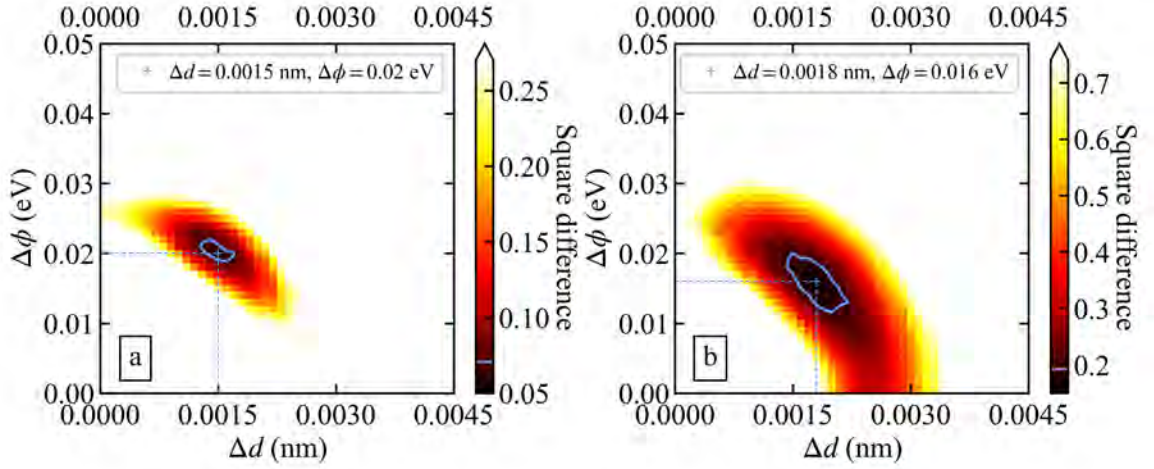


Figure 6.10: Heatmaps of the squared difference matrices of the simulated and measured mean relative noise ($\text{sd}_{j,k}$). (a)-(b) The simulated relative noise is compared to the measured relative noise for the opening/closing. In both panels, color scale ranges from the global minimum value (dark tones) to five times this value (white), while the light blue + denotes the position of the global minimum value (see the exact numbers in the inset). This parameter pair produces the relative noise closest to the measured data. The areas where the squared difference value differs less than 30% from the minimum value are surrounded by light blue contour plots.

Figure 6.10 shows the heat maps of the calculated $\text{sd}_{j,k}$ matrices for the opening and closing processes. In these plots, darker tones represent a low squared difference between

Chapter 6. Correlating Noise and Nonlinear Conductance Data in Real-time Controlled Break Junction Measurements

the measured and simulated trends. The global minimum on both panels is indicated by a light blue + sign. The corresponding gap size and barrier height fluctuations for the opening (closing) process are $\Delta d = 0.0015$ nm and $\Delta\phi = 0.020$ eV ($\Delta d = 0.0018$ nm and $\Delta\phi = 0.016$ eV). These estimated gap size and barrier height fluctuations differ slightly between the two processes; however, the heat maps show that the well-fitting cases tend to represent broader regions rather than single well-defined points.

The figure shows that in the best-fitting cases, the dark region representing the possible parameters does not touch either the gap size fluctuation axis or the barrier height fluctuation axis. This indicates that, according to the simulation, the experimentally observed noise trend cannot be described solely by the gap size or solely by the barrier height fluctuation.

The amplitude of the gap size fluctuation is ~ 2 pm for both plateaus, which is in the same range as values estimated from data from the literature using the barrier height of 1.1 eV and the relative fluctuation reported $\Delta I/I \approx 0.045$, resulting in $\Delta d \approx 4$ pm [29]. This value is somewhat higher, but still of the same order of magnitude as the $\Delta d = 2$ pm obtained in our analysis. This demonstrates that the sub-Ångström fluctuations obtained from the simulation are physically reasonable.

In the reference publication mentioned above, a trend $\Delta G/G \sim \text{const.}$ was observed and attributed solely to fluctuations in the size of the gap. In contrast, our simulations indicate that barrier height fluctuations are not negligible in our case. For an ideal theoretical tunnel junction, such barrier height fluctuations would not be expected to occur to first approximation; however, in a real physical system, they are conceivable. On the one hand, the work function of gold depends on the surface lattice structure, e.g., $W_{\text{Au},\langle 111 \rangle} = 5.3$ eV or $W_{\text{Au},\langle 100 \rangle} = 5.5$ eV [98]. Therefore, fluctuations in atomic positions around the nanogap may lead to variations in not only the gap size itself but also the barrier height. On the other hand, we have seen that the barrier heights estimated from our simulations are significantly lower than would be expected from the literature work function of gold. This points to the presence of surface contaminants (e.g., water vapor, oxygen) on the electrodes, whose movement or rearrangement could manifest as barrier height fluctuations. Considering that no barrier height fluctuations were observed in [29], we regard the latter effect as the more likely cause of the barrier height fluctuations in our case, as the presence of contaminants can strongly depend on the measurement conditions.

6.6 Conclusions

In summary, in this chapter I have demonstrated the capabilities of our recently developed FPGA-based real-time measurement control system through the investigation of highly sensitive gold tunnel nanojunctions.

In my first measurements, using a simple constant voltage bias, I tested the reaction time of the measurement system and the stability of the junction. I observed a relaxation phenomenon during the hold portion of the opening process, which is likely caused by

Chapter 6. Correlating Noise and Nonlinear Conductance Data in Real-time Controlled Break Junction Measurements

atomic rearrangements following the rupture of a stretched atomic contact. Consequently, once the electrode separation tuning is stopped during the opening process, the actual conductance configuration is determined more by self-organizing processes in the system than by the predefined trigger value. I showed that after the few hundred milliseconds long relaxation, the contact can remain stable for several seconds, making it suitable for performing complex measurements in the formed configuration. In the closing process, excellent stability was also observed, but without the relaxation phenomenon, making it ideal for performing measurements at the predefined conductance values.

I have demonstrated the potential of our FPGA-based measurement system with a measurement requiring a complex voltage pattern, in which combined $I(V)$ characteristics and noise measurements were performed during each hold period. From these measurements, I determined the conductance dependence of the relative noise in the gold tunnel junction, while the measured $I(V)$ curves were fitted using a numerically evaluated Simmons model to extract the gap size, barrier height, and simulated noise levels. Finally, by comparing the simulation results with the experimental noise characteristics, I found that, within the framework of the Simmons model, considering solely gap size fluctuations does not describe our experimental results. Instead, a combination of gap size and barrier height fluctuations (with respective amplitudes of approximately 2 pm and 20 meV), is required.

**Chapter 6. Correlating Noise and Nonlinear Conductance Data in
Real-time Controlled Break Junction Measurements**

Chapter 7

Thesis Statements

7.1 Binary conductance switching in gold–4,4'-bipyridine–gold single-molecule nanowires

I investigated the mechanical and voltage-controlled switching phenomena of gold–4,4'-bipyridine–gold molecular contacts at low temperature ($T = 4.2$ K) and compared the measurement results with simple theoretical models commonly used in the literature [P1].

I demonstrated that mechanical switching between the two configurations of the 4,4'-bipyridine molecule, previously seen in room-temperature measurements, can also be performed at low temperature, on a timescale that is orders of magnitude longer, thanks to cryogenic conditions.

I studied the conductance hysteresis that appears in the range associated with the molecular configurations in the conductance–electrode displacement graph and observed stochastic transitions in the $I(V)$ characteristics measurements. I have shown that these transitions occur between conductance values associated with the two molecular configurations and that the ratio of the times spent in each state changes depending on the electrode displacement and the position inside the hysteresis.

Finally, I examined how the characteristic time of the switching depends on the applied voltage, which allowed me to determine that the characteristic times decrease exponentially as the voltage increases, i.e. that the switching accelerates simultaneously in both states.

7.2 Investigation of configuration-specific noise characteristics of gold–4,4'-bipyridine–gold molecular contacts

I investigated the $1/f$ -type noise characteristics of gold–4,4'-bipyridine–gold molecular contacts as a function of their molecular configurations and conductance in room-temperature

break junction measurements. I demonstrated that trace selection based on the extremal principal component projection (EPCP) method combined with noise measurements gives us more information about the characteristics of molecular contacts [P2].

I performed slow break junction measurements using a low-noise system equipped with an anti-aliasing filter. I analyzed the resulting curves by evaluating their noise spectra during the breaking process and statistically examined the conductance dependence of the noise characteristics. I observed noise characteristics consistent with the molecular configurations and expectations based on the literature at the edges of the molecular conductance range; however, I found different behavior in the transition region between the configurations.

To better understand my observations, I used a curve selection method based on extremal principal component projection (EPCP), creating two groups of conductance curves, completely separating the high- and low-conductance molecular configurations. This allowed for a configuration-specific analysis of the conductance dependence of the relative noise. I showed that both molecular configurations exhibit a similar trend: a constant behavior in the upper part of the molecular conductance peak and a power-law dependence of $\sim G^{-0.5}$ in the lower part. These trends suggest the appearance of through-space and through-bond coupling in both configurations, respectively. Understanding the noise characteristics broken down by configuration also helped to explain the noise characteristics of the entire dataset. It revealed that the observed, unexpected trend might be a consequence of the alternating formation of through-space and through-bond couplings during the breaking process.

7.3 Investigation of stability and noise phenomena of gold nanogaps using an FPGA-based real-time measurement control system

Using the FPGA-based real-time measurement control system developed by our group, I investigated the stability and noise phenomena of gold nanogaps created with the room-temperature break junction technique [P3, P4].

Thanks to the rapid response time of the measurement system, I was able to observe the relaxation phenomenon occurring during the opening process, and that after this relaxation, which lasts for a few 100 ms, the junction can remain stable for several seconds. This makes it suitable for performing complex measurements in the resulting configuration. I observed a comparable degree of stability during the closing process, but without the relaxation phenomenon, showing that the closing process is ideal for measurements at predefined conductance values.

I demonstrated that because of the rapid response time and high stability, measurements requiring complex waveforms can also be performed. To this end, I performed combined $I(V)$ characteristics and noise measurements on gold nanogaps. I determined

the relative conductance noise of the gold tunnel junction as a function of the conductance, observing a slight conductance dependence. This conductance dependence cannot be explained with gap size fluctuations considered in simple tunnel models.

For a more complex noise analysis, the experimental $I(V)$ curves were modeled using a numerically evaluated Simmons model, yielding the size of the gap and the height of the potential barrier. Using the gap size and barrier height parameters while permitting their combined fluctuation, the noise characteristics can be simulated. I calculated the simulated noise characteristics considering various gap-size and barrier-height fluctuations and compared these findings with the measurement results. I have shown that, based on these simulations, the conductance dependence of the measured relative noise is most effectively explained with gap size fluctuations on the order of a few picometers combined with barrier height fluctuations on the order of 10 meV.

Chapter 8

Acknowledgements

I am deeply grateful to my supervisor, *Zoltán Balogh* for his invaluable guidance and his insightful feedback on the manuscript. I could always turn to him with both technical and theoretical questions.

I would also like to thank *Prof. András Halbritter* for inspiring me to pursue a Ph.D. in physics and for our invaluable discussions.

Next, I would like to thank my colleagues who contributed to the results. *András Magyarkuti* was instrumental in developing the measurement control setup, and I could always turn to him with technical questions about measurement control and data analysis in IgorPro. I also want to thank *Nóra Tenk* for implementing the principal component analysis in IgorPro; her code was a great help when I implemented it in Python. I am grateful to *László Pósa*, who helped with the simulations for the numerically evaluated Simmons model.

I am thankful to my fellow students, *Anna Nyáry* for proofreading the Hungarian booklet and summary, and to *Sánta Botond*, *Dániel Molnár*, and *Tímea Török* for always having a motivating word for me.

I would like to express my gratitude to the administrative and technical staff from the university. My measurements would not have been possible without the technical support of *Márton Hajdu* and *Béla Horváth* in maintaining and building the sample holders.

Last but not least, my deepest gratitude goes to my family for their unwavering support and love throughout these years. Without you, I could not have completed this journey. I am especially grateful to my husband, *Ottó Hanyecz*, for his immense support and love, particularly during the final stretch before submitting my thesis. I am also thankful to my parents, who inspired me to always keep on learning (*Köszönöm, anya és apa!*), and to my in-laws for their support and patience. I am thankful to my brother *Berci*, for his emotional support during my studies and to my friends *Antónia Horváth* and *Zsófia Szatmári* for cheering me on on this journey.

This thesis was supported by the TKP2021-NVA-02 grants of the Ministry of Culture and Innovation of Hungary through the National Research, Development and Innovation Fund.

Chapter 8. Acknowledgements

List of Publications

- [P1] **G. Mezei**, Z. Balogh, A. Magyarkuti, and A. Halbritter, “Voltage-controlled binary conductance switching in gold-4,4'-bipyridine-gold single-molecule nanowires”, *Journal of Physical Chemistry Letters* **11**, 8053–8059 (2020).
- [P2] Z. Balogh, **G. Mezei**, N. Tenk, A. Magyarkuti, and A. Halbritter, “Configuration-specific insight into single-molecule conductance and noise data revealed by the principal component projection method”, *Journal of Physical Chemistry Letters* **14**, 5109–5118 (2023).
- [P3] Z. Balogh, **G. Mezei**, L. Pósa, B. Sánta, A. Magyarkuti, and A. Halbritter, “1/f noise spectroscopy and noise tailoring of nanoelectronic devices”, *Nano Futures* **5**, 10.1088/2399-1984/ac14c8 (2021).
- [P4] **G. Mezei**, A. Magyarkuti, L. Pósa, A. Halbritter, and Z. Balogh, “Correlating noise and nonlinear conductance data in real-time controlled break junction measurements”, To be submitted (2025).

List of Publications

Other Publications

- [O1] A. Magyarkuti, Z. Balogh, **G. Mezei**, and A. Halbritter, “Structural memory effects in gold–4,4′-bipyridine–gold single-molecule nanowires”, *The Journal of Physical Chemistry Letters* **12**, 1759–1764 (2021).
- [O2] W. Bro-Jørgensen, J. M. Hamill, **G. Mezei**, B. Lawson, U. Rashid, A. Halbritter, M. Kamenetska, V. Kaliginedi, and G. C. Solomon, “Making the most of nothing: one-class classification for single-molecule transport studies”, *ACS Nanoscience Au* **4**, 250–262 (2024).

Other Publications

Bibliography

- [1] R. P. Feynman, “There’s plenty of room at the bottom”, *Engineering and Science* **23** (1960).
- [2] G. E. Moore, “Cramming more components onto integrated circuits”, *Electronics* **38** (1965).
- [3] A. Aviram and M. A. Ratner, “Molecular rectifiers”, *Chemical Physics Letters* **29**, 277–283 (1974).
- [4] C. Joachim, J. K. Gimzewski, and A. Aviram, “Electronics using hybrid-molecular and mono-molecular devices”, *Nature* **408**, 541–548 (2000).
- [5] G. Qu, T. Xia, W. Zhou, X. Zhang, H. Zhang, L. Hu, J. Shi, X.-F. Yu, and G. Jiang, “Property–activity relationship of black phosphorus at the nano–bio interface: from molecules to organisms”, *Chemical Reviews* **120**, 2288–2346 (2020).
- [6] T. Li, W. Hu, and D. Zhu, “Nanogap electrodes”, *Advanced Materials* **22**, 286–300 (2010).
- [7] V. R. Manfrinato, L. Zhang, D. Su, H. Duan, R. G. Hobbs, E. A. Stach, and K. K. Berggren, “Resolution limits of electron-beam lithography toward the atomic scale”, *Nano Letters* **13**, 1555–1558 (2013).
- [8] J. Moreland and J. W. Ekin, “Electron tunneling experiments using nb-sn “break” junctions”, *Journal of Applied Physics* **58**, 3888–3895 (1985).
- [9] J. K. Gimzewski and R. Möller, “Transition from the tunneling regime to point contact studied using scanning tunneling microscopy”, *Phys. Rev. B* **36**, 1284–1287 (1987).
- [10] C. Muller, J. van Ruitenbeek, and L. de Jongh, “Experimental observation of the transition from weak link to tunnel junction”, *Physica C: Superconductivity* **191**, 485–504 (1992).
- [11] J. I. Pascual, J. Méndez, J. Gómez-Herrero, A. M. Baró, N. García, and V. T. Binh, “Quantum contact in gold nanostructures by scanning tunneling microscopy”, *Phys. Rev. Lett.* **71**, 1852–1855 (1993).
- [12] M. A. Reed, C. Zhou, C. Muller, T. Burgin, and J. Tour, “Conductance of a molecular junction”, *Science* **278**, 252–254 (1997).

Bibliography

- [13] A. I. Yanson, G. Rubio Bollinger, H. E. van den Brom, N. Agraït, and J. M. van Ruitenbeek, “Formation and manipulation of a metallic wire of single gold atoms”, *Nature* **395**, 783–785 (1998).
- [14] H. Ohnishi, Y. Kondo, and K. Takayanagi, “Quantized conductance through individual rows of suspended gold atoms”, *Nature* **395**, 780–783 (1998).
- [15] N. Agraït, A. L. Yeyati, and J. M. van Ruitenbeek, “Quantum properties of atomic-sized conductors”, *Physics Reports* **377**, 81–279 (2003).
- [16] A. F. Morpurgo, C. M. Marcus, and D. B. Robinson, “Controlled fabrication of metallic electrodes with atomic separation”, *Applied Physics Letters* **74**, 2084–2086 (1999).
- [17] J. Sutanto, R. L. Smith, and S. D. Collins, “Fabrication of nano-gap electrodes and nano wires using an electrochemical and chemical etching technique”, *Journal of Micromechanics and Microengineering* **20**, 045016 (2010).
- [18] H. Park, A. K. L. Lim, A. P. Alivisatos, J. Park, and P. L. McEuen, “Fabrication of metallic electrodes with nanometer separation by electromigration”, *Applied Physics Letters* **75**, 301–303 (1999).
- [19] D. R. Strachan, D. E. Smith, M. D. Fischbein, D. E. Johnston, B. S. Guiton, M. Drndić, D. A. Bonnell, and A. T. Johnson, “Clean electromigrated nanogaps imaged by transmission electron microscopy”, *Nano Letters* **6**, 441–444 (2006).
- [20] Z. M. Wu, M. Steinacher, R. Huber, M. Calame, S. J. van der Molen, and C. Schönenberger, “Feedback controlled electromigration in four-terminal nanojunctions”, *Applied Physics Letters* **91**, 053118 (2007).
- [21] T. Taychatanapat, K. I. Bolotin, F. Kuemmeth, and D. C. Ralph, “Imaging electromigration during the formation of break junctions”, *Nano Letters* **7**, 652–656 (2007).
- [22] T. Yelin, R. Vardimon, N. Kuritz, R. Korytár, A. Bagrets, F. Evers, L. Kronik, and O. Tal, “Atomically wired molecular junctions: connecting a single organic molecule by chains of metal atoms”, *Nano Letters* **13**, 1956–1961 (2013).
- [23] S. V. Aradhya and L. Venkataraman, “Single-molecule junctions beyond electronic transport”, *Nature Nanotech* **8**, 399–410 (2013).
- [24] Y. Komoto, J. Ryu, and M. Taniguchi, “Total variation denoising-based method of identifying the states of single molecules in break junction data”, *Discover Nano* **19**, 10.1186/s11671-024-03963-4 (2024).
- [25] S. Kogan, *Electronic noise and fluctuations in solids* (Cambridge University Press, 1996).

-
- [26] A. Balandin, S. Morozov, S. Cai, R. Li, K. Wang, G. Wijeratne, and C. Viswanathan, “Low flicker-noise GaN/AlGa_N heterostructure field-effect transistors for microwave communications”, *IEEE Transactions on Microwave Theory and Techniques* **47**, 1413–1417 (1999).
- [27] A. Balandin, *Noise and fluctuations control in electronic devices* (American Scientific Publishers, Stevenson Ranch, Calif, 2002).
- [28] A. A. Balandin, “Low-frequency 1/f noise in graphene devices”, *Nature Nanotechnology* **8**, 549–555 (2013).
- [29] O. Adak, E. Rosenthal, J. Meisner, E. F. Andrade, A. N. Pasupathy, C. Nuckolls, M. S. Hybertsen, and L. Venkataraman, “Flicker noise as a probe of electronic interaction at metal–single molecule interfaces”, *Nano Letters* **15**, 4143–4149 (2015).
- [30] A. Magyarkuti, O. Adak, A. Halbritter, and L. Venkataraman, “Electronic and mechanical characteristics of stacked dimer molecular junctions”, *Nanoscale* **10**, 3362–3368 (2018).
- [31] S. Yuan, T. Gao, W. Cao, Z. Pan, J. Liu, J. Shi, and W. Hong, “The characterization of electronic noise in the charge transport through single-molecule junctions”, *Small Methods* **5**, 2001064 (2021).
- [32] A. Halbritter, P. Makk, S. Csonka, and G. Mihály, “Huge negative differential conductance in Au-H₂ molecular nanojunctions”, *Phys. Rev. B* **77**, 075402 (2008).
- [33] A. Halbritter, P. Makk, S. Mackowiak, S. Csonka, M. Wawrzyniak, and J. Martinek, “Regular atomic narrowing of ni, fe, and v nanowires resolved by two-dimensional correlation analysis”, *Phys. Rev. Lett.* **105**, 266805 (2010).
- [34] P. Makk, D. Tomaszewski, J. Martinek, Z. Balogh, S. Csonka, M. Wawrzyniak, M. Frei, L. Venkataraman, and A. Halbritter, “Correlation analysis of atomic and single-molecule junction conductance”, *ACS Nano* **6**, 3411–3423 (2012).
- [35] P. Makk, Z. Balogh, S. Csonka, and A. Halbritter, “Pulling platinum atomic chains by carbon monoxide molecules”, *Nanoscale* **4**, 4739–4745 (2012).
- [36] P. Makk, “Investigation of atomic and molecular nanojunctions beyond conductance histograms”, PhD thesis (Budapest University of Technology and Economics, 2012).
- [37] G. Mezei, “Egyedi szerves molekulákból kialakított nanovezetékek kísérleti vizsgálata” (Budapest University of Technology and Economics, 2018).
- [38] A. Halbritter, “Investigation of atomic-sized conductors with the mechanically controllable break junction technique”, PhD thesis (Budapest University of Technology and Economics, 2003).
- [39] A. Halbritter, *Elektrontranszport atomi méretskálán*, 2014.
- [40] Z. Balogh, “Atomi kontaktusok kölcsönhatása szén-monoxid molekulákkal”, PhD thesis (Budapest University of Technology and Economics, 2017).

Bibliography

- [41] A. Magyarkuti, “Analysis of break junction measurements with single organic molecules using advanced statistical methods”, PhD thesis (Budapest University of Technology and Economics, 2020).
- [42] Z. Balogh, D. Visontai, P. Makk, K. Gillemot, L. Oroszlány, L. Pósa, C. Lambert, and A. Halbritter, “Precursor configurations and post-rupture evolution of ag–co–ag single-molecule junctions”, *Nanoscale* **6**, 14784–14791 (2014).
- [43] A. Magyarkuti, K. P. Lauritzen, Z. Balogh, A. Nyáry, G. Mészáros, P. Makk, G. C. Solomon, and A. Halbritter, “Temporal correlations and structural memory effects in break junction measurements”, *The Journal of Chemical Physics* **146**, 092319 (2017).
- [44] N. Balogh, “Molekuláris elektronikai mérések elemzése modern gépi tanulási és adatbányászati módszerekkel” (Budapest University of Technology and Economics, 2020).
- [45] K. P. Lauritzen, A. Magyarkuti, Z. Balogh, A. Halbritter, and G. C. Solomon, “Classification of conductance traces with recurrent neural networks”, *The Journal of Chemical Physics* **148**, 084111 (2018).
- [46] A. Magyarkuti, N. Balogh, Z. Balogh, L. Venkataraman, and A. Halbritter, “Unsupervised feature recognition in single-molecule break junction data”, *Nanoscale* **12**, 8355–8363 (2020).
- [47] M. Yuan, Y. Qiu, H. Gao, J. Feng, L. Jiang, and Y. Wu, “Molecular electronics: from nanostructure assembly to device integration”, *Journal of the American Chemical Society* **146**, 7885–7904 (2024).
- [48] D. Sharma, S. P. Rath, B. Kundu, A. Korkmaz, H. S. D. Thompson, N. Bhat, S. Goswami, R. S. Williams, and S. Goswami, “Linear symmetric self-selecting 14-bit kinetic molecular memristors”, *Nature* **633**, 560–566 (2024).
- [49] X. Xu, C. Gao, R. Emusani, C. Jia, and D. Xiang, “Toward practical single-molecule/atom switches”, *Advanced Science* **11**, 2400877 (2024).
- [50] A. Galanti, V. Diez-Cabanes, J. Santoro, M. Valášek, A. Minoia, M. Mayor, J. Cornil, and P. Samorì, “Electronic decoupling in c3-symmetrical light-responsive tris(azobenzene) scaffolds: self-assembly and multiphotochromism”, *Journal of the American Chemical Society* **140**, 16062–16070 (2018).
- [51] L. Meng, N. Xin, C. Hu, J. Wang, B. Gui, J. Shi, C. Wang, C. Shen, G. Zhang, H. Guo, S. Meng, and X. Guo, “Side-group chemical gating via reversible optical and electric control in a single molecule transistor”, *Nature Communications* **10**, 1450 (2019).
- [52] M. Nakamura, S. Yoshida, T. Katayama, A. Taninaka, Y. Mera, S. Okada, O. Takeuchi, and H. Shigekawa, “Mechanically activated switching of si-based single-molecule junction as imaged with three-dimensional dynamic probe”, *Nature Communications* **6**, 8465 (2015).

- [53] Z. Feng, S. Velari, C. Dri, A. Goldoni, M. Peressi, and G. Comelli, “Binary conformational switches in a porphyrin chain: tautomerization and stereoisomerization”, *The Journal of Physical Chemistry C* **124**, 11376–11382 (2020).
- [54] S. Y. Quek, M. Kamenetska, M. L. Steigerwald, H. J. Choi, S. G. Louie, M. S. Hybertsen, J. B. Neaton, and L. Venkataraman, “Mechanically controlled binary conductance switching of a single-molecule junction”, *Nature Nanotechnology* **4**, 10.1038/nano.2009.10 (2009).
- [55] S. Goswami, R. Pramanick, A. Patra, S. P. Rath, M. Foltin, A. Ariando, D. Thompson, T. Venkatesan, S. Goswami, and R. S. Williams, “Decision trees within a molecular memristor”, *Nature* **597**, 51–56 (2021).
- [56] J. C. Cuevas and E. Scheer, *Molecular electronics - an introduction to theory and experiment* (World Scientific, 2010).
- [57] S.-L. Lv, C. Zeng, Z. Yu, J.-F. Zheng, Y.-H. Wang, Y. Shao, and X.-S. Zhou, “Recent advances in single-molecule sensors based on stm break junction measurements”, *Biosensors* **12**, 10.3390/bios12080565 (2022).
- [58] D. Natelson, *Nanostructures and nanotechnology* (Cambridge University Press, 2015).
- [59] M. Frei, S. V. Aradhya, M. Koentopp, M. S. Hybertsen, and L. Venkataraman, “Mechanics and chemistry: single molecule bond rupture forces correlate with molecular backbone structure”, *Nano Letters* **11**, PMID: 21366230, 1518–1523 (2011).
- [60] S. V. Aradhya, M. Frei, M. S. Hybertsen, and L. Venkataraman, “Van der waals interactions at metal/organic interfaces at the single-molecule level”, *Nature Materials* **11**, 872–876 (2012).
- [61] M. Frei, S. V. Aradhya, M. S. Hybertsen, and L. Venkataraman, “Linker dependent bond rupture force measurements in single-molecule junctions”, *Journal of the American Chemical Society* **134**, 4003–4006 (2012).
- [62] Y. Zhu, Z. Tan, and W. Hong, “Simultaneous electrical and mechanical characterization of single-molecule junctions using afm-bj technique”, *ACS Omega* **6**, 30873–30888 (2021).
- [63] S. Datta, *Electronic transport in mesoscopic systems*, Cambridge Studies in Semiconductor Physics and Microelectronic Engineering (Cambridge University Press, 1995).
- [64] C. A. Martin, D. Ding, J. K. Sørensen, T. Bjørnholm, J. M. van Ruitenbeek, and H. S. J. van der Zant, “Fullerene-based anchoring groups for molecular electronics”, *Journal of the American Chemical Society* **130**, 13198–13199 (2008).
- [65] M. Kamenetska, M. Koentopp, A. C. Whalley, Y. S. Park, M. L. Steigerwald, C. Nuckolls, M. S. Hybertsen, and L. Venkataraman, “Formation and evolution of single-molecule junctions”, *Phys. Rev. Lett.* **102**, 126803 (2009).

Bibliography

- [66] S. V. Aradhya, M. Frei, A. Halbritter, and L. Venkataraman, “Correlating structure, conductance, and mechanics of silver atomic-scale contacts”, *ACS Nano* **7**, 3706–3712 (2013).
- [67] J. M. Hamill, X. T. Zhao, G. Mészáros, M. R. Bryce, and M. Arenz, “Fast data sorting with modified principal component analysis to distinguish unique single molecular break junction trajectories”, *Phys. Rev. Lett.* **120**, 016601 (2018).
- [68] M. Greenacre, P. J. F. Groenen, T. Hastie, A. I. D’Enza, A. Markos, and E. Tuzhilina, “Principal component analysis”, *Nature Reviews Methods Primer*, 10.1038/s43586-022-00184-w (2022).
- [69] T. Fu, Y. Zang, Q. Zou, C. Nuckolls, and L. Venkataraman, “Using deep learning to identify molecular junction characteristics”, *Nano Letters* **20**, 3320–3325 (2020).
- [70] W. Bro-Jørgensen, J. M. Hamill, R. Bro, and G. C. Solomon, “Trusting our machines: validating machine learning models for single-molecule transport experiments”, *Chem. Soc. Rev.* **51**, 6875–6892 (2022).
- [71] L. Pósa, Z. Balogh, D. Krisztián, P. Balázs, B. Sánta, R. Furrer, M. Csontos, and A. Halbritter, “Noise diagnostics of graphene interconnects for atomic-scale electronics”, *npj 2D Materials and Applications* **5**, 10.1038/s41699-021-00237-w (2021).
- [72] Z. Pan, L. Chen, C. Tang, Y. Hu, S. Yuan, T. Gao, J. Shi, J. Shi, Y. Yang, and W. Hong, “The evolution of the charge transport mechanism in single-molecule break junctions revealed by flicker noise analysis”, *Small* **18**, 2107220 (2022).
- [73] B. Sánta, “Rezisztív kapcsoló memóriák dinamikai vizsgálata”, PhD thesis (Budapest University of Technology and Economics, 2021).
- [74] H. Nyquist, “Thermal Agitation of Electric Charge in Conductors”, *Physical Review* **32**, 110–113 (1928).
- [75] J. B. Johnson, “Thermal Agitation of Electricity in Conductors”, *Physical Review* **32**, 97–109 (1928).
- [76] G. Mészáros, C. Li, I. Pobelov, and T. Wandlowski, “Current measurements in a wide dynamic range – applications in electrochemical nanotechnology”, *Nanotechnology* **18**, 424004 (2007).
- [77] *Variable gain low noise current amplifier*, <https://www.femto.de/images/pdf-dokumente/de-dlpca-200.pdf>, 2024.
- [78] *Loctite stycast 2850ft*, https://datasheets.tdx.henkel.com/LOCTITE-STYCAST-2850FT-CAT-27-1-en_GL.pdf, 2024.
- [79] *Sigma aldrich gold wire, diam. 0.1 mm, 99.99% trace metals basis*, <https://www.sigmaaldrich.com/HU/en/product/aldrich/349283>, 2024.
- [80] *Electronics for piezoaction*, https://www.piezomechanik.com/fileadmin/content_files/catalogs/piezomechanik-electronics.pdf, 2024.

-
- [81] *H5py quick start guide*, 2024.
- [82] C. Untiedt, A. I. Yanson, R. Grande, G. Rubio-Bollinger, N. Agrait, S. Vieira, and J. van Ruitenbeek, “Calibration of the length of a chain of single gold atoms”, *Phys. Rev. B* **66**, 085418 (2002).
- [83] T. Kim, P. Darancet, J. R. Widawsky, M. Kotiuga, S. Y. Quek, J. B. Neaton, and L. Venkataraman, “Determination of energy level alignment and coupling strength in 4,4′-bipyridine single-molecule junctions”, *Nano Letters* **14**, 794–798 (2014).
- [84] A. Borges, E.-D. Fung, F. Ng, L. Venkataraman, and G. C. Solomon, “Probing the conductance of the s-system of bipyridine using destructive interference”, *The Journal of Physical Chemistry Letters* **7**, 4825–4829 (2016).
- [85] M. L. Trouwborst, E. H. Huisman, F. L. Bakker, S. J. van der Molen, and B. J. van Wees, “Single atom adhesion in optimized gold nanojunctions”, *Phys. Rev. Lett.* **100**, 175502 (2008).
- [86] S. V. Aradhya, A. Nielsen, M. S. Hybertsen, and L. Venkataraman, “Quantitative bond energetics in atomic-scale junctions”, *ACS Nano* **8**, 7522–7530 (2014).
- [87] A. Halbritter, L. Borda, and A. Zawadowski, “Slow two-level systems in point contacts”, *Advances in Physics* **53**, 939–1010 (2004).
- [88] T. N. Todorov, “Local heating in ballistic atomic-scale contacts”, *Philosophical Magazine B* **77**, 965–973 (1998).
- [89] Y. Kim, T. J. Hellmuth, M. Bürkle, F. Pauly, and E. Scheer, “Characteristics of amine-ended and thiol-ended alkane single-molecule junctions revealed by inelastic electron tunneling spectroscopy”, *ACS Nano* **5**, 4104–4111 (2011).
- [90] C. Wu, D. Bates, S. Sangtarash, N. Ferri, A. Thomas, S. J. Higgins, C. M. Robertson, R. J. Nichols, H. Sadeghi, and A. Vezzoli, “Folding a single-molecule junction”, *Nano Lett.* **20**, 7980–7986 (2020).
- [91] P. Darancet, J. R. Widawsky, H. J. Choi, L. Venkataraman, and J. B. Neaton, “Quantitative current–voltage characteristics in molecular junctions from first principles”, *Nano Letters* **12**, 6250–6254 (2012).
- [92] B. Capozzi, J. Xia, O. Adak, E. J. Dell, Z.-F. Liu, J. C. Taylor, J. B. Neaton, L. M. Campos, and L. Venkataraman, “Single-molecule diodes with high rectification ratios through environmental control”, *Nature Nanotechnology* **10**, 522–527 (2012).
- [93] M. A. Karimi, S. G. Bahoosh, M. Herz, R. Hayakawa, F. Pauly, and E. Scheer, “Shot noise of 1,4-benzenedithiol single-molecule junctions”, *Nano Letters* **16**, 1803–1807 (2016).
- [94] T. Fu, K. Frommer, C. Nuckolls, and L. Venkataraman, “Single-molecule junction formation in break-junction measurements”, *The Journal of Physical Chemistry Letters* **12**, 10802–10807 (2021).

Bibliography

- [95] A. Nyáry, Z. Balogh, B. Sánta, G. Lázár, N. Jimenez Olalla, J. Leuthold, M. Csontos, and A. Halbritter, “Benchmarking stochasticity behind reproducibility: denoising strategies in ta₂o₅ memristors”, *ACS Applied Materials & Interfaces* **17**, 25654–25662 (2025).
- [96] J. G. Simmons, “Generalized formula for the electric tunnel effect between similar electrodes separated by a thin insulating film”, *Journal of Applied Physics* **34**, 1793–1803 (1963).
- [97] C. Kergueris, J.-P. Bourgoin, S. Palacin, D. Esteve, C. Urbina, M. Magoga, and C. Joachim, “Electron transport through a metal-molecule-metal junction”, *Phys. Rev. B* **59**, 12505–12513 (1999).
- [98] S. A. G. Vrouwe, E. van der Giessen, S. J. van der Molen, D. Dulic, M. L. Trouwborst, and B. J. van Wees, “Mechanics of lithographically defined break junctions”, *Phys. Rev. B* **71**, 035313 (2005).